

N74-10031

NASA CONTRACTOR  
REPORT

NASA CR-2340



NASA CR-2340

CASE FILE  
COPY

RESEARCH ON THE SONIC BOOM PROBLEM  
Part 2 -Flow Field Measurement in Wind Tunnel  
and Calculation of Second Order F-Function

by M. Landahl, H. Sorensen, and L. Hilding

Prepared by

THE AERONAUTICAL RESEARCH INSTITUTE OF SWEDEN  
Stockholm, Sweden

for

NATIONAL AERONAUTICS AND SPACE ADMINISTRATION • WASHINGTON, D. C. • NOVEMBER 1973

1. Report No. NASA CR-2340	2. Government Accession No.	3. Recipient's Catalog No.	
4. Title and Subtitle <b>RESEARCH ON THE SONIC BOOM PROBLEM PART 2 FLOW FIELD MEASUREMENT IN WIND TUNNEL AND CALCULATION OF SECOND ORDER F -FUNCTION</b>		5. Report Date November 1973	
		6. Performing Organization Code	
7. Author(s) <b>M. Landahl, H. Sørensen and L. Hilding</b>		8. Performing Organization Report No. <b>FFA AU-621</b>	
9. Performing Organization Name and Address <b>The Aeronautical Research Institute of Sweden Aerodynamics Department Stockholm, Sweden</b>		10. Work Unit No.	
		11. Contract or Grant No. <b>NGR-52-120-001</b>	
12. Sponsoring Agency Name and Address <b>National Aeronautics and Space Administration Washington, D. C. 20546</b>		13. Type of Report and Period Covered <b>Final</b>	
		14. Sponsoring Agency Code	
15. Supplementary Notes			
16. Abstract  An experimental investigation has been carried out in the FFA-TVM wind tunnel to test some of the results of Landahl's second order theory. The slender models consisted of a parabolic spindle, tested at $M = 3$ , and a wing body configuration, suggested by Ferri, and tested at $M = 2.7$ .  The theory indicates that shock position and strength at an arbitrary distance can be calculated by means of near field measurements. The results show that this method is an appropriate one for simple bodies and for bodies with complicated geometries as well.			
17. Key Words (Suggested by Author(s)) <b>Sonic Boom Supersonic Flow</b>		18. Distribution Statement <b>Unclassified - Unlimited</b>	
19. Security Classif. (of this report) <b>Unclassified</b>	20. Security Classif. (of this page) <b>Unclassified</b>	21. No. of Pages <b>111</b>	22. Price* <b>Domestic, \$4.25 Foreign, \$6.75</b>

\* For sale by the National Technical Information Service, Springfield, Virginia 22151

**LIST OF CONTENTS**

	<b>Page</b>
<b>SYMBOLS</b>	<b>iv</b>
<b>1. INTRODUCTION</b>	<b>1</b>
<b>2. MODEL AND APPARATUS</b>	<b>2</b>
<b>3. TEST CONDITIONS AND ACCURACY</b>	<b>3</b>
<b>4. EXPERIMENTAL RESULTS</b>	<b>4</b>
<b>5. CALCULATIONS</b>	<b>5</b>
<b>6. CONCLUSION</b>	<b>8</b>
<b>REFERENCES</b>	<b>9</b>
<b>TABLE</b>	<b>11</b>
<b>FIGURES</b>	<b>12</b>

## SYMBOLS

D	diam. of parabolic spindle
F	F-function (Whitham)
K	$\{(n+1)M_\infty^4\} / (2\beta^2)$
L, L <sub>o</sub>	model length (see Fig. 1 and Fig. 4)
M <sub>1</sub>	Mach number ahead of shock wave at probe apex
M <sub>∞</sub>	free-stream Mach number
V <sub>1</sub>	velocity ahead of shock wave at probe apex
V <sub>∞</sub>	free-stream velocity
d	sting diameter
p	static pressure
p <sub>t,1</sub>	total pressure ahead of shock wave at probe apex
p <sub>t,2</sub>	total pressure measured behind normal shock wave at probe apex (pitot pressure)
r	radial distance from model centerline
u	velocity component in main flow direction
v	velocity component in radial direction
x, y, z	Cartesian coordinates for model
x <sub>1</sub> , y <sub>1</sub> , z <sub>1</sub>	Cartesian coordinates of pressure probe (Fig. 5 and Fig. 6)
y	characteristics coordinate
α	angle of incidence of model axes relative to free-stream
β	$(M_\infty^2 - 1)^{1/2}$
κ	ratio of specific heats
φ	potential
ε	angle of downwash
σ	angle of sidewash
θ	meridian angle

index

0 symbols with this index are defined on p. 8

## 1. INTRODUCTION

To test some of the more important results of the second order theory of Landahl et al [1], an experimental investigation has been carried out in the FFA-TVM wind tunnel. One of the conclusions reached in the theory is that the non-linear effects are to lowest order confined to the very near field. This simplifies the experimental verification considerably, since it is not necessary to measure the flow field at very large distances from the model, obviating in particular the need to test with very small models. For the introductory experiments, a body of simple shape, a parabolic spindle, was selected. The investigation was conducted at Mach number 3. In a following set of experiments, a wing-body model, proposed by Ferri, was used, at a Mach number of 2,7.

A careful mapping of the supersonic flow field in the vicinity of the body was carried out. The streamline deviation was measured for several streamlines starting on a cylindrical tube placed around the model, having the axis parallel to the wind, and at small distances from the axis. In the experiments performed, the distance is smaller than the length of the model. For the wing-body model, the deviation of each streamline of this tube was measured locally in several meridian planes. Two angles were measured: one gives the deviation in the meridian plane, and the second gives the deviation on the cylinder normal to the meridian plane.

Whitham [2], in his paper on the flow pattern of a supersonic projectile, developed a method for calculating the pressure field of the body, and gave some simple formulae for the far field. The second order theory by Landahl et al [1] shows however, that certain terms should be added in Whitham's formulae for the F-function and the characteristics coordinate  $y$ . These terms can be calculated by means of the near field measurements [3]. Some calculations have been made to show the intensity and position of the shock waves.

## 2. MODEL AND APPARATUS

The parabolic spindle with the diameter  $D = 40$  mm and the length  $L = 282,84$  mm (the theoretical length  $L_0 = 339,4$  mm) was constructed of brass, and has pressure orifices over the whole length in one section. The model, its coordinates and the coordinates for the pressure orifices are shown in Fig. 1 and 2.

The three-dimensional model, as suggested by Ferri, is shown in Fig. 3. The wing is swept back at  $72^\circ$ . The wing profile has 2% thickness and is a symmetrical circular arc profile. The fuselage shape has a circular cross section; detailed dimensions of the fuselage area as a function of the distance are given in Table 1.

The construction of the model has required some modification on the wing leading edge and fuselage front tip, and on the rear part of the fuselage. The modification introduced at the leading edge is required in order to avoid local separation. The modification at the rear part of the fuselage is required because of the pressure of the support.

The support increases the equivalent area in the rear part of the vehicle. In order to eliminate this effect, the equivalence between lift and cross-sectional area has been utilized, and a correction on the planform of the wing has been introduced. The area of the wing has been reduced in the region where the fuselage cross section is different from the theoretical design. The design of the model is shown in Fig. 4.

The hemispherical differential pressure yaw meter employed for pressure measurements is shown in Fig. 7 and 8. The pressure probe has a diameter of 3,5 mm. Four static-pressure orifices are located circumferentially  $90^\circ$  apart on the hemispherical surface and four on the cylindrical surface. A pitot-pressure orifice is located at the probe apex. The static-pressure orifice diameters are 0,5 mm and the pitot-pressure orifice diameter is 1,0 mm.

The tunnel total pressure was sensed in the settling chamber, and the reference pressure in the test section with two 74 psia Foxboro 611 DM transducers. The probe and model pressure were measured with high-sensitivity pressure devices. For the model pressure and the four static pressures on the hemispherical surface pressure scanners were used. The pressure scanner for the model pressure was located in the movable sting, and the transducers and scanners for the probe were located outside the wind tunnel. A schematic design is shown in Fig. 9.

### 3. TEST CONDITIONS AND ACCURACY

The investigation was conducted in the Trisonic Tunnel FFA-TVM 500. The tunnel has a square test section of  $50 \times 50 \text{ cm}^2$  with perforated walls for the transonic speed range and a flexible wall nozzle, which allows the Mach number to be varied continuously between 1 and 4. It is a blow-down tunnel, which may be operated with a stagnation pressure up to 12 atmospheres and a stagnation temperature range  $300^\circ\text{K}$  -  $400^\circ\text{K}$ .

Pressure measurements were performed on the parabolic model at  $0^\circ$  angle of incidence and at three positions along the tunnel axis. In addition, the supersonic flow field along a line parallel to the flow direction was measured as the model moved 400 mm along the tunnel axis. For the three-dimensional model measurements were made at  $2,6^\circ$  and  $3,2^\circ$  incidence at two positions along the tunnel axis. The flow field measurements were conducted at two radial distances from the model axis. These distances are  $r/L_0 = 0,375$  and  $0,228$  for the parabolic spindle,  $r/L_0 = 0,558$  and  $0,271$  for the wing-body model. For the latter model the measurements were made in meridian planes spaced at  $5^\circ$  intervals from the plane of symmetry in the range between  $0^\circ$  and  $90^\circ$ . The meridian planes are defined by the angle  $\theta$  with respect to the plane of symmetry. The pressures were recorded almost simultaneously, since the time between the individual measurements was  $1 \cdot 10^{-4}$  sec. Schlieren photographs were taken of the flow field generated by the model and the pressure probe.

The absolute level of accuracy of the results is very difficult to establish, because of the combined effects of the many possible sources of error. A number of precautions were taken, however, to reduce the magnitude and probability of significant errors. The facility instrumentation consists primarily of high-sensitivity pressure measurement devices for determining both stagnation and reference pressures. These pressures were calibrated carefully preceding the investigation. The free-stream properties are considered accurate within the following limits:

$M_\infty$	$\pm 0.01$
$p_{t,\infty}$	$\pm 0.1 \%$

The precision with which local flow quantities can be determined is estimated to be as follows

Errors at $M_\infty = 3.0$	
$M_1$	$\pm 0.07$
$p_{t,1}$	$\pm 1.0 \%$
$\epsilon$	$\pm 0,^{\circ}10$
$\sigma$	$\pm 0,^{\circ}10$

The values of the errors in angles quoted here do not include the influence of the nonuniform flow on the probe. The interaction of the shock with the subsonic flow in front of the probe produces locally large errors; therefore, such a measurement is not accurate there. In addition there is some influence due to Mach number gradients ( $\Delta\epsilon \approx 0,^{\circ}1$ ).

#### 4. EXPERIMENTAL RESULTS

Local flow field parameters for the parabolic spindle, determined from the probe-measured pressures, are presented in Figs. 10 to 17. The pressure distribution on the surface of the model is shown in Fig. 10 for three positions along the tunnel centerline. Local

velocity ratio  $V_1/V_\infty$ , downwash angle  $\epsilon$  and sidewash angle  $\sigma$  for  $r/L_o = 0,375$  are shown in Figs. 11 to 13 and for  $r/L_o = 0,228$  in Figs. 14 to 16. In order to test repeatability several different traverses were made at the probe locations of  $r/L_o = 0,375$  and  $r/L_o = 0,228$ . Hence, the different graphs in the figure series 11 - 13 represent results from four different runs at the location  $r/L_o = 0,375$ . A schlieren photograph of the model and the pressure probe is shown in Fig. 17.

The experimental data for the three-dimensional model are presented in Figs. 18 to 29. Fig. 18 presents the measured values of  $\epsilon$  at  $r/L_o = 0,271$  for different values of  $\theta$ , while Fig. 19 gives the values of  $\sigma$  for the conditions. Figs. 20 and 21 show the same quantities for the distance  $r/L_o = 0,558$ . For several values of  $\theta$ , measurements are available for more than one position of the model along the axis of the tunnel. Figs. 22 and 23 present the result for  $\theta = 0$  and  $r/L_o = 0,271$  and  $0,558$  for the different positions. The figures indicate that the change of position does not affect the experimental results, giving an indication of the uniformity of the flow. The results mentioned are for  $\alpha = 2,^{\circ}6$ . Similar results for  $\sigma$  and  $\epsilon$  at the two distances but for  $\alpha = 3,^{\circ}2$  are given in Figs. 24 to 27.

In addition, schlieren pictures are available for all of these conditions. Figs. 28a and 28b give the photographs at  $\theta = 0^{\circ}$  and  $\theta = 90^{\circ}$ , for  $\alpha = 2,^{\circ}6$ , and Figs. 29a and 29b for  $\alpha = 3,^{\circ}2$ . The photographs give the possibility to locate the position of the shocks, and therefore help in the interpretation of the experimental results.

## 5. CALCULATIONS

With the definition of symbols adopted here, the second order theory gives the intensity and position of the shock wave from the formulae:

$$F = \sqrt{\frac{2r_0}{\beta}} \left( v_0 + \frac{3}{8} \frac{\phi_0}{r_0} + \frac{r}{2r_0} \frac{d\sigma}{d\theta} \right)$$

$$y = x - \beta r + K F \sqrt{2\beta r} + \left( M_\infty^2 - \frac{K}{4} \right) \phi_0 + K r \frac{d\sigma}{d\theta}$$

with

$$\phi_0 = \phi - K r \frac{v^2}{\beta}; \quad v_0 = \left( 1 + \frac{M_\infty^2}{\beta} \epsilon \right) \left( 1 + \frac{K}{\beta} \epsilon \right) v$$

$$\phi = - \frac{1}{\beta} \int_0^x \epsilon(x) dx; \quad r_0 = r \left( 1 - \frac{K}{\beta} \epsilon \right)$$

$$v = \left( 1 - \frac{\epsilon}{\beta} \right) \epsilon;$$

For the derivative  $d\sigma/d\theta$  only approximate values can be obtained, as  $\sigma$  is measured as a function of  $x$  at constant  $\theta$ , and  $\Delta\theta$  is not small ( $\Delta\theta = 5^\circ$ ). In the shock area a line cannot be drawn accurately through the experimental  $\epsilon$  points. Thus, for the wing-body model two alternatives have been investigated at  $r/L_0 = 0,558$ . One has two shocks in the wing area, and a comparison will be made with the corresponding flow picture at  $r/L_0 = 0,271$ . The other has only one shock as an approximation at the wing. In the latter case it will be investigated how the  $F$ -curve and the pressure distribution are changed, when a different number of terms are included in the  $F$ -formula. Only results for  $\theta = 0^\circ$  are given.

Fig. 30 shows the  $F$ -curve for the parabolic spindle. Experimental points from the two different radial distances give an almost identical curve. With the measured values inserted in Whitham's simple formulae, the agreement is less good, and the location changed. A third set has been calculated analytically from the equivalent area of the body.

The chosen  $\epsilon$ -curves, wing-body model, for  $r/L_0 = 0,558$  and  $0,271$ , respectively, are shown in Fig. 31 and Fig. 32. The corresponding  $F$ -function from the second order theory is presented in Figs. 33 and 34. Before the pressure distribution at a certain distance from the body is calculated by the Whitham method, those parts of the  $F$ -curve should be modified (see Ferri [4]), which have a posi-

tive inclination for diminishing F, when the curve is followed in a direction corresponding to increasing x. This can be done through vertical lines, cutting off equal area segments, see Fig. 35 and Fig. 36. The finally obtained F-curves are compared to each other in Fig. 37. They do not coincide but the agreement is good.

The relative pressure rise  $\Delta p/p$  in the main flow direction has been calculated at a distance of  $r/L_o = 200$ . In the far field Whitham's formula will suffice:

$$\frac{\Delta p}{p} = (\kappa M_\infty^2 F) / \left( \frac{2\beta r}{L_o} \right)^{1/2}$$

At reflecting surfaces (ground) a factor is often added to the right side (a common numerical value is 1,8). In Figs. 38 and 39 the final shock position has been drawn. Cutting lines have the inclination  $\{L_o/(2K^2\beta r)\}^{1/2}$ . Evidently, at this distance the two shocks from the wing have combined with each other, but not with the front shock wave. The pressure distribution is presented in Fig. 40. The values from the case  $r/L_o = 0,558$  and from the case  $r/L_o = 0,271$  give practically identical curves.

For  $r/L_o = 0,558$  also an alternate form of the  $\epsilon$  distribution has been considered. It is shown in Fig. 41. The F-curve has been calculated with one, two or three terms, that is, approximately the simple Whitham formula, ditto including  $\phi_0$  and finally ditto including the influence of the angle  $\sigma$ . The derivative is approximated as in Fig. 42. It is zero until 30 mm behind the wing shock wave ( $x=550$ ). Its value has been chosen zero for  $x > 670$ , too, because experimental points are missing.

Fig. 43 shows the F-function. Vertical cuts (see for instance Fig. 44) appear at  $y = 250, 243$  and  $226$  mm respectively. Figs. 45 and 46 yield the conclusion that wing and front shocks have combined at a distance  $r/L_o = 200$ , when only one or two terms are considered. When three-dimensional effects are included, however, it is evident from Fig. 47 that there are still two separate shocks. The corresponding pressure distribution is presented in Fig. 48.

From the foregoing examples it is clear that small variations of the chosen  $\epsilon$  distribution and shock positions do not have a great influence on the F-curve, and much less so on the pressure distribution. Here, only the case  $\theta=0$  has been considered. At other values of  $\theta$  the shock configuration may be more complicated. Further, it is changing fast with varying  $\theta$ . However, by means of schlieren pictures, close measuring points and considering Edney's [5] investigation of shock-influenced pressure measuring sonds, a satisfactory  $\epsilon$ -curve can be obtained. It is important that the angle  $\sigma$  is measured with small enough errors, so  $d\sigma/d\theta$  can be calculated accurately. This derivative has a direct influence on F. It has a direct as well as an indirect influence on y. In the latter case these two effects always operate in the same direction.

## 6. CONCLUSION

The second order theory of Landahl et al, complemented with experimentally measured values of some components in the near field, gives an appropriate method for calculation of the F-function - and hence the strength and position of the shock waves - at an arbitrary distance from a body with complicated geometry.

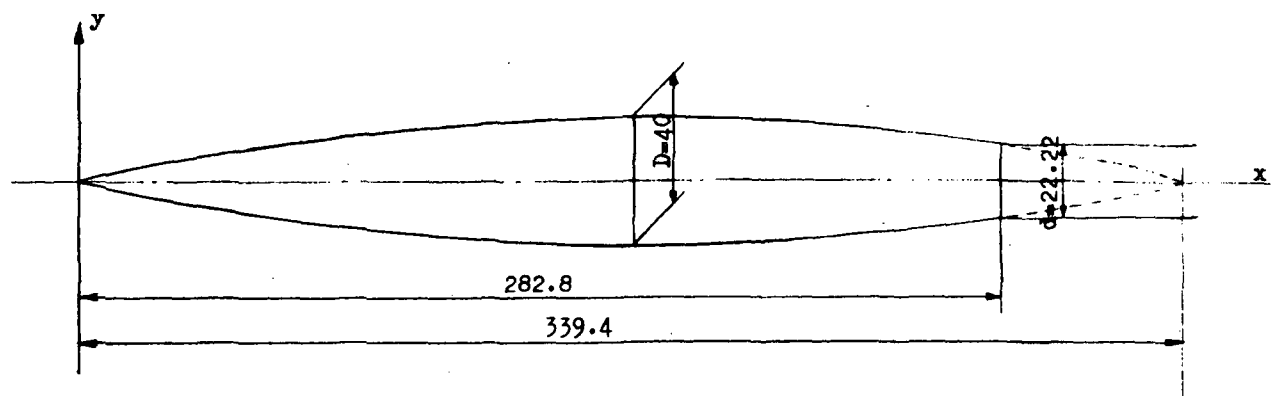
## REFERENCES

1. Landahl  
Ryhming  
Löfgren  
  
Nonlinear effects on sonic boom intensity.  
NASA SP 255, 1970.
2. Whitham  
  
The flow pattern of a supersonic projectile.  
Comm. Pure & Appl. Math. Aug. 1952.
3. Landahl  
Ryhming  
Sörensen  
Drougge  
  
A new method for determining sonic boom strength  
from near-field measurements.  
NASA SP 255, 1970.
4. Ferri  
Wang  
Sörensen  
  
Experimental verification of low sonic boom  
configuration. New York Univ. NYA-AA-71-19, 1971.
5. Edney  
  
Anomalous heat transfer and pressure distribu-  
tion on blunt bodies at hypersonic speeds in  
the presence of an impinging shock.  
Aeron. Res. Inst., Sweden, FFA Rep 115, 1968

Table 1

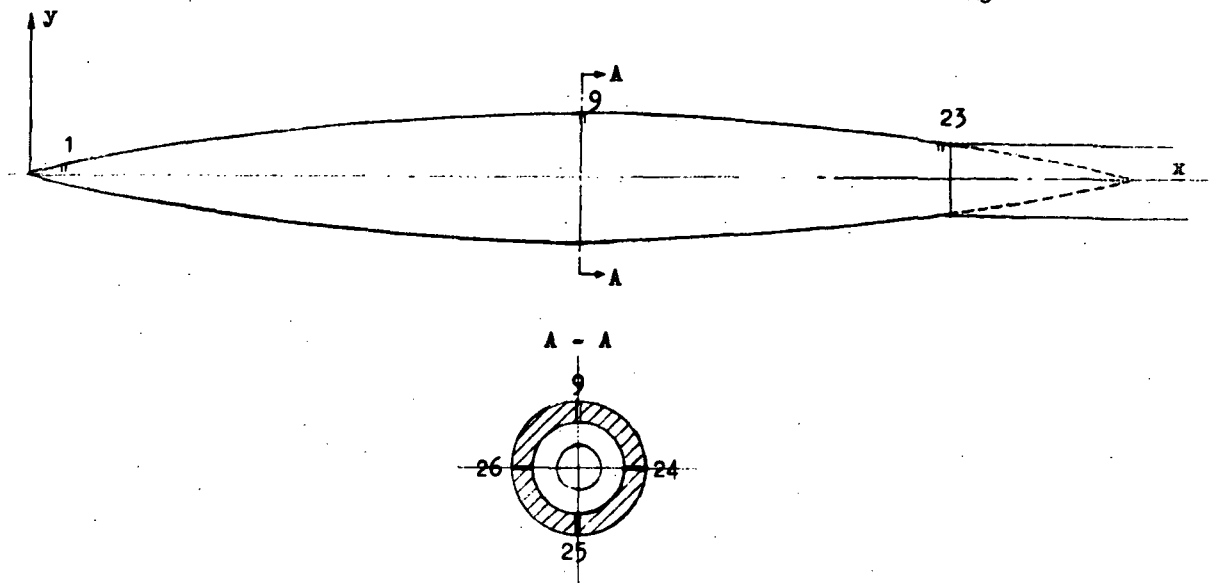
STATION	FUSELAGE RADIUS (FT)	TOTAL EQUIV. AREA AE	FUSELAGE AREA AF(SQ.FT.)	WING AREA. AW(SQ.FT.)	FUSELAGE LIFT AFW(SQ.FT.)	LIFT DUE TO WING XLEF	LIFT DUE TO FUSELAGE XLEW	LIFT DUE TO WING+FUSE. XLEX	MODEL SCALE STATION RADIUS IN.(IN.) RW(IN.)
.00000	.00000	.00000	.00000	.00000	.00000	.00000	.00000	.00000	.000 .000
5.00000	1.03617	3.95640	3.37297	.00000	3.37297	1.8343	.00000	.18343	.181 .037
10.00000	1.64482	8.96156	6.49935	.00000	6.49935	.46222	.00000	.46222	.361 .059
15.00000	2.15532	15.38745	14.59299	.00000	14.59299	.79366	.00000	.79366	.542 .078
20.00000	2.61099	22.58173	21.41702	.00000	21.41702	1.16471	.00000	1.16471	.723 .094
25.00000	3.02978	30.40677	28.83848	.00000	28.83848	1.56831	.00000	1.56831	.903 .109
30.00000	3.42136	38.77446	36.77455	.00000	36.77455	1.99989	.00000	1.99989	1.088 .124
35.00000	3.79166	47.68203	45.16580	.00000	45.16580	2.45623	.00000	2.45623	1.265 .137
40.00000	4.14468	56.90239	53.96780	.00000	53.96780	2.93489	.00000	2.93489	1.445 .150
45.00000	4.48325	66.57846	63.44452	.00000	63.44452	3.43396	.00000	3.43396	1.626 .162
50.00000	4.80948	76.62030	72.66841	.00000	72.66841	3.95189	.00000	3.95189	1.807 .174
55.00000	5.12499	87.00248	82.51557	.00000	82.51557	4.48740	.00000	4.48740	1.987 .185
60.00000	5.43107	97.70546	92.66605	.00000	92.66605	5.03941	.00000	5.03941	2.168 .196
65.00000	5.72675	108.70971	103.10272	.00000	103.10272	5.60698	.00000	5.60698	2.349 .207
70.00000	6.01889	120.00000	113.81069	.00000	113.81069	6.18931	.00000	6.18931	2.529 .217
75.00000	6.30049	131.49169	124.70909	.00000	124.70909	6.78199	.00000	6.78199	2.710 .228
80.00000	6.57290	143.10721	135.72608	.00000	135.72608	7.38112	.00000	7.38112	2.891 .238
85.00000	6.83727	154.88436	146.86166	.00000	146.86166	7.98670	.00000	7.98670	3.071 .247
90.00000	7.09435	166.71455	158.11582	.00000	158.11582	8.59873	.00000	8.59873	3.252 .256
95.00000	7.34506	178.70578	169.48857	.00000	169.48857	9.21721	.00000	9.21721	3.433 .265
100.00000	7.58597	190.82203	180.97989	.00000	180.97989	9.89218	.00000	9.89218	3.613 .274
105.00000	7.82964	203.06332	192.58981	.00000	192.58981	10.47351	.00000	10.47351	3.794 .283
110.00000	8.06552	215.42965	204.31830	.00000	204.31830	11.11134	.00000	11.11134	3.975 .291
115.00000	8.29503	227.92111	216.16539	.00000	216.16539	11.75561	.00000	11.75561	4.155 .300
120.00000	8.52152	240.53740	228.13106	.00000	228.13106	12.40633	.00000	12.40633	4.336 .318
125.00000	8.74431	253.27842	240.21531	.00000	240.21531	13.06351	.00000	13.06351	4.517 .316
130.00000	8.95296	268.14576	251.81550	.00000	251.81550	13.69457	.00000	13.69457	4.697 .320
135.00000	9.13796	279.13587	262.33020	.00000	262.33020	14.26617	.00000	14.26617	4.878 .330
140.00000	9.30072	292.62330	271.75848	.00000	271.75848	14.77890	.00000	14.77890	5.059 .336
145.00000	9.44239	305.49467	280.10065	.00000	280.10065	15.23257	.00000	15.23257	5.239 .341
150.00000	9.56392	318.86146	287.35672	.00000	287.35672	15.62717	.00000	15.62717	5.420 .346
155.00000	9.66600	332.35338	293.82362	.00382	293.82362	16.96255	.00000	16.96255	5.601 .349
160.00000	9.72976	345.96973	287.40892	1.26696	286.67586	16.17384	31.12000	47.29384	5.781 .352
165.00000	9.74122	359.71144	298.11031	6.76267	302.85958	16.21198	40.46653	56.85851	5.962 .352
170.00000	9.70299	373.57817	295.71713	10.27867	306.05919	16.08460	51.49326	67.52807	6.143 .351
175.00000	9.61763	387.56946	290.99351	17.66304	308.25656	15.80320	63.51020	79.31340	6.323 .348
180.00000	9.48822	401.68673	382.62697	20.63156	309.45855	15.38083	76.84735	92.22618	6.504 .343
185.00000	9.31796	415.92857	372.76670	36.87343	309.69013	14.83373	91.45649	106.28842	6.685 .337
190.00000	9.11026	430.25943	40.74234	48.04102	308.78337	14.17982	107.33224	121.51206	6.865 .329
195.00000	8.86890	446.76753	47.10927	59.78972	306.86899	13.43842	124.48000	137.91842	7.046 .320
200.00000	8.59789	459.40496	512.23889	71.63831	303.87659	12.62970	142.89796	155.52765	7.227 .311
205.00000	8.30156	474.14622	416.50557	83.26044	299.78001	11.77411	162.58612	174.36023	7.407 .300
210.00000	7.98447	489.01383	200.28223	94.29467	294.57890	10.89185	183.54494	194.43633	7.588 .289
215.00000	7.65147	504.00596	183.92336	104.38955	288.22991	10.06226	205.77506	215.77532	7.769 .276
220.00000	7.30760	519.12833	167.76002	112.98305	280.78706	9.12392	229.27183	238.39526	7.949 .264

225.00000	8.95510	534.36463	152.10056	19.95144	272.05199	8.27161	254.04081	262.31242	8.130 .251
230.00000	8.60533	549.73156	137.19335	124.99733	262.19067	7.46092	260.07999	287.5091	8.311 .239
235.00000	8.26364	365.22373	123.25469	187.87677	281.13146	6.70290	307.38039	314.09228	8.491 .226
240.00000	5.92921	580.84063	110.44454	126.42117	238.66571	6.00625	335.96898	341.97522	8.672 .214
245.00000	5.60980	596.58317	98.86529	126.32257	225.38786	6.37654	365.81877	371.19531	8.853 .203
250.00000	5.30930	612.45046	88.59741	122.13829	210.69570	6.81597	396.93877	401.75474	9.033 .192
255.00000	5.03033	628.44276	79.49844	115.29517	194.79061	6.42316	429.32696	433.65213	9.214 .182
260.00000	4.77345	644.56007	71.58379	106.09401	177.67780	5.89290	462.98938	466.88229	9.395 .172
265.00000	4.53641	660.00244	64.65091	94.71567	159.36658	5.31588	497.91999	501.43587	9.575 .164
270.00000	4.31300	677.16965	58.43982	81.43113	139.87099	5.17810	534.12081	537.29891	9.756 .156
275.00000	4.09148	693.06226	52.59094	66.61950	119.21044	5.86003	571.59183	578.45185	9.937 .148
280.00000	3.85181	710.27976	46.61008	56.80166	97.41195	5.25477	610.33305	612.86782	10.117 .139
285.00000	3.55963	727.02827	39.60701	34.70598	74.51299	5.16460	650.39448	652.50928	10.298 .129
290.00000	3.14980	742.88941	31.17004	19.39856	50.56660	4.69510	691.62611	693.32121	10.479 .114
295.00000	2.46238	760.02238	19.6390	6.60978	25.56774	4.03669	734.17795	738.21964	10.659 .089
300.00	0.0	778.00	0.0	0.0	0.0	0.0	778.00	778.00	10.840 0.0



x mm	y mm	x mm	y mm
0.000	0	144.704	29.566
4.704	1.094	149.704	19.722
9.704	2.222	154.704	19.844
14.704	3.316	159.704	19.931
19.704	4.375	164.704	19.983
24.704	5.399	169.704	20.000
29.704	6.389	174.704	19.983
34.704	7.344	179.704	19.931
39.704	8.264	184.704	19.844
44.704	9.149	189.704	19.722
49.704	10.000	194.704	19.566
54.704	10.816	199.704	19.375
59.704	11.597	204.704	19.149
64.704	12.344	209.704	18.889
69.704	13.056	214.704	18.594
74.704	13.733	219.704	18.264
79.704	14.375	224.704	17.899
84.704	14.983	229.704	17.500
89.704	15.556	234.704	17.066
94.704	16.094	239.704	16.597
99.704	16.597	244.704	16.094
104.704	17.066	249.704	15.556
109.704	17.500	254.704	14.983
114.704	17.899	259.704	14.375
119.704	18.264	264.704	13.733
124.704	18.594	269.704	13.056
129.704	18.889	274.704	12.344
134.704	19.149	279.704	11.597
139.704	19.375	282.840	11.111

Fig 1 Parabolic model



orifices number	x mm	orifices number	x mm
1	9.70	13	223.70
2	24.70	14	231.70
3	39.70	15	239.70
4	54.70	16	244.70
5	69.70	17	249.70
6	89.70	18	254.70
7	115.70	19	259.70
8	141.70	20	264.70
9	169.70	21	269.70
10	183.70	22	274.70
11	197.70	23	279.70
12	210.70	24	169.70
		25	169.70
		26	169.70

Fig 2 Coordinates of the pressure orifices

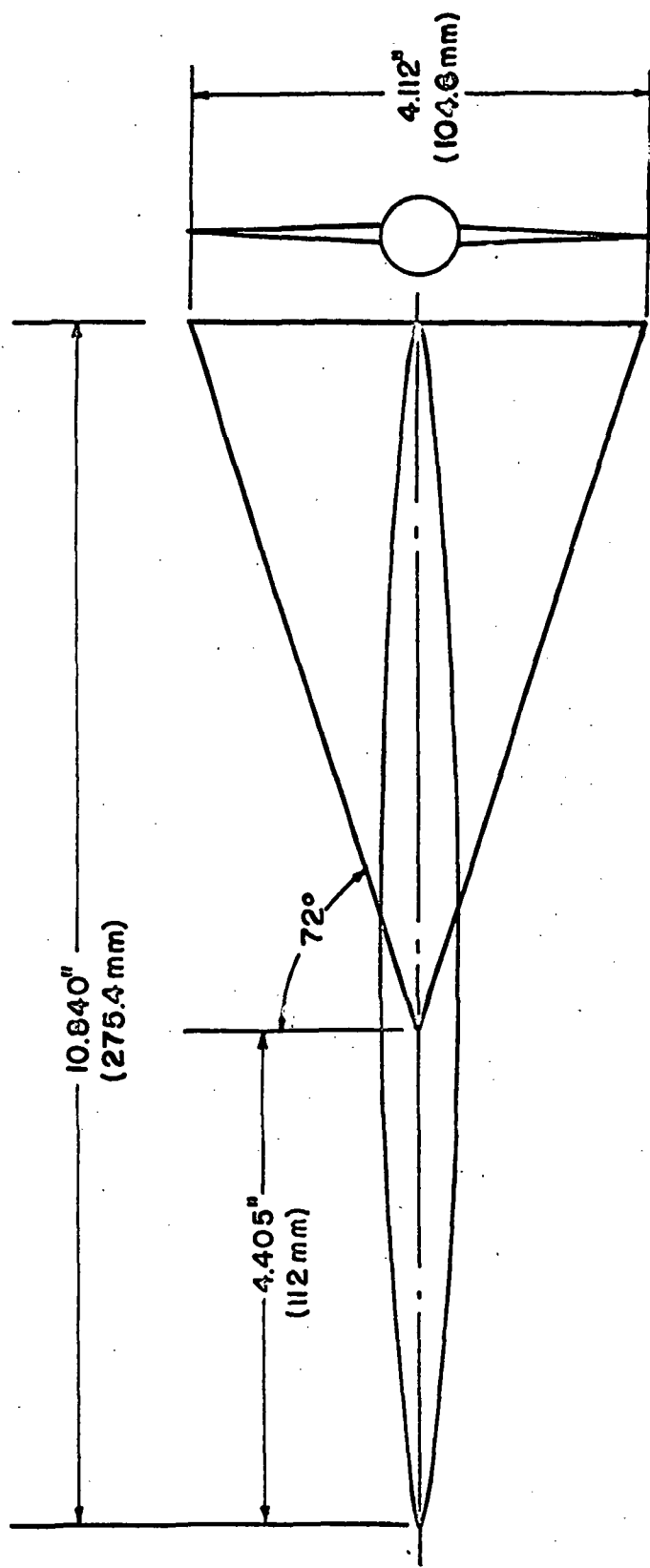


Fig 3 Design of airplane configuration

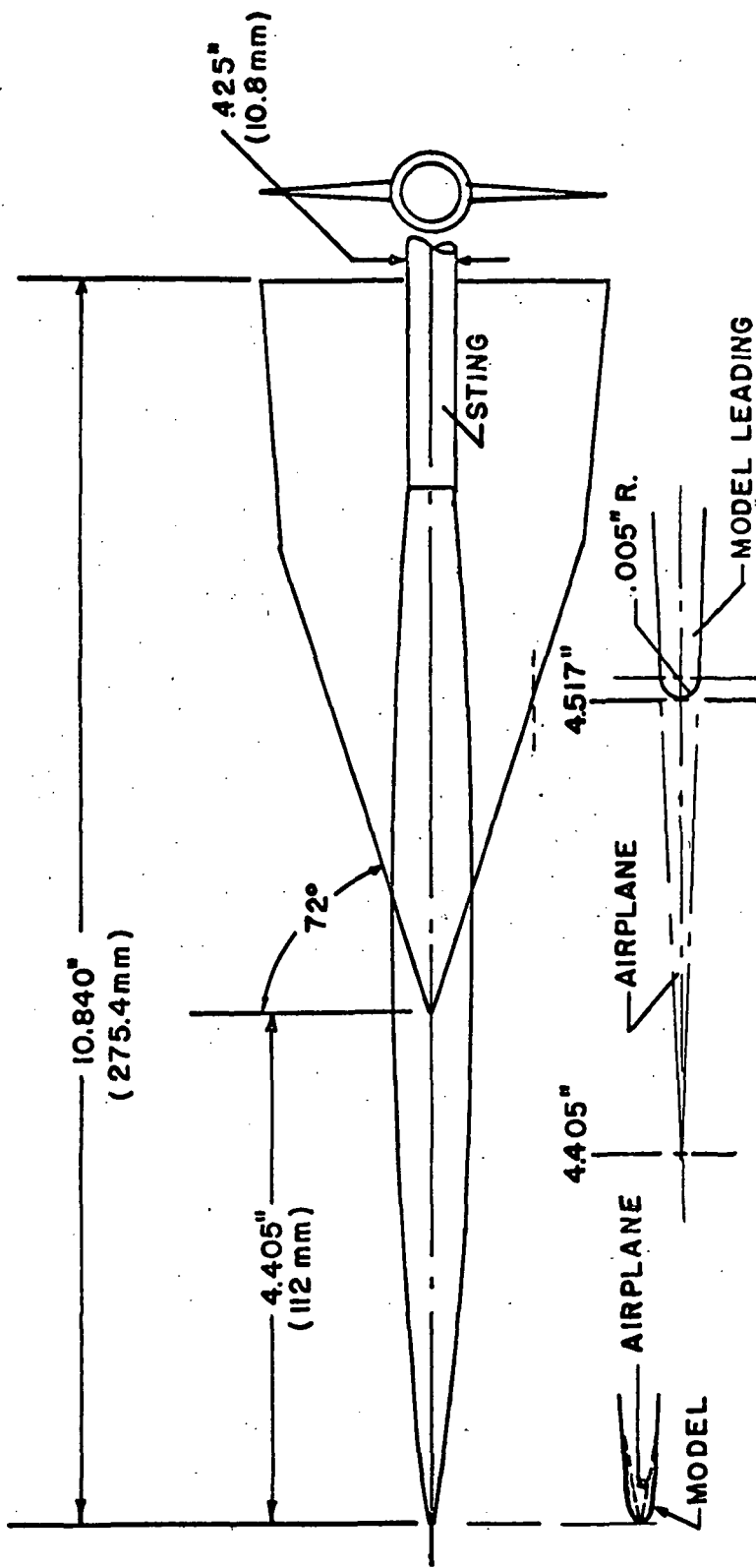


Fig. 4 Wing body model design

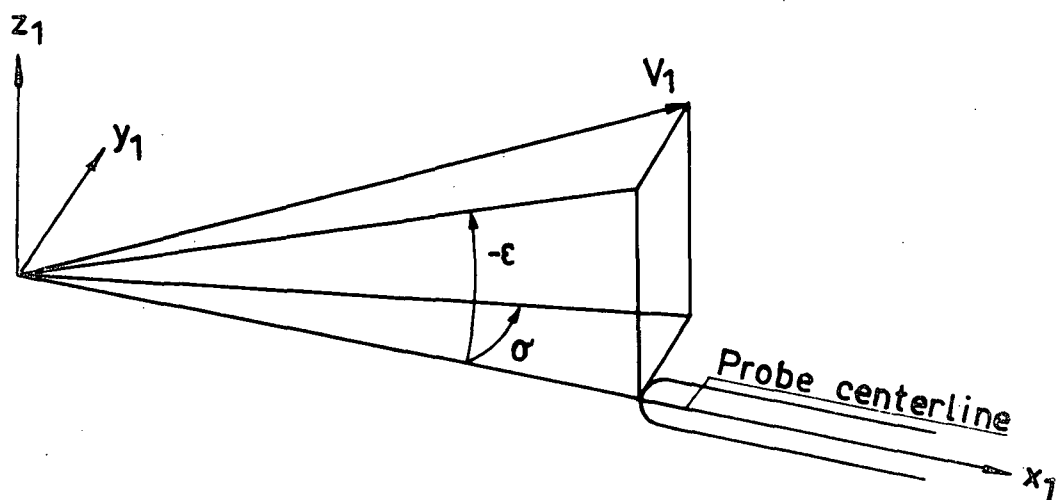
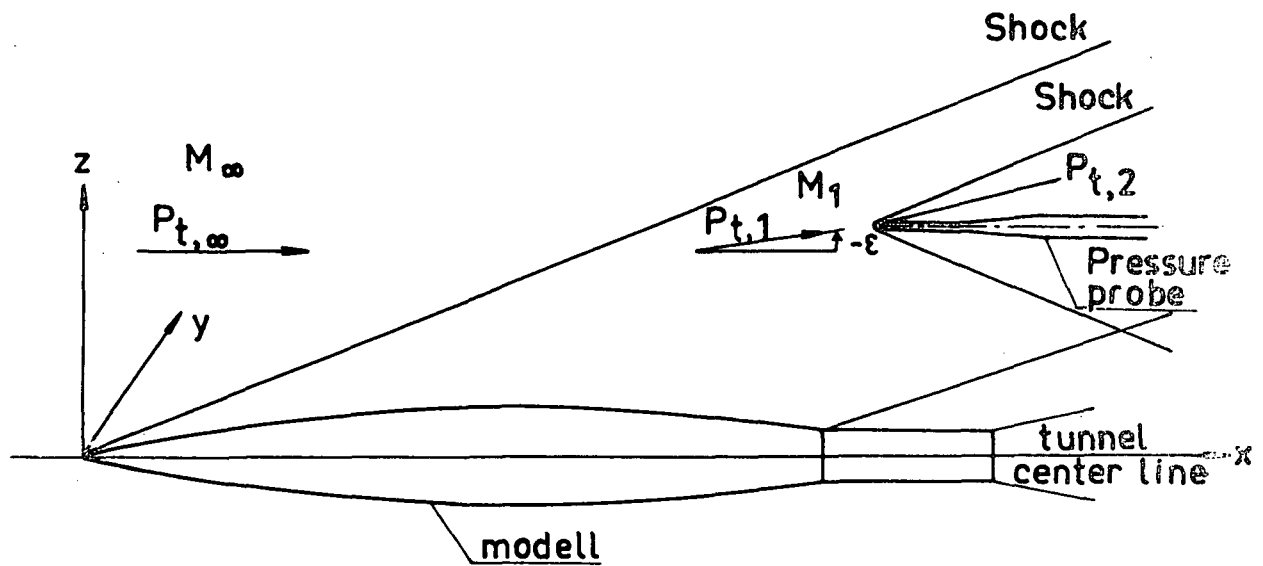


Fig 5 Sketch showing physical flow characteristics

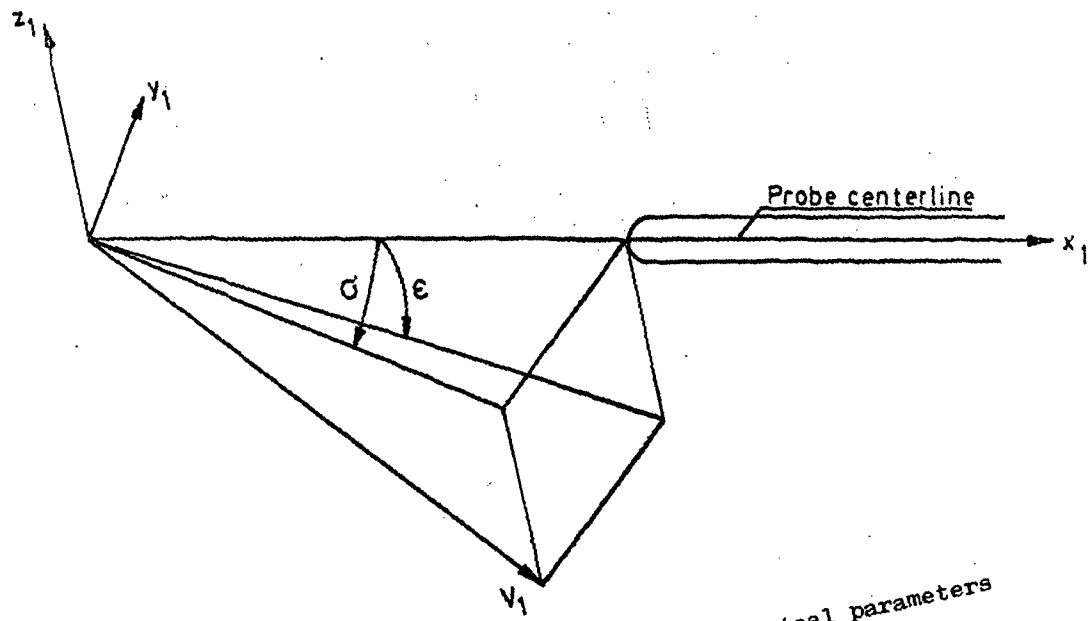
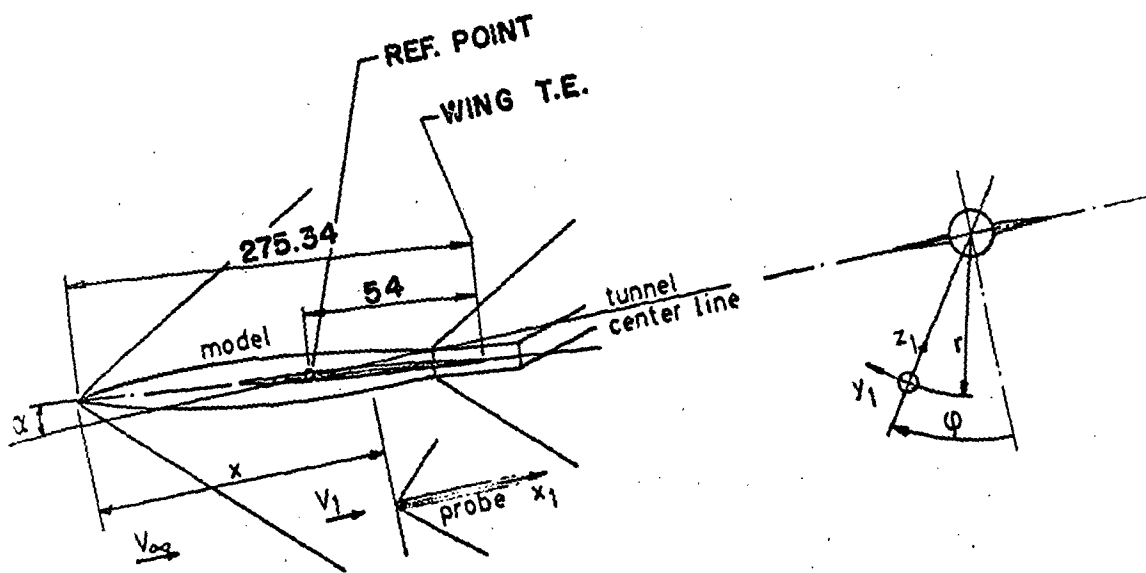


Fig 6 Schematic indication of geometrical parameters

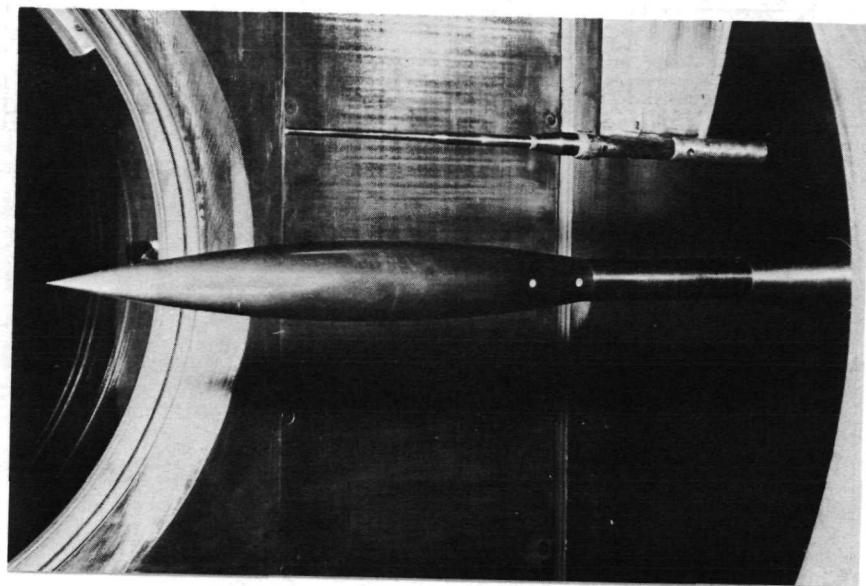


Fig 7. Photograph of model and probe

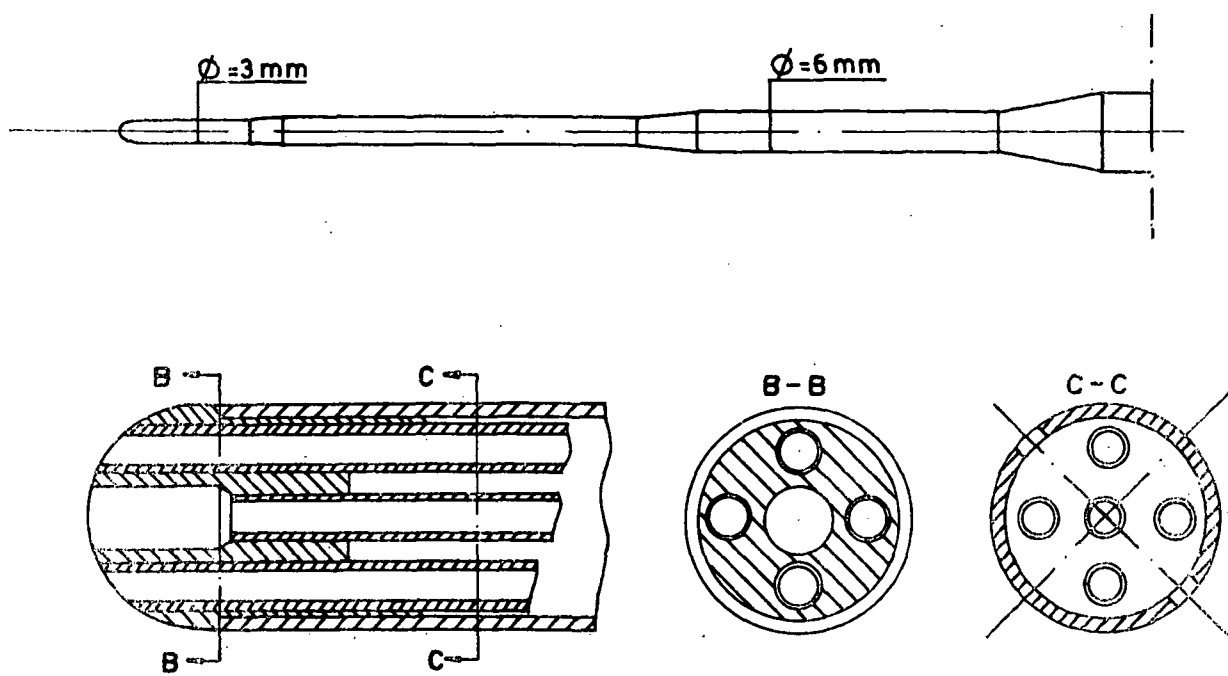


Fig 8. Design of yaw probe

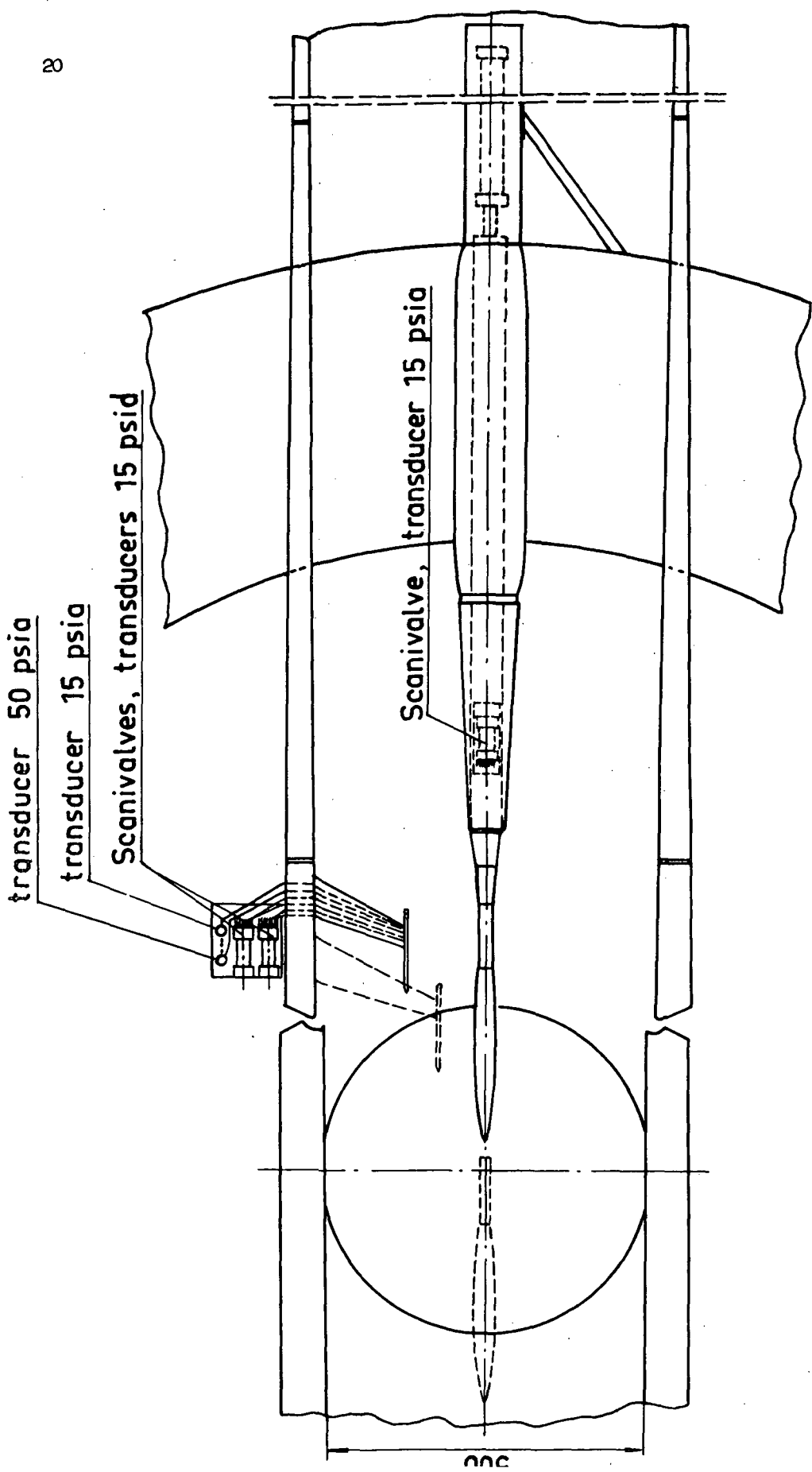


Fig 9 Schematical view of test set-up

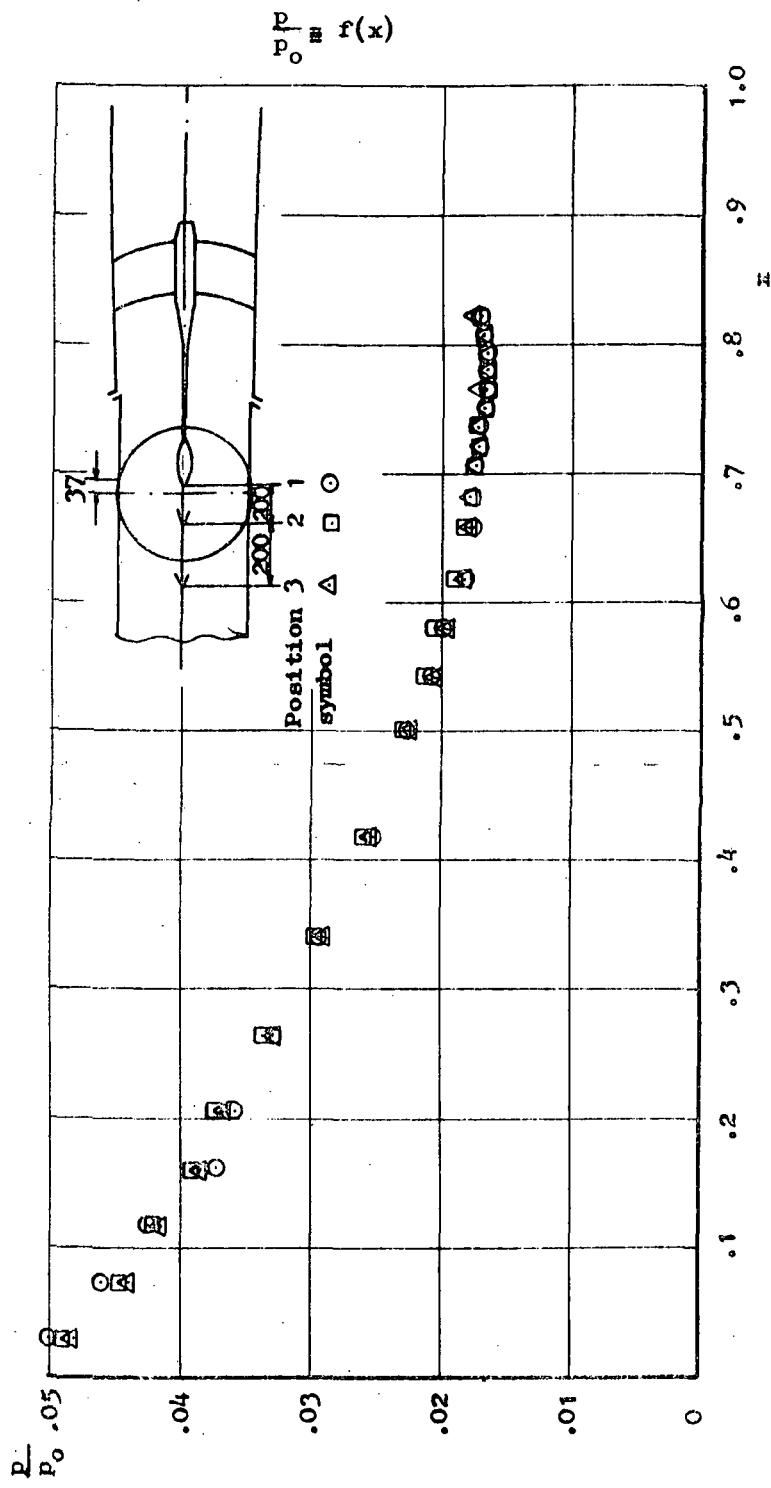
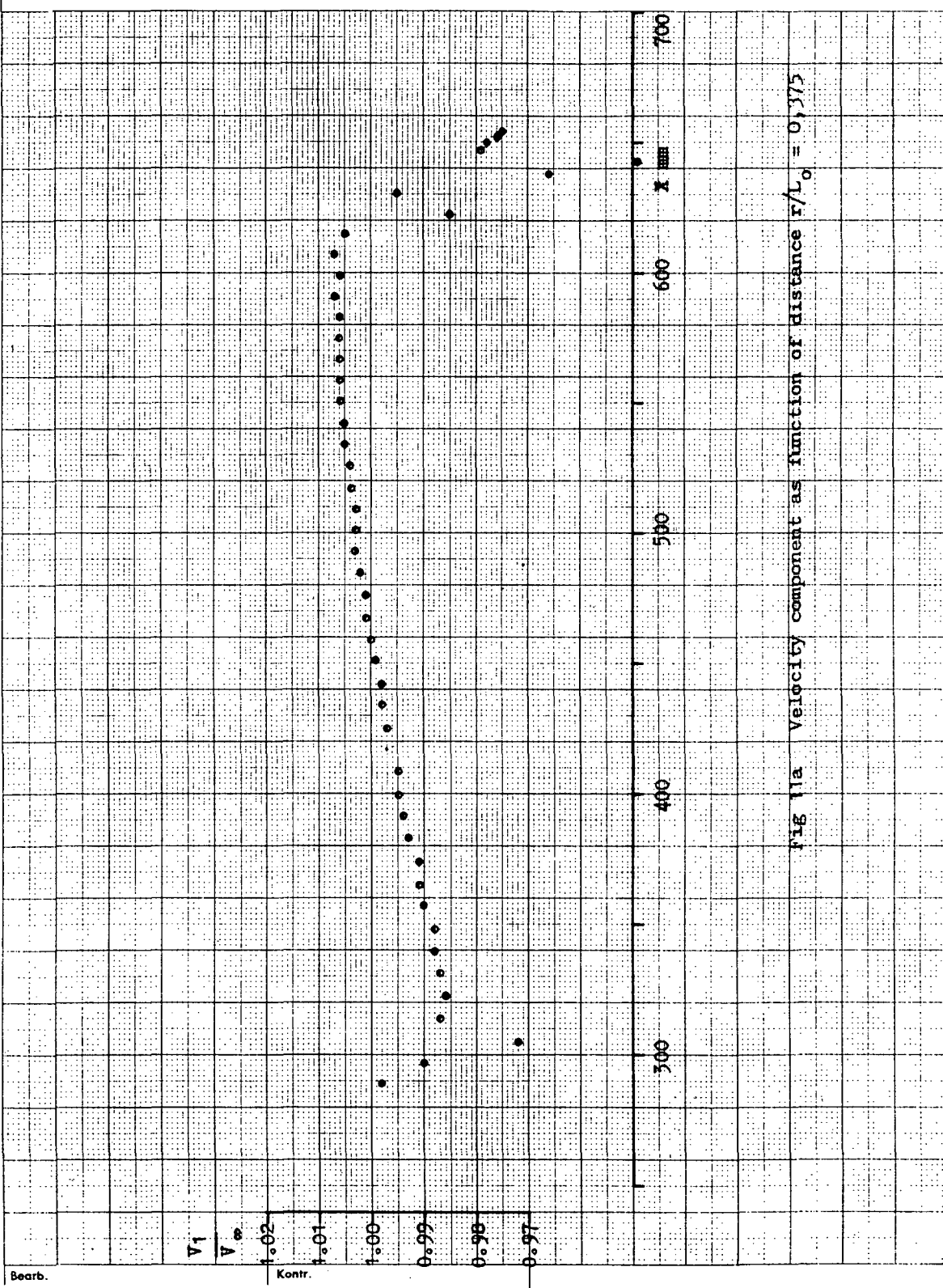
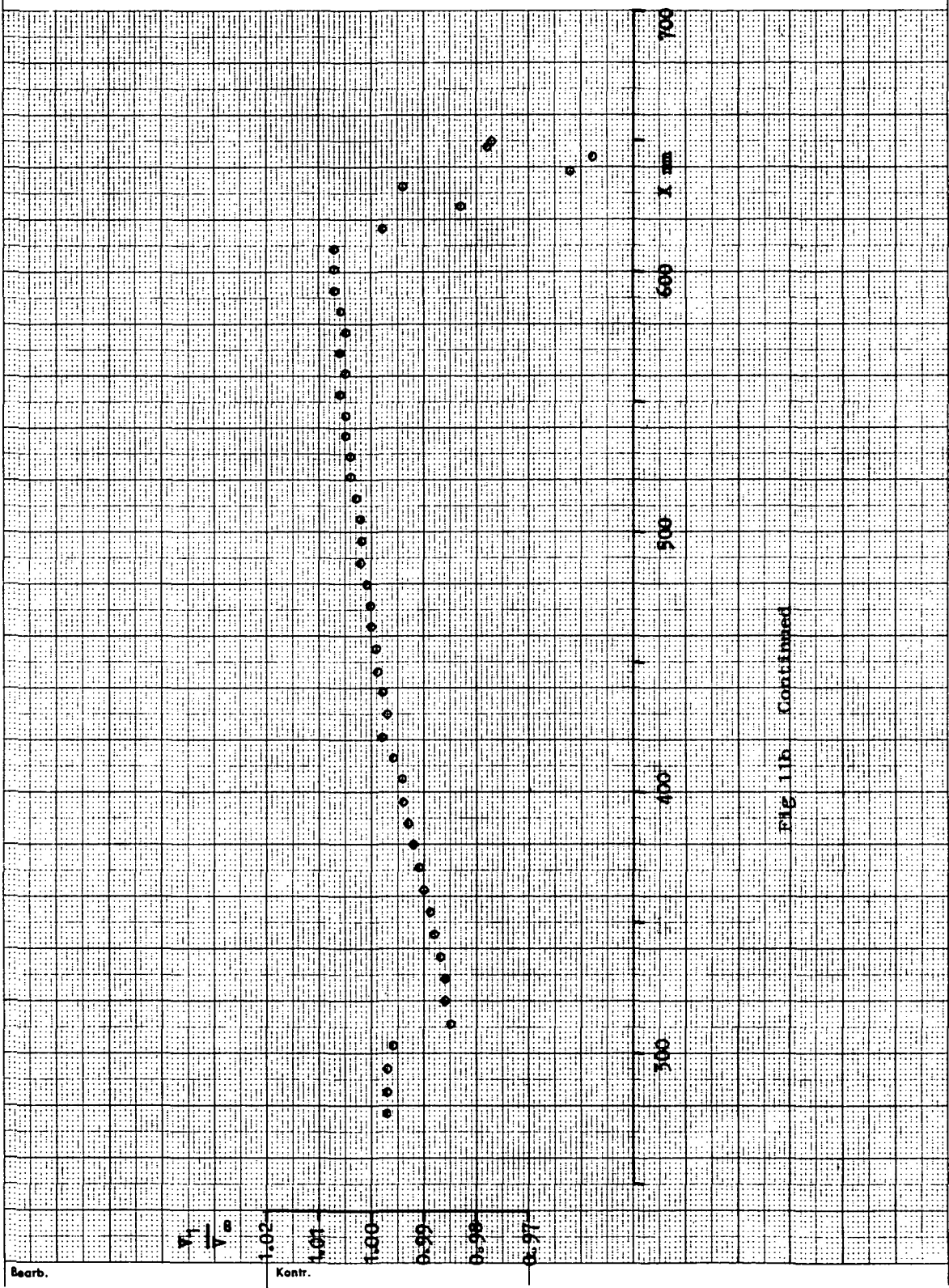


Fig. 10. Pressure distribution on the model

Logg 374



Logg 376



Logg 377

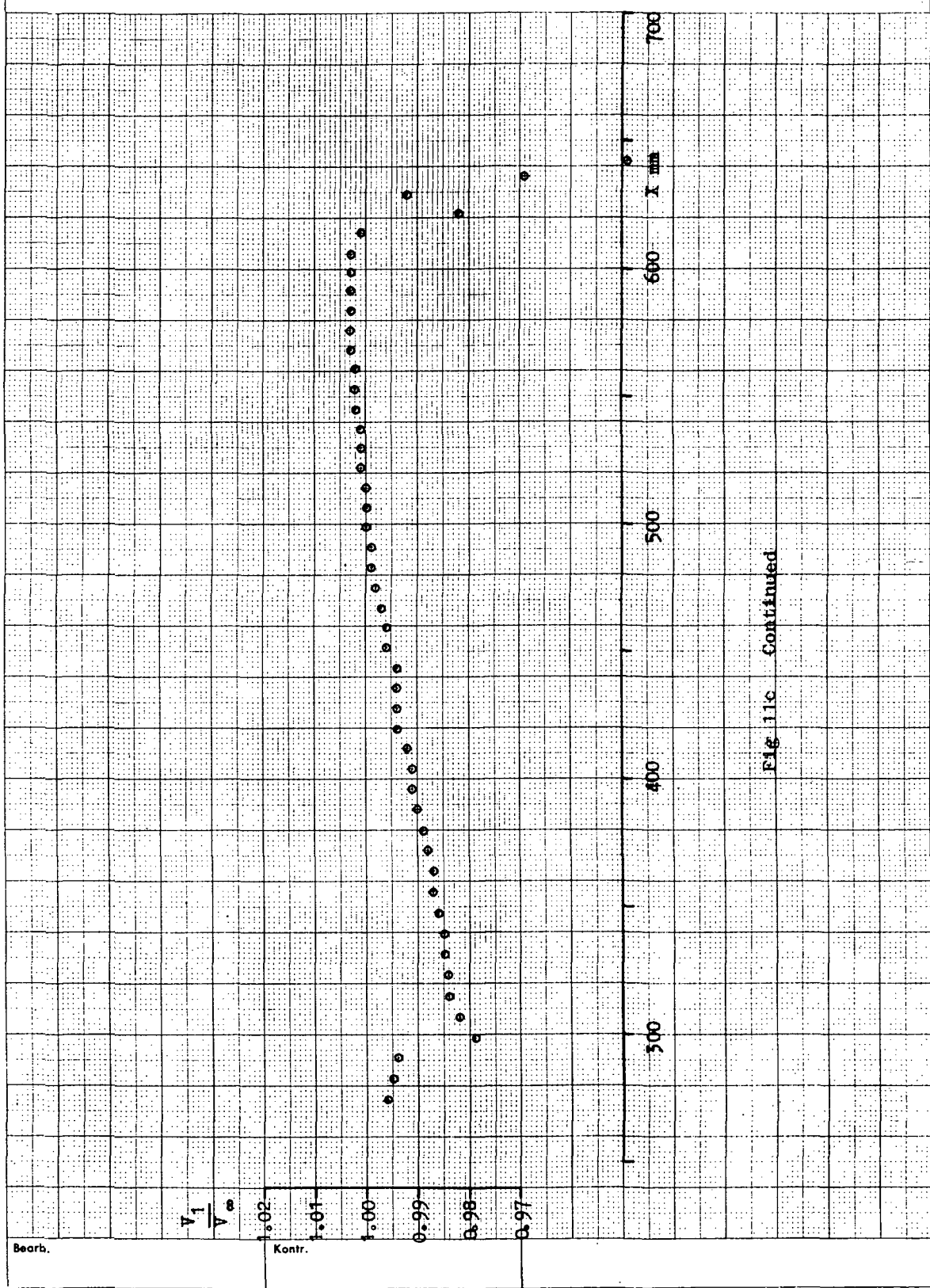
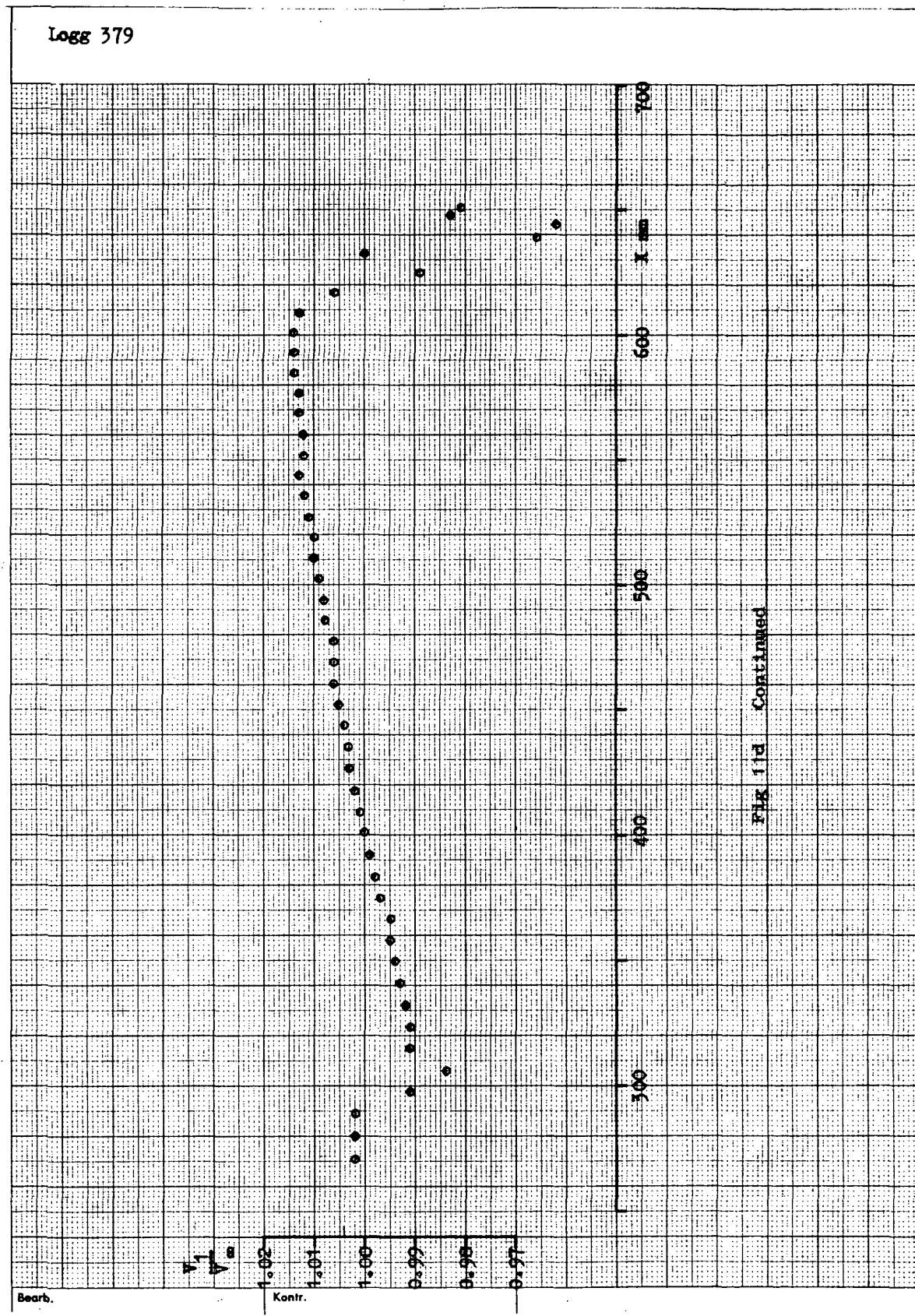
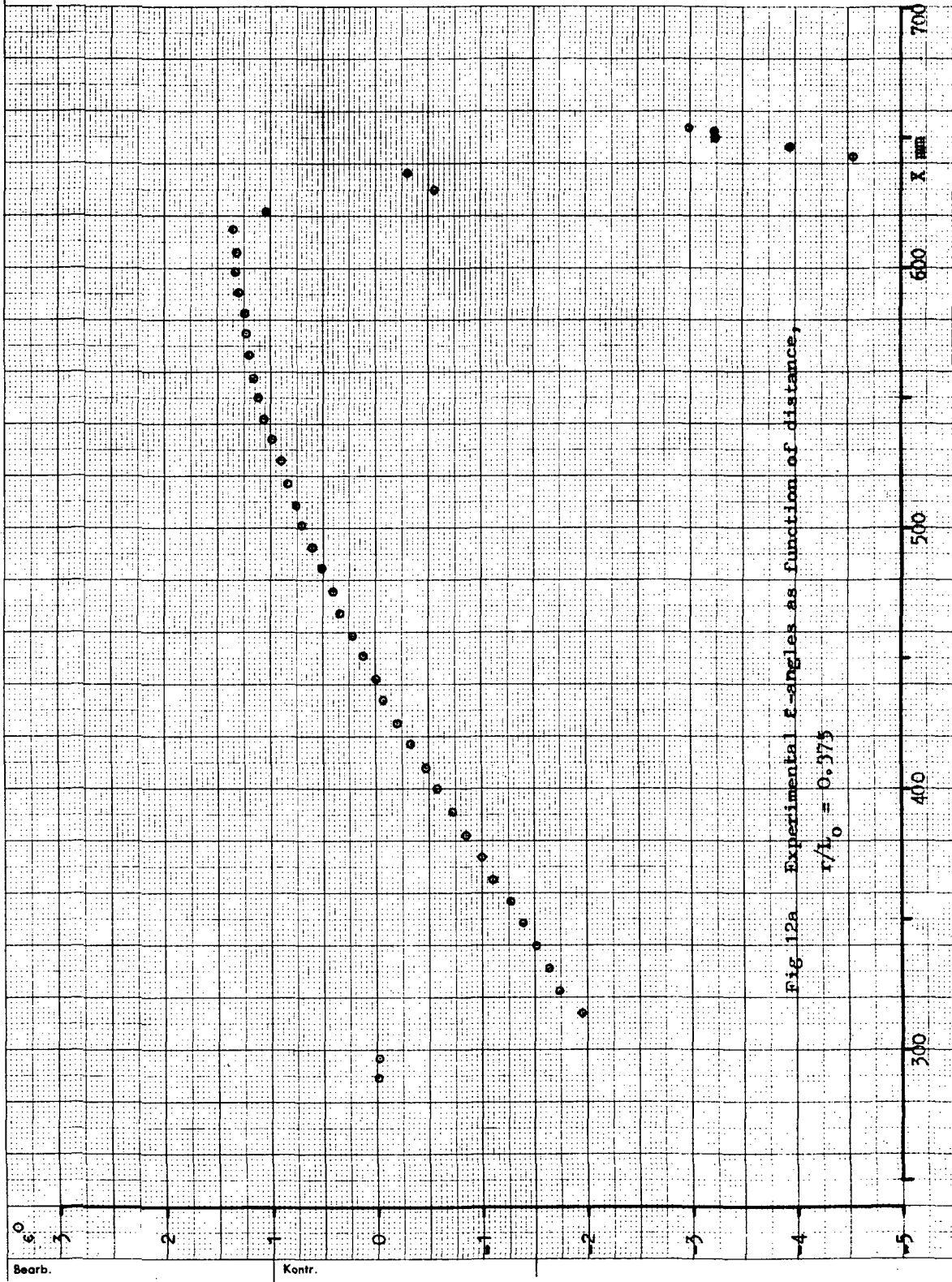


FIG. 11c Continued



Logg 374



Logg 376

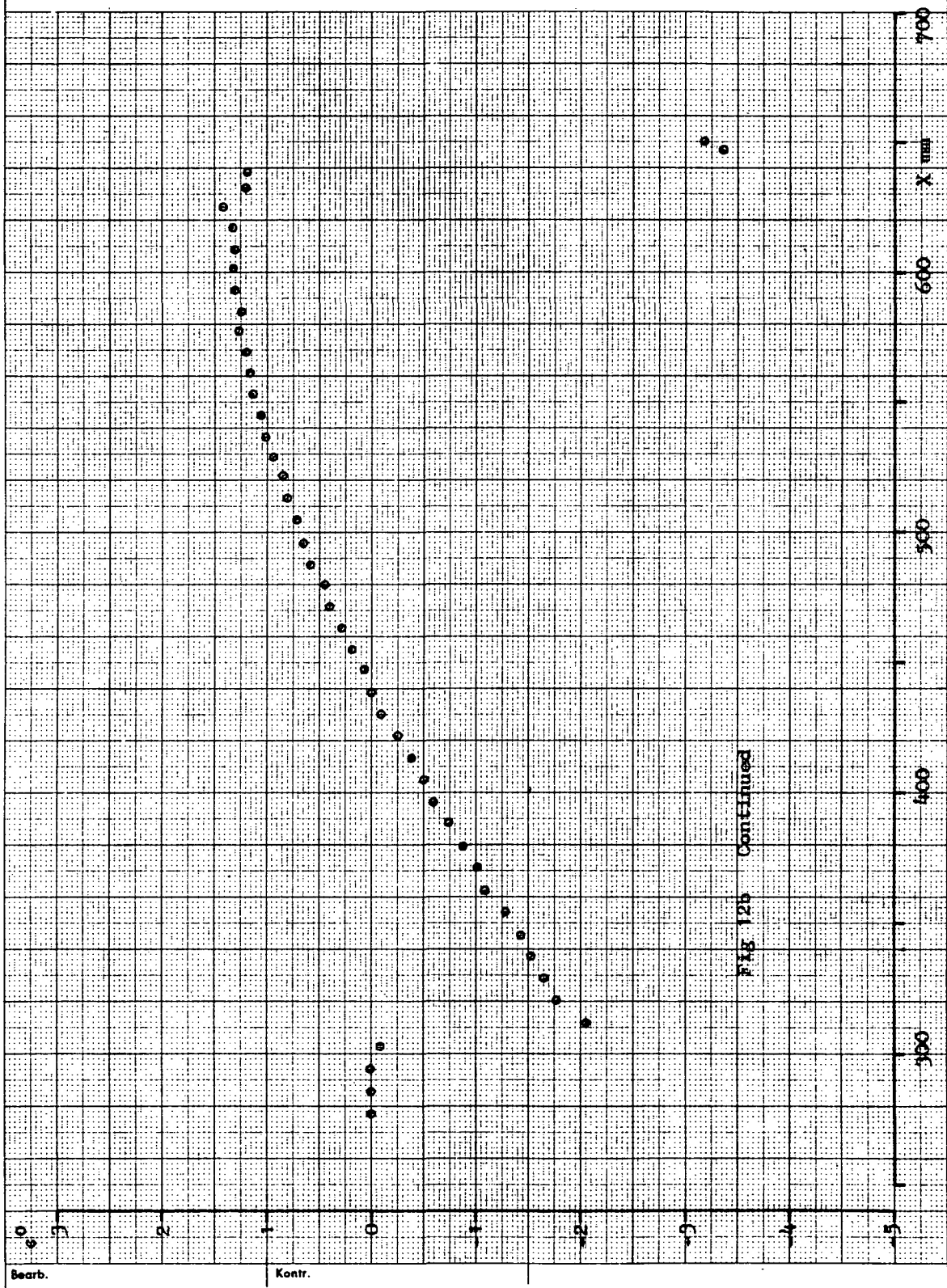


FIG 12b - continued

Logg 377

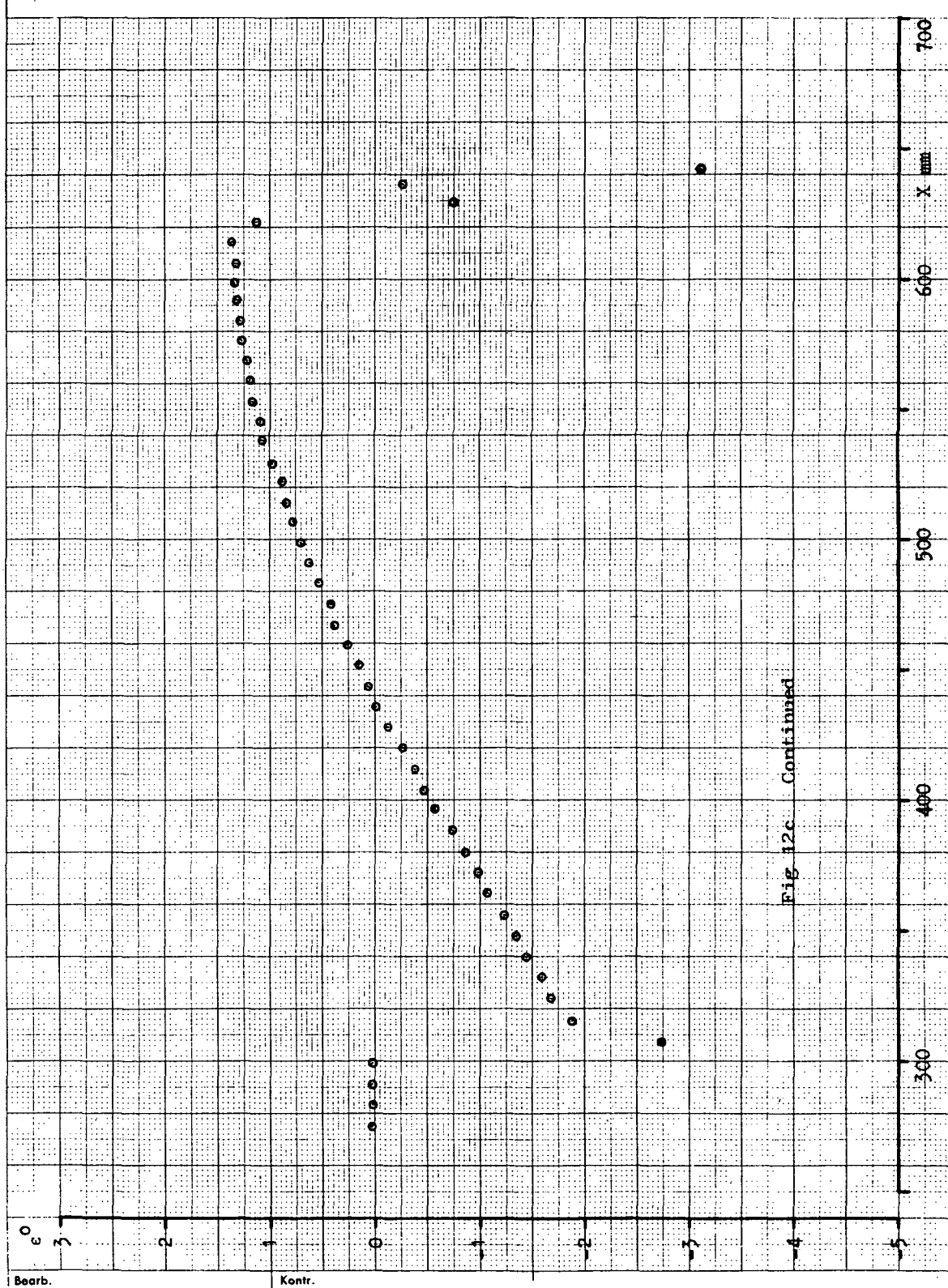
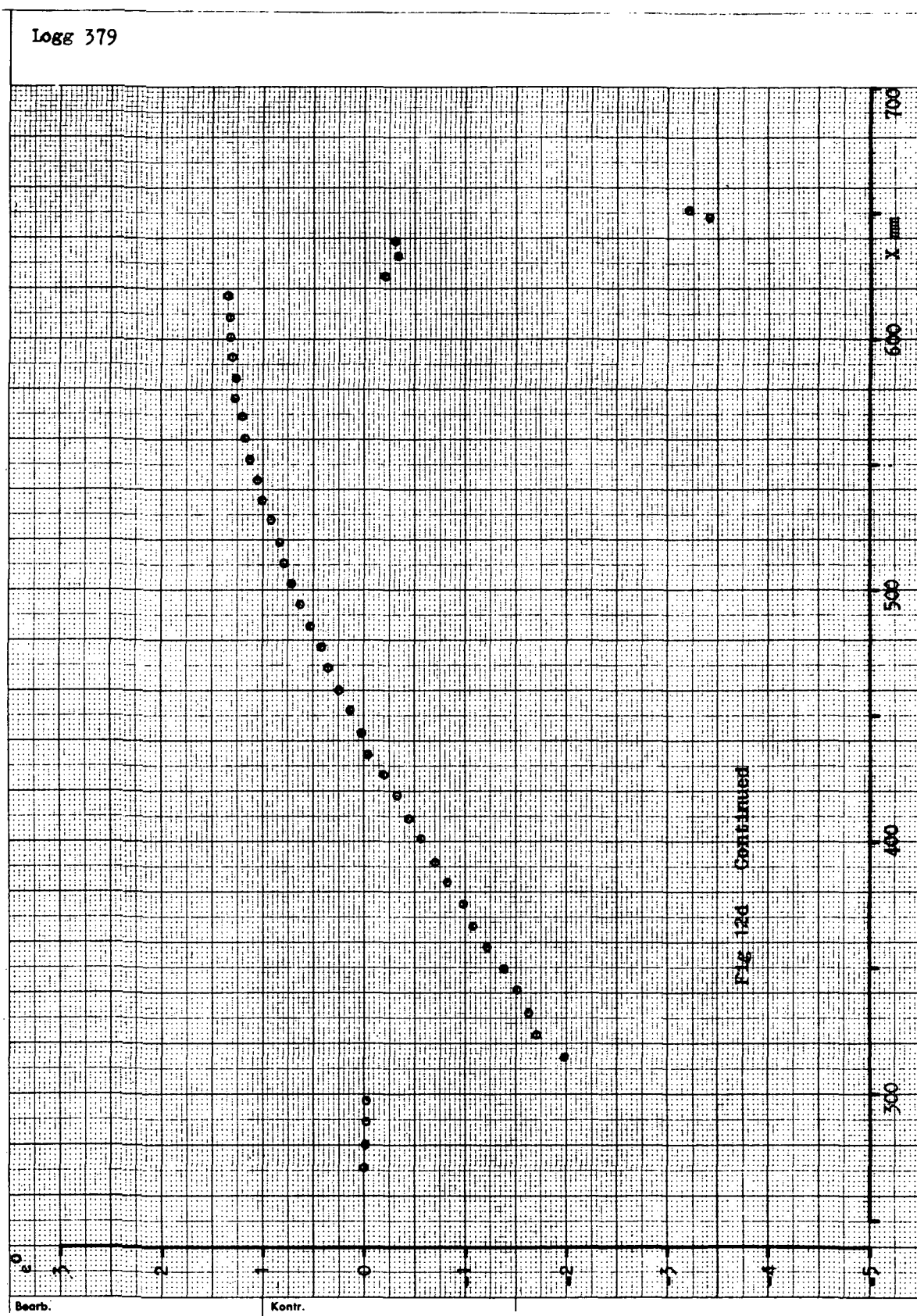


Fig. 12c. Continued



Logg 374

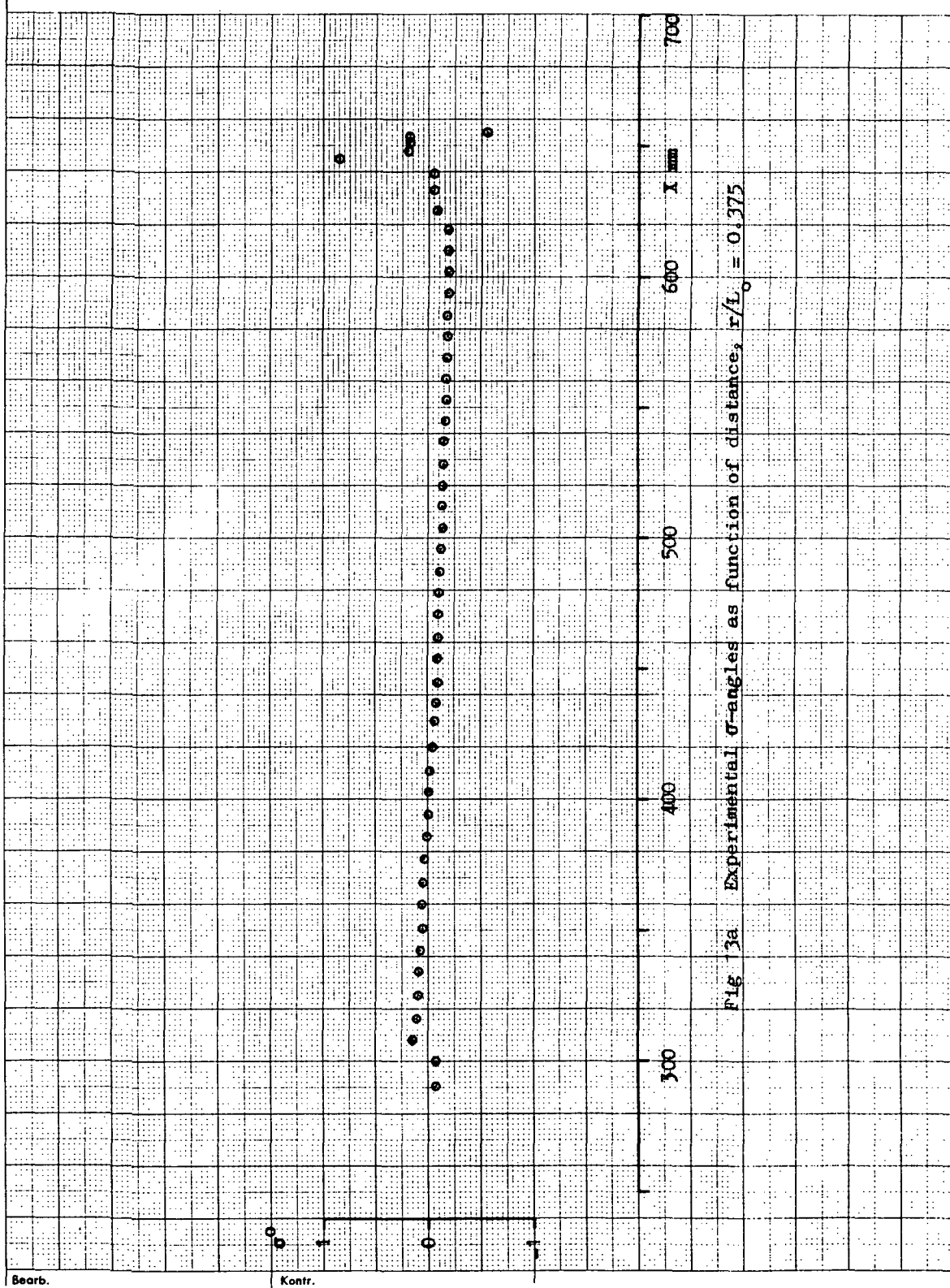
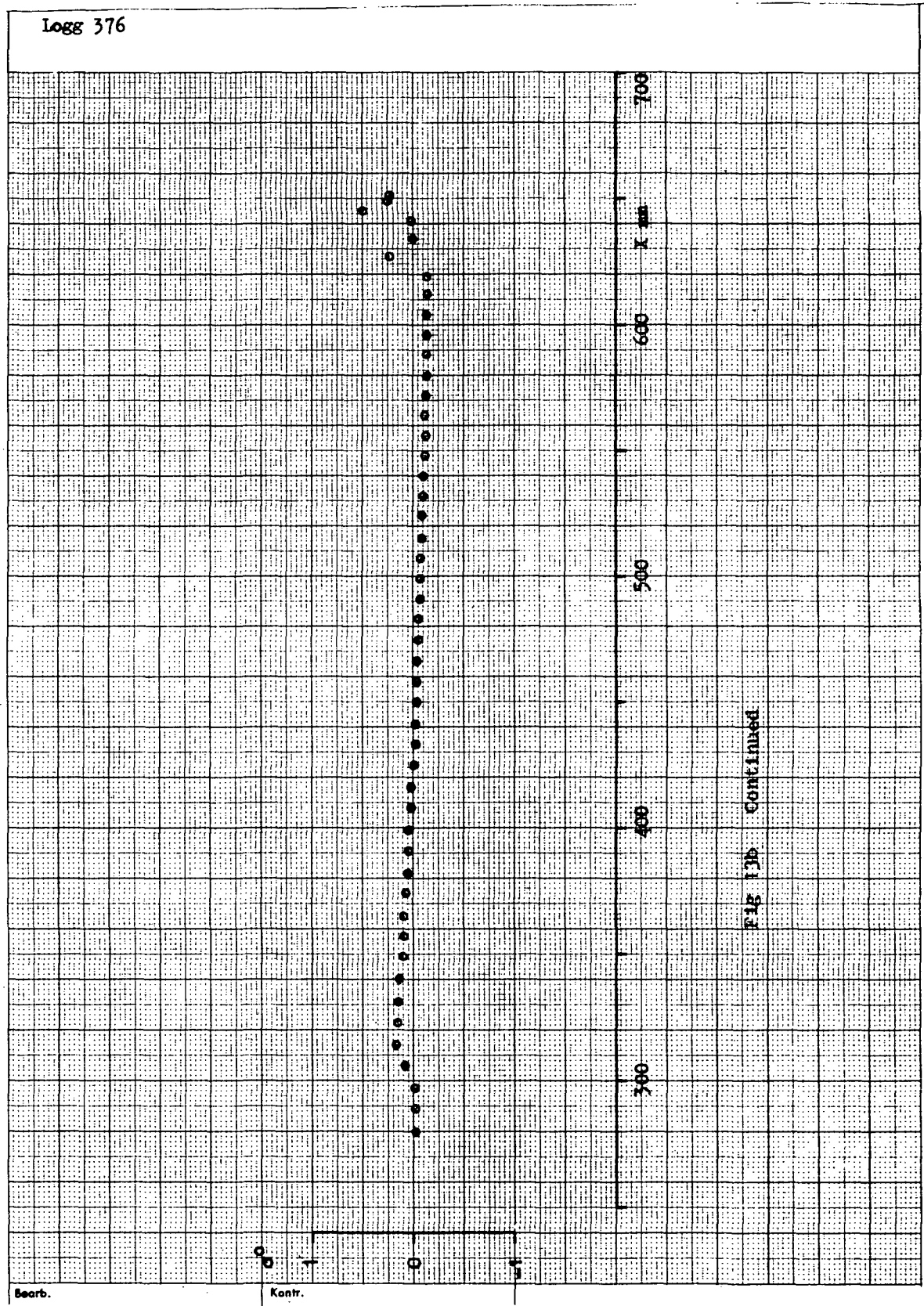
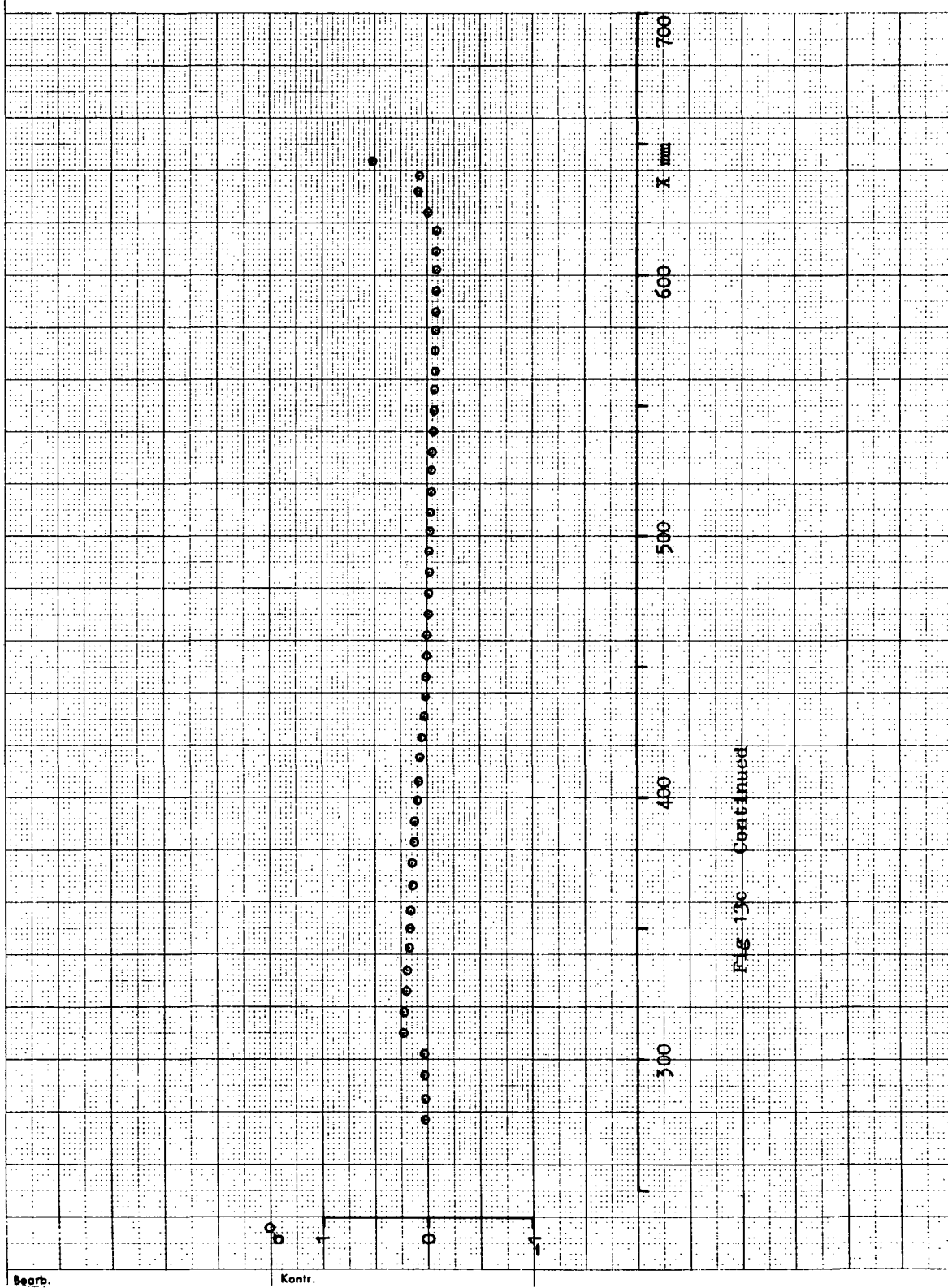


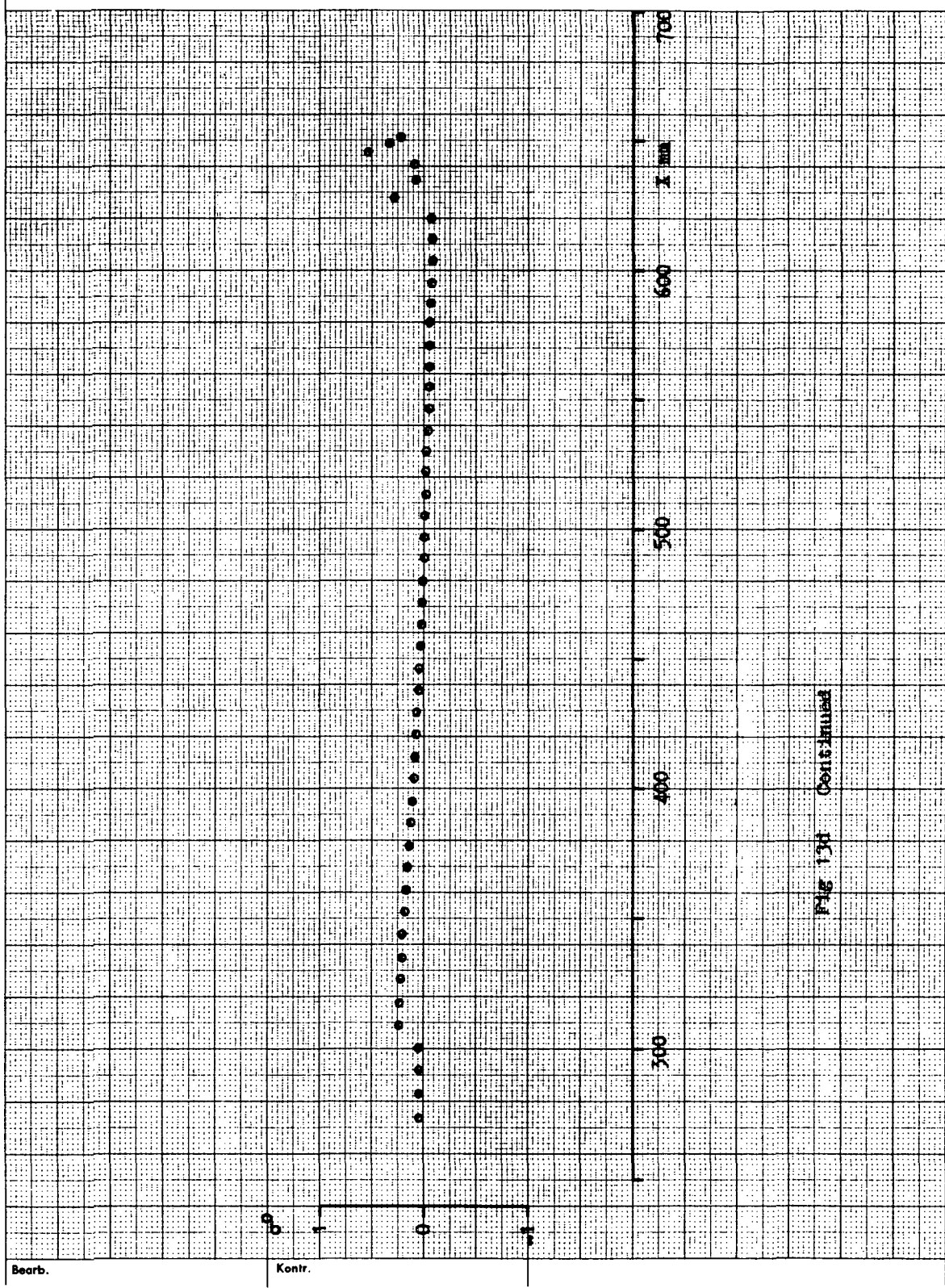
Fig. 3a. Experimental  $\sigma$ -angles as function of distance,  $r/L_0 = 0.375$



Logg 377



Logg 379



Logg 396

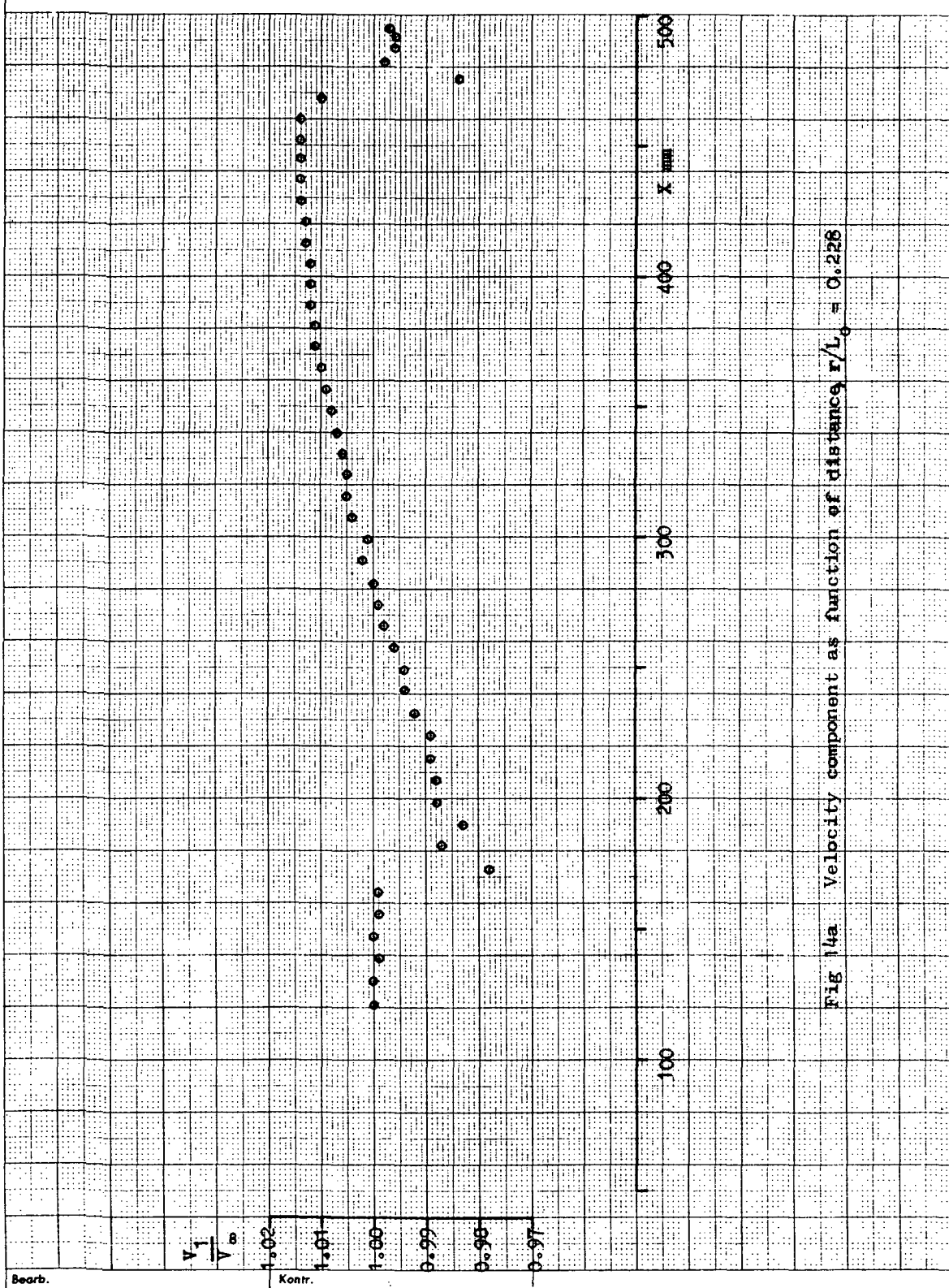
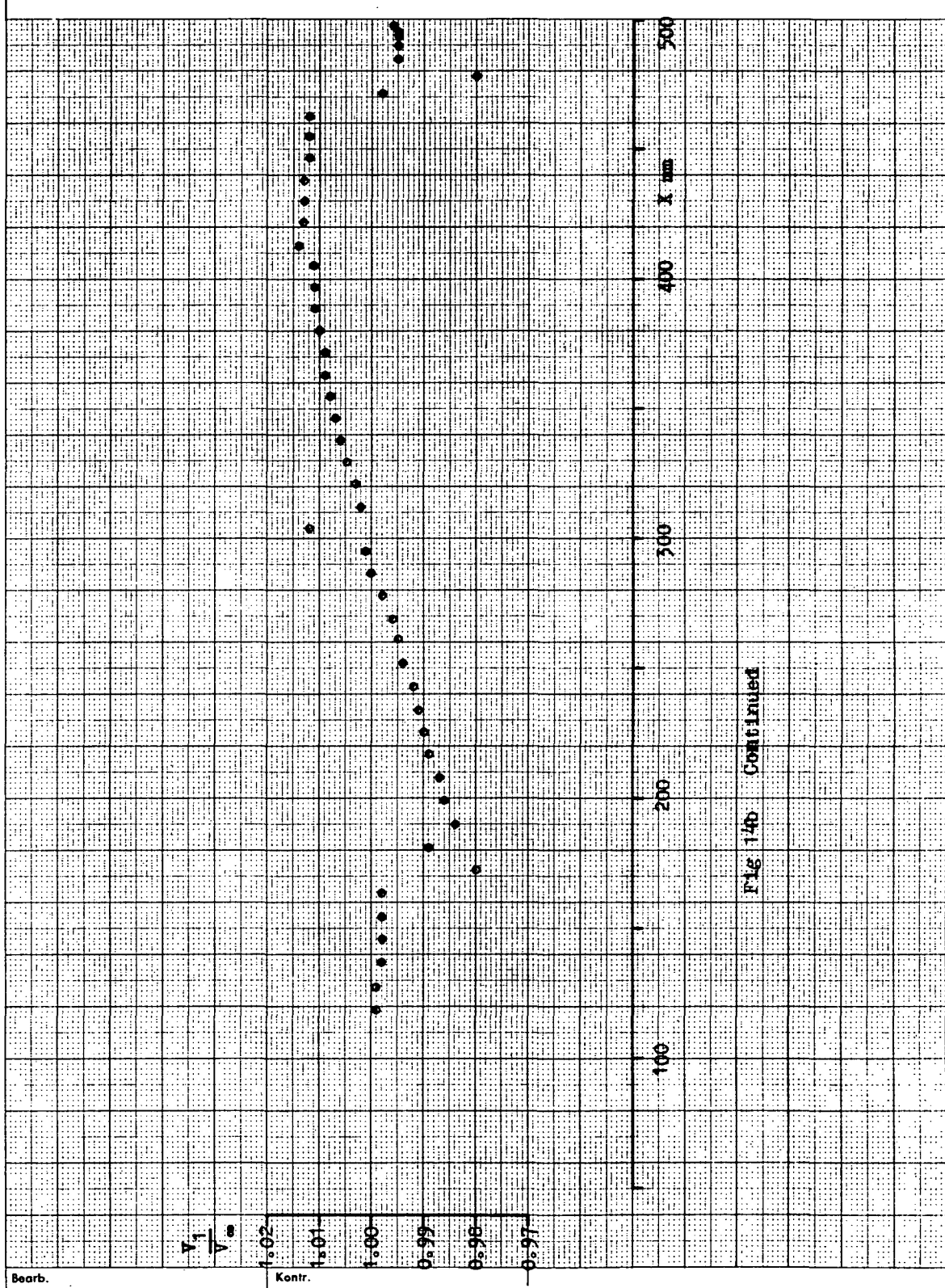
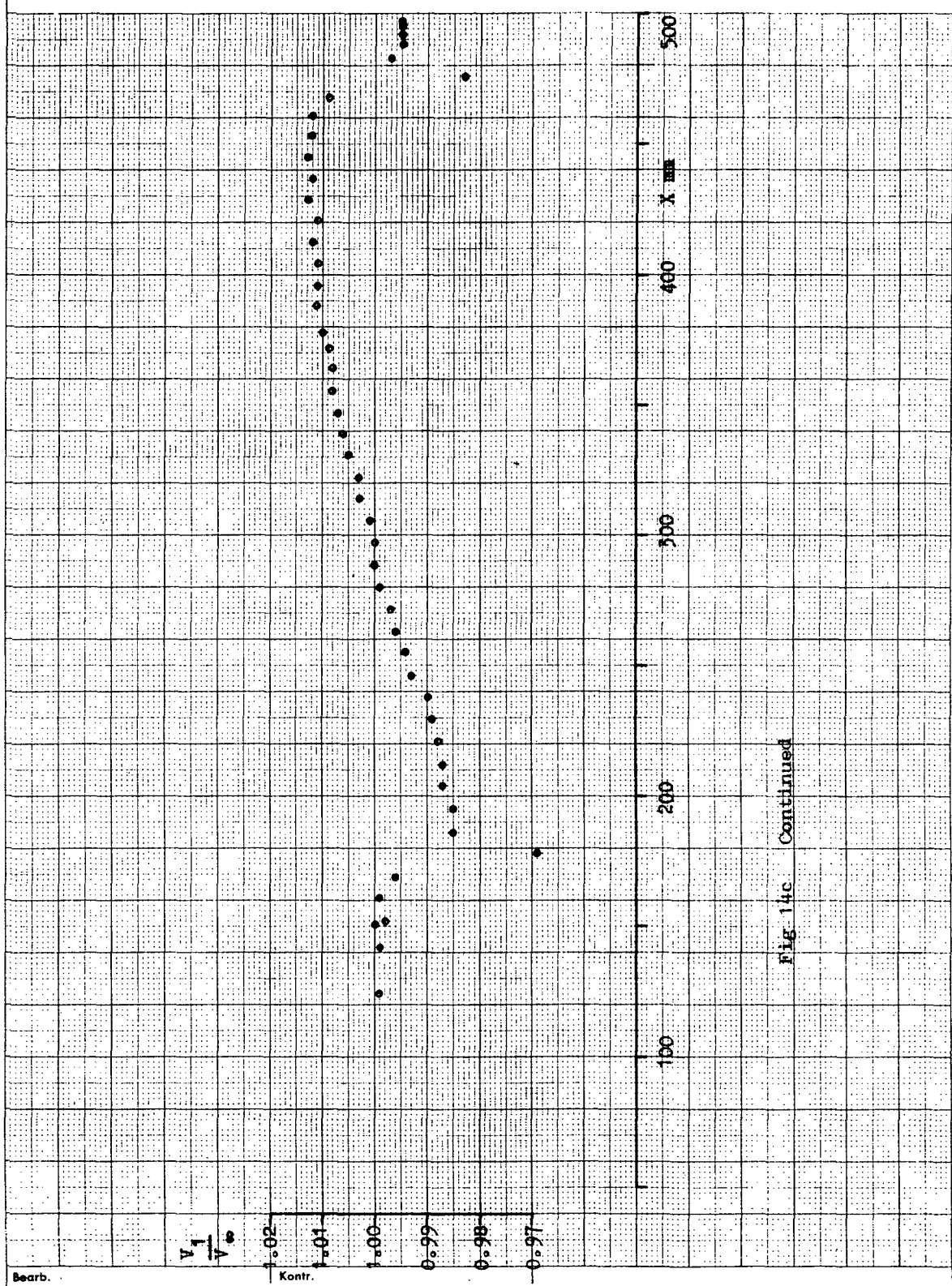


Fig 14a. Velocity component as function of distance,  $r/L_0 = 0.226$

Logg 397



Logg 398



Logg 396

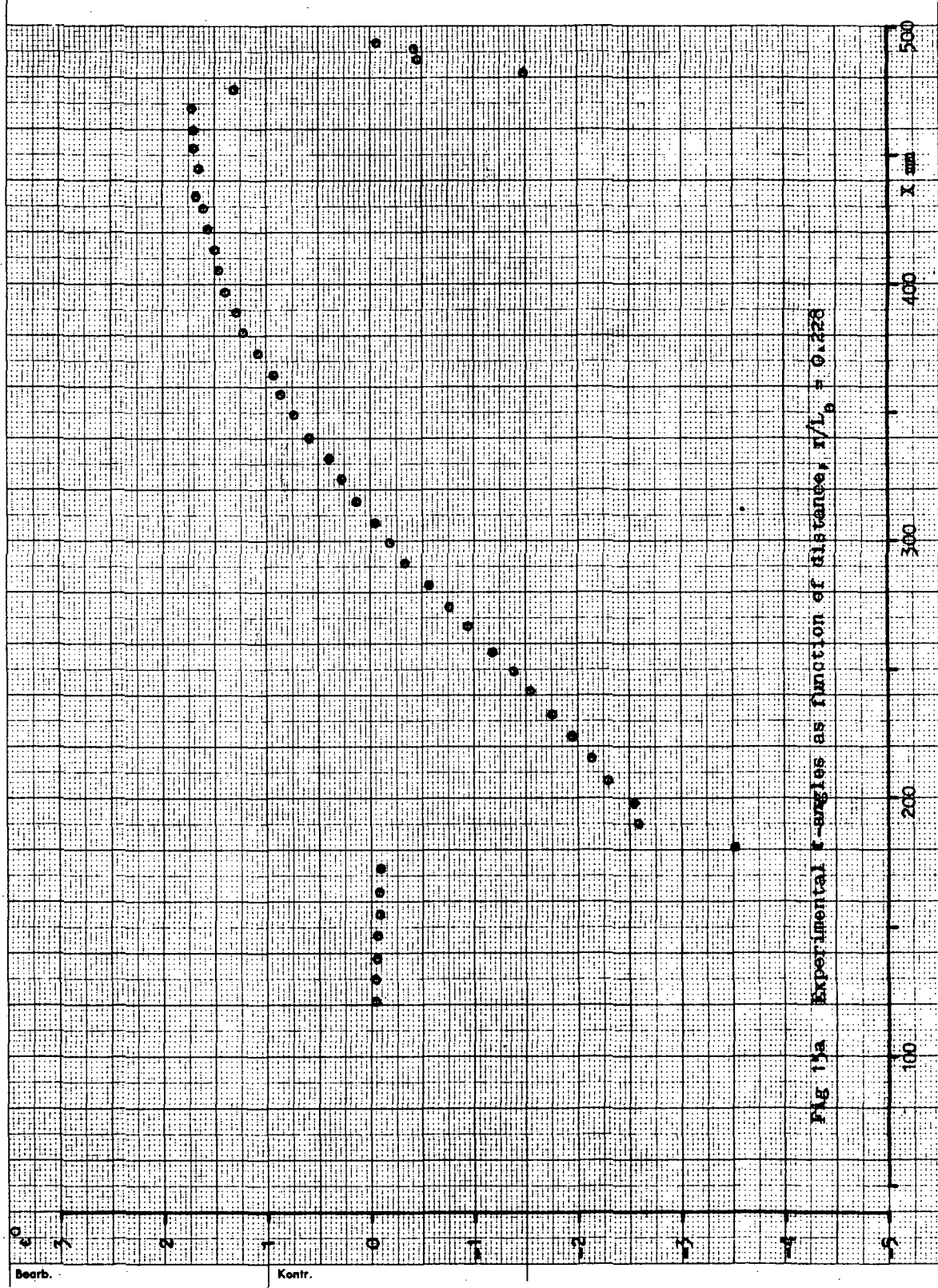
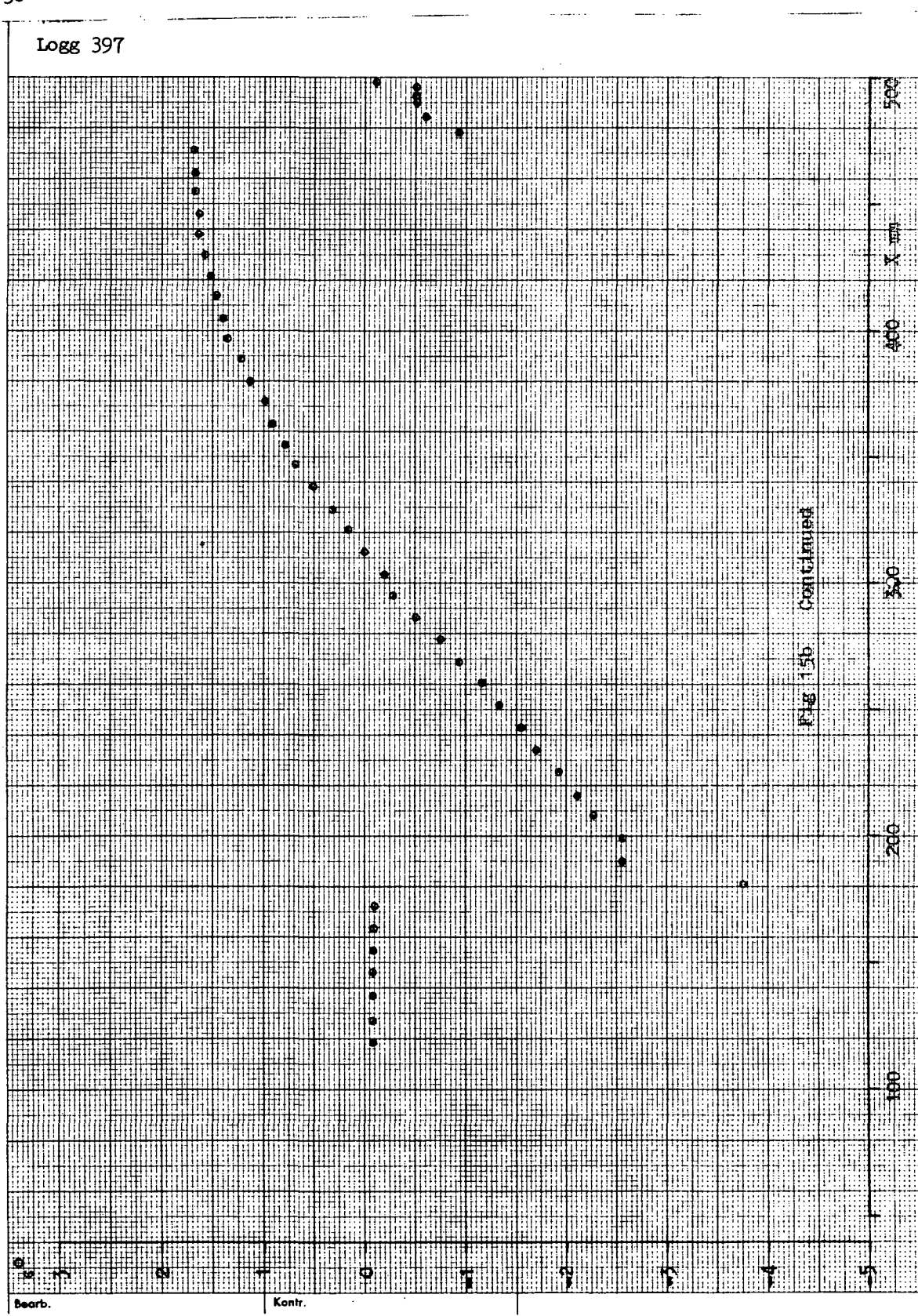
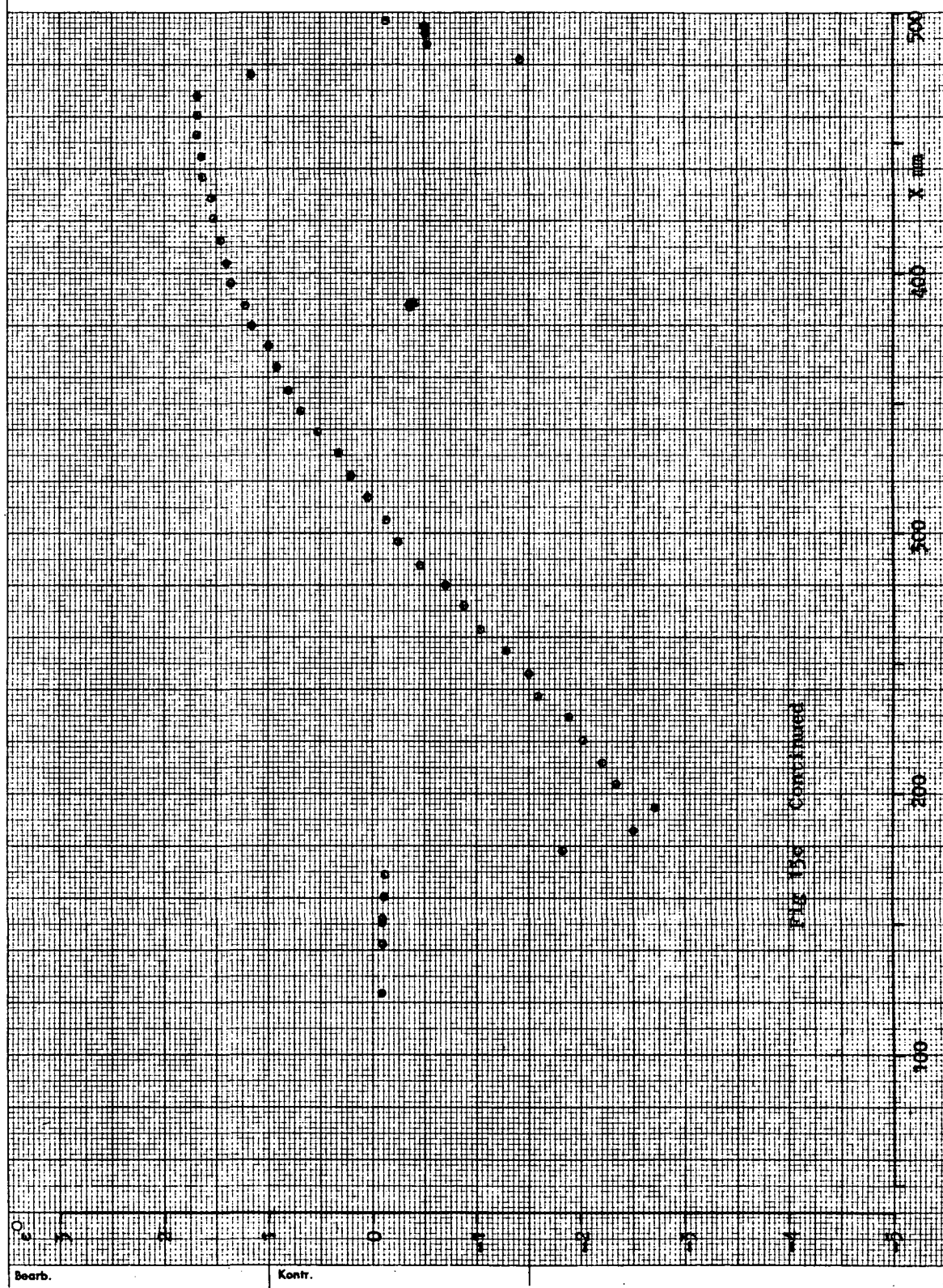


Fig. 13a. Reproductive samples as function of life-table stage.



Logg 398



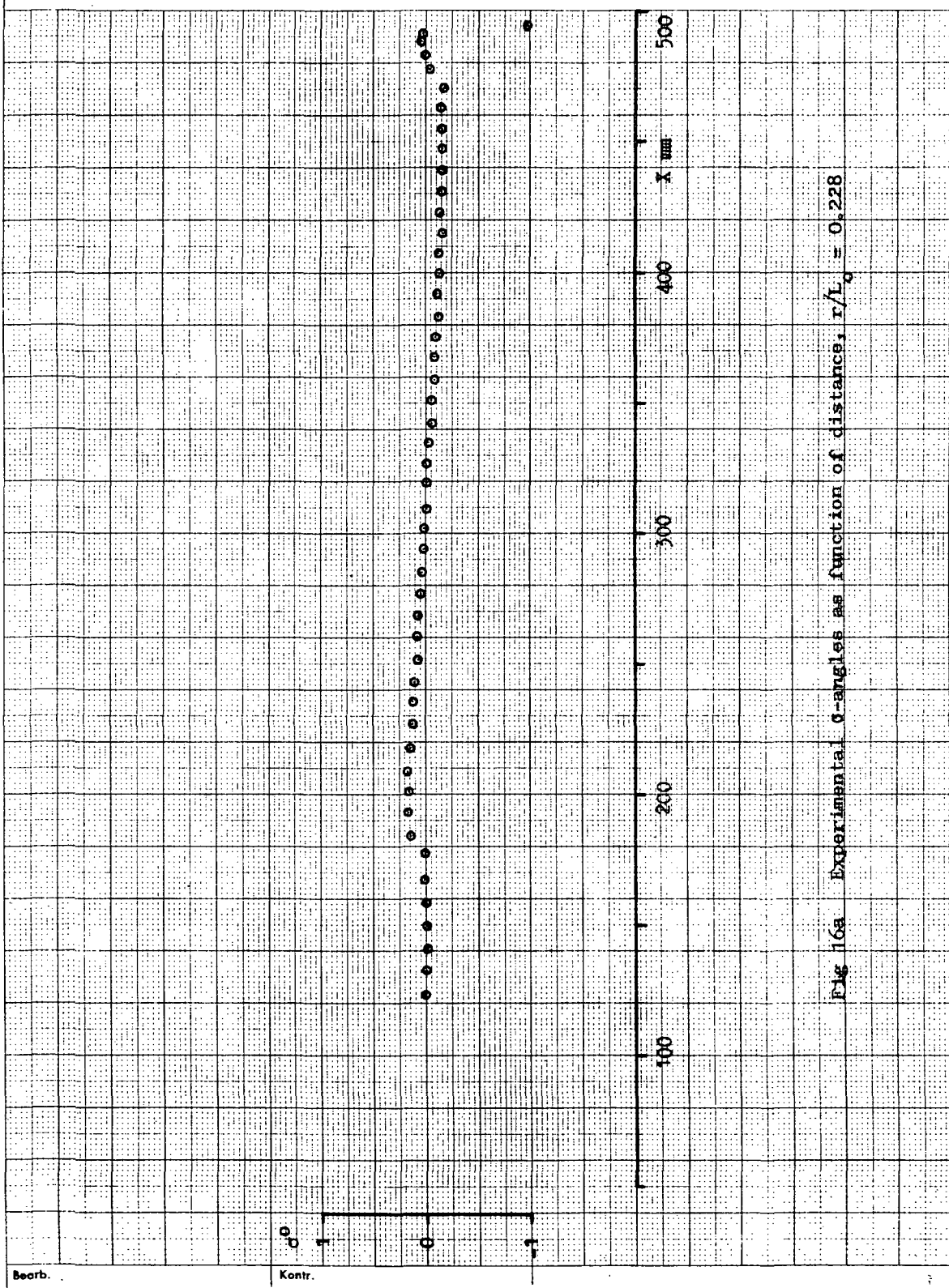
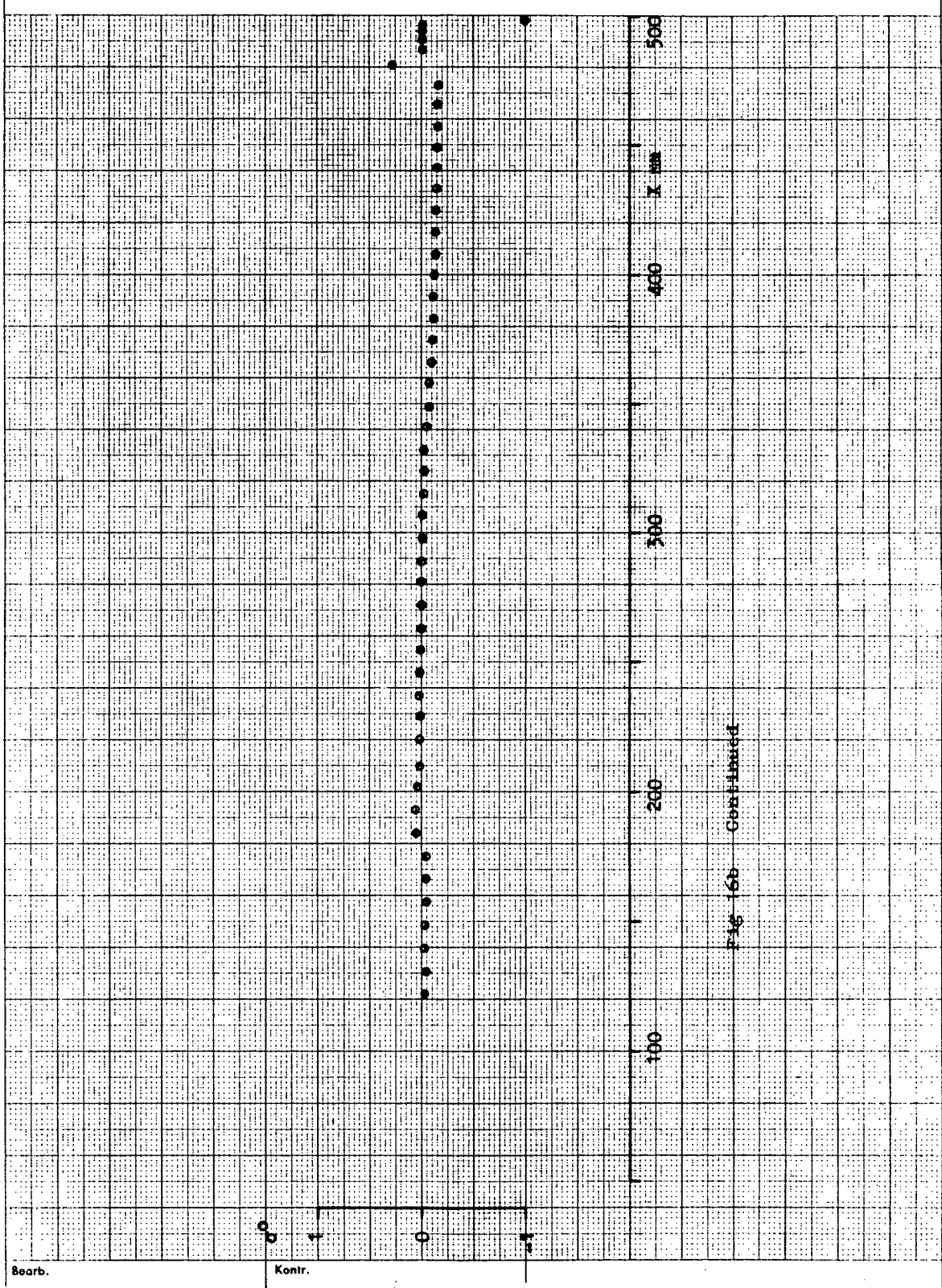
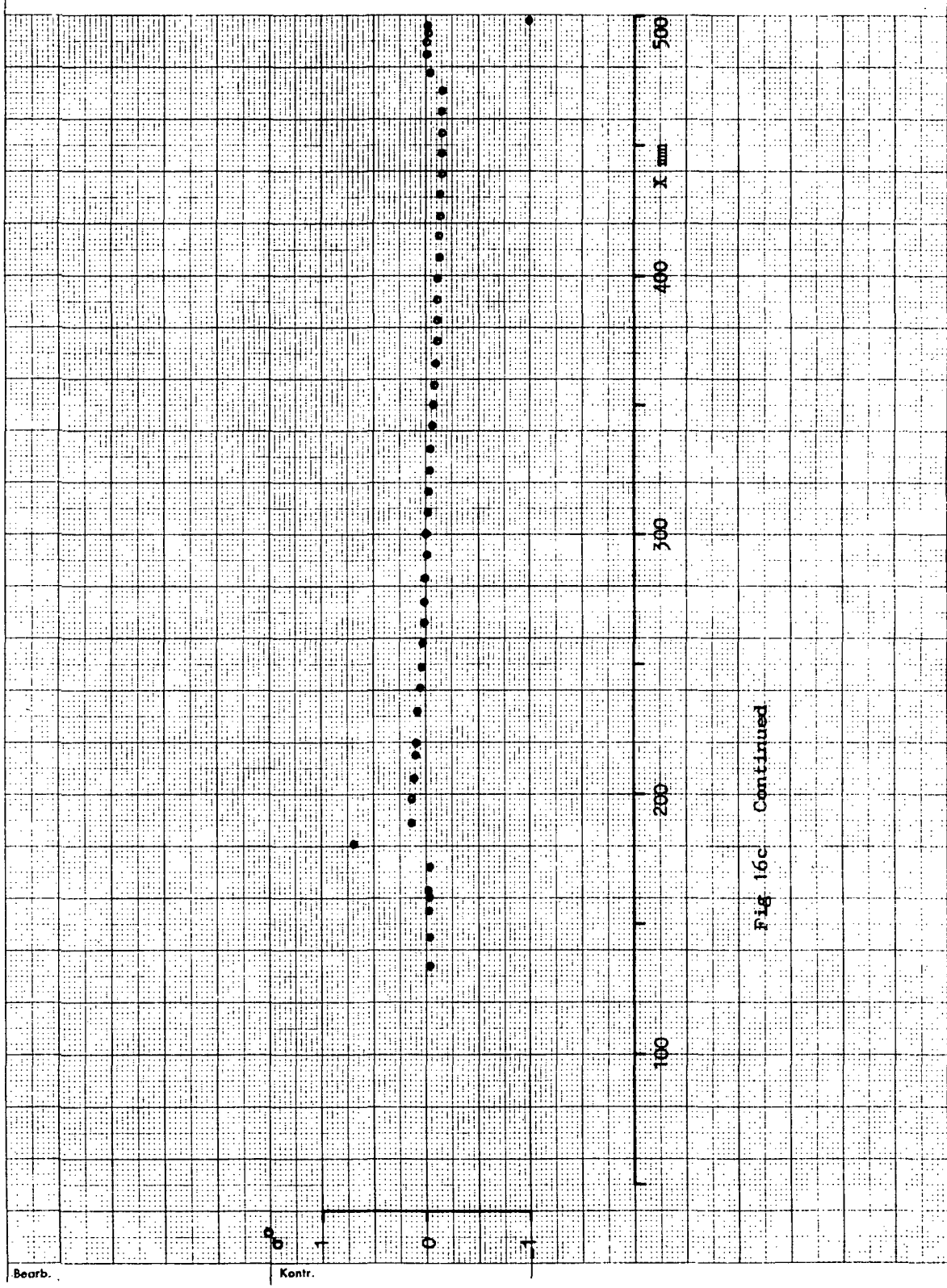


Fig. 16a. Experimental g-angles as function of distance,  $r/l_0 \pm 0.228$ .

Logg 397





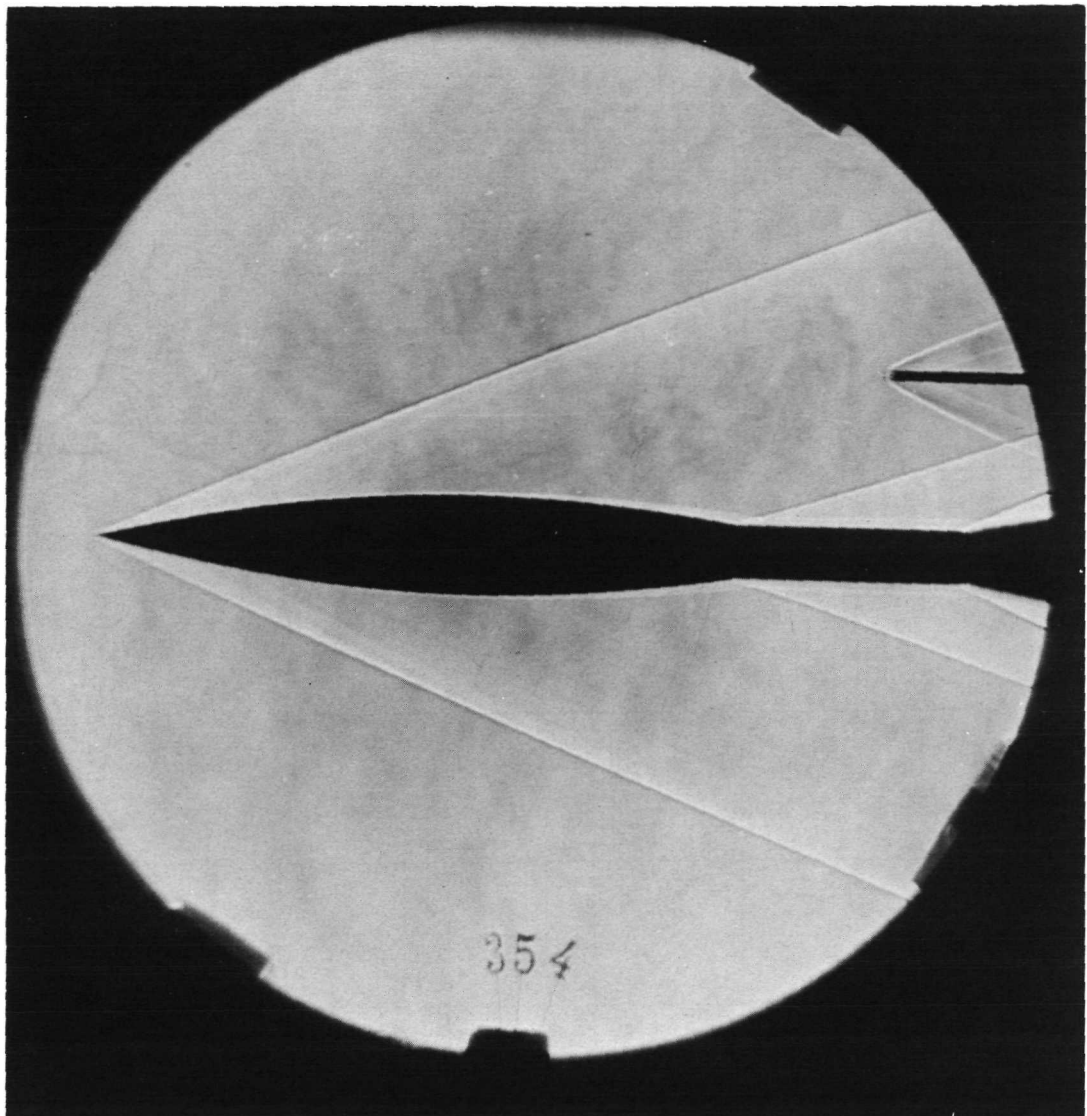


Fig. 17 Schlierenphotograph of model and probe

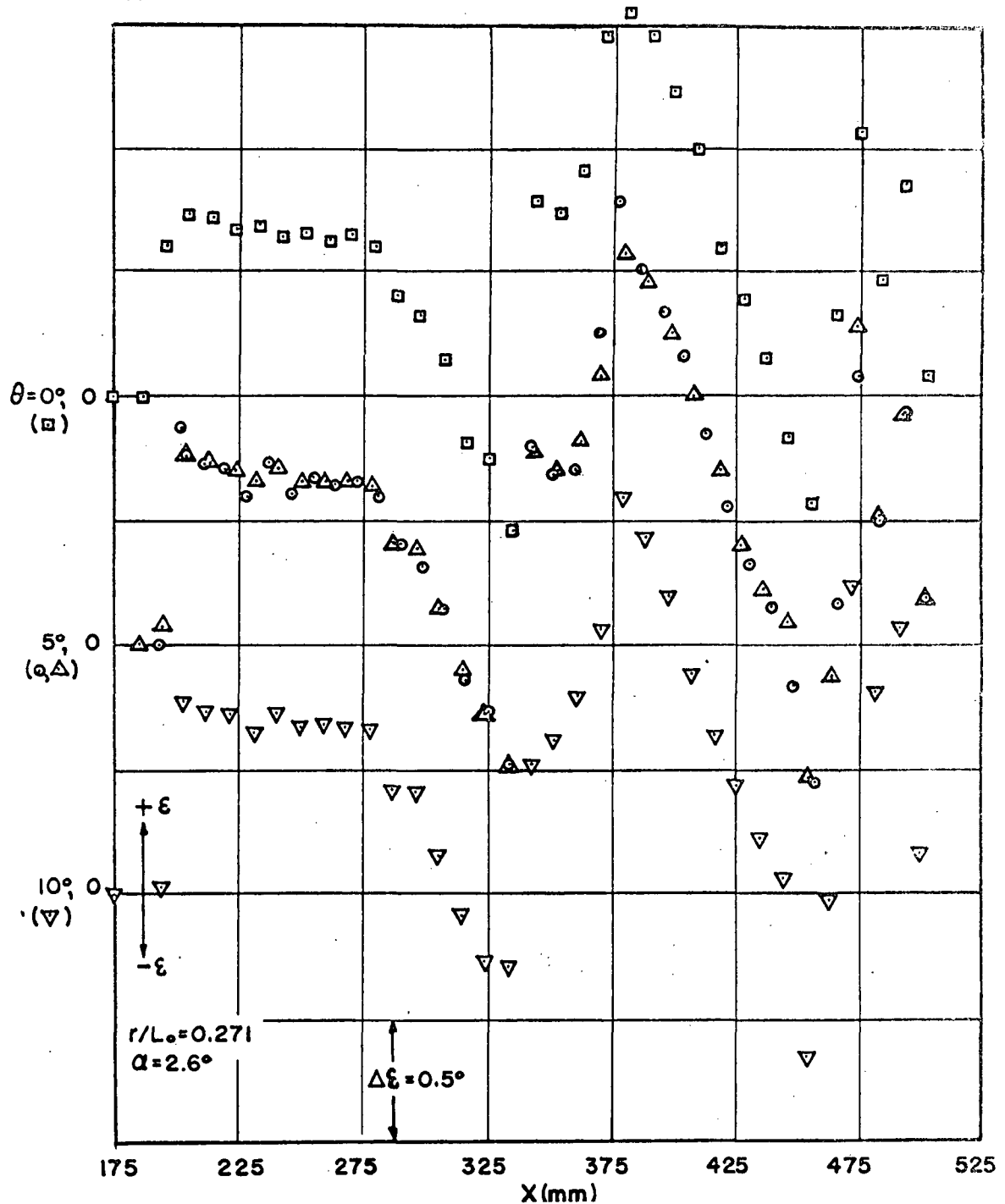


Fig 18 a Experimental values of  $\epsilon$  as function of distance at several meridian planes

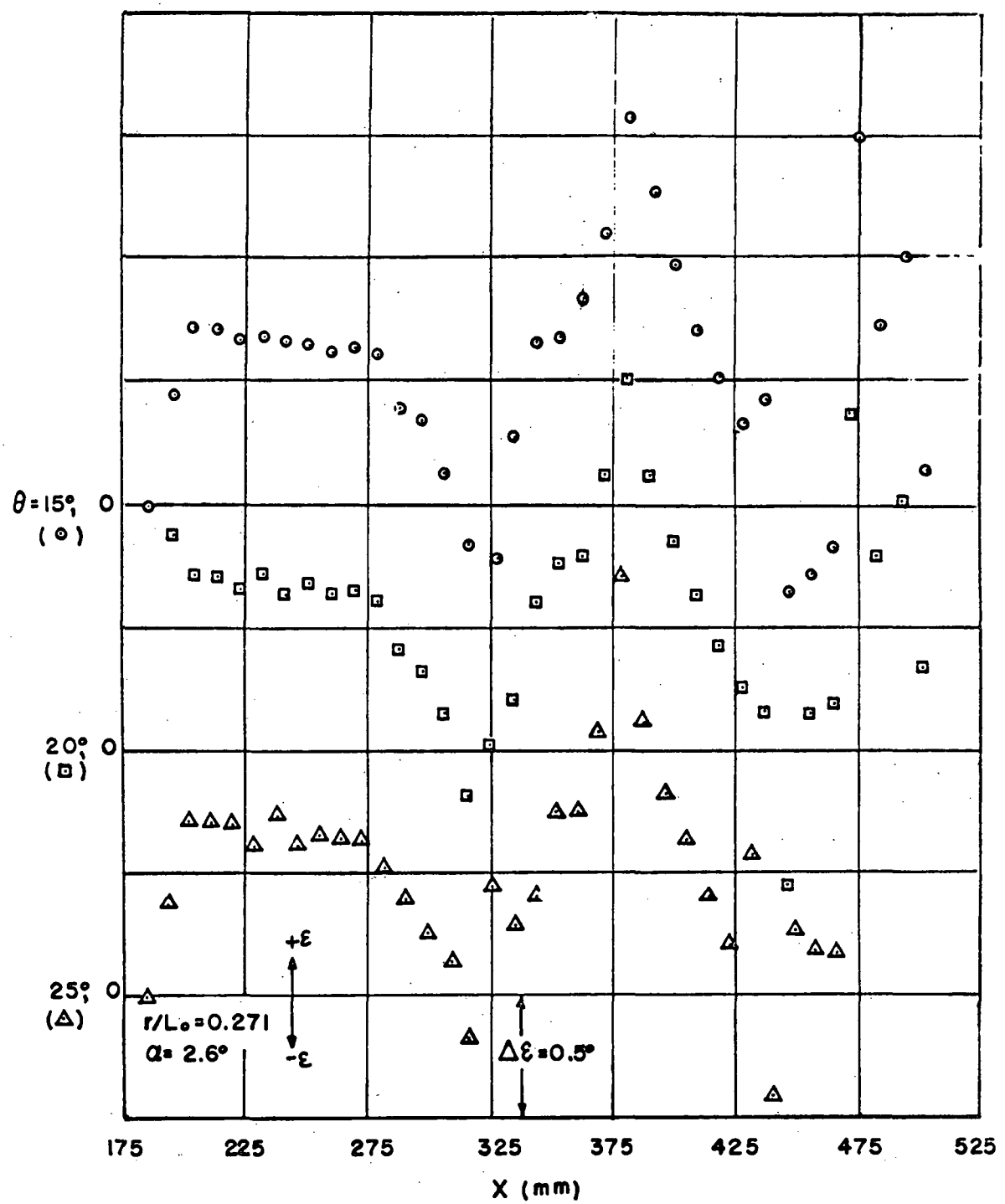


Fig 18 b Continued

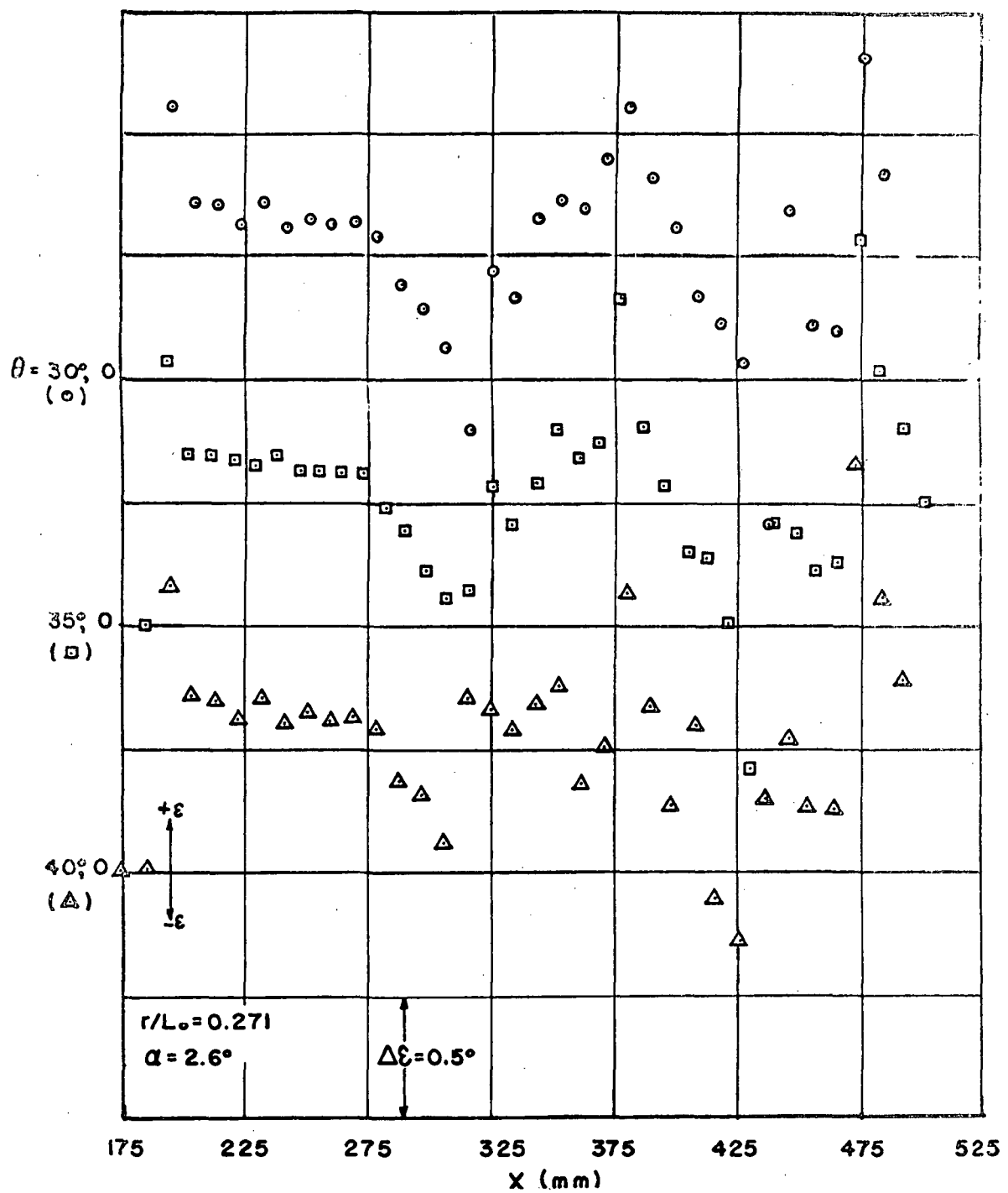


Fig 18 c Continued

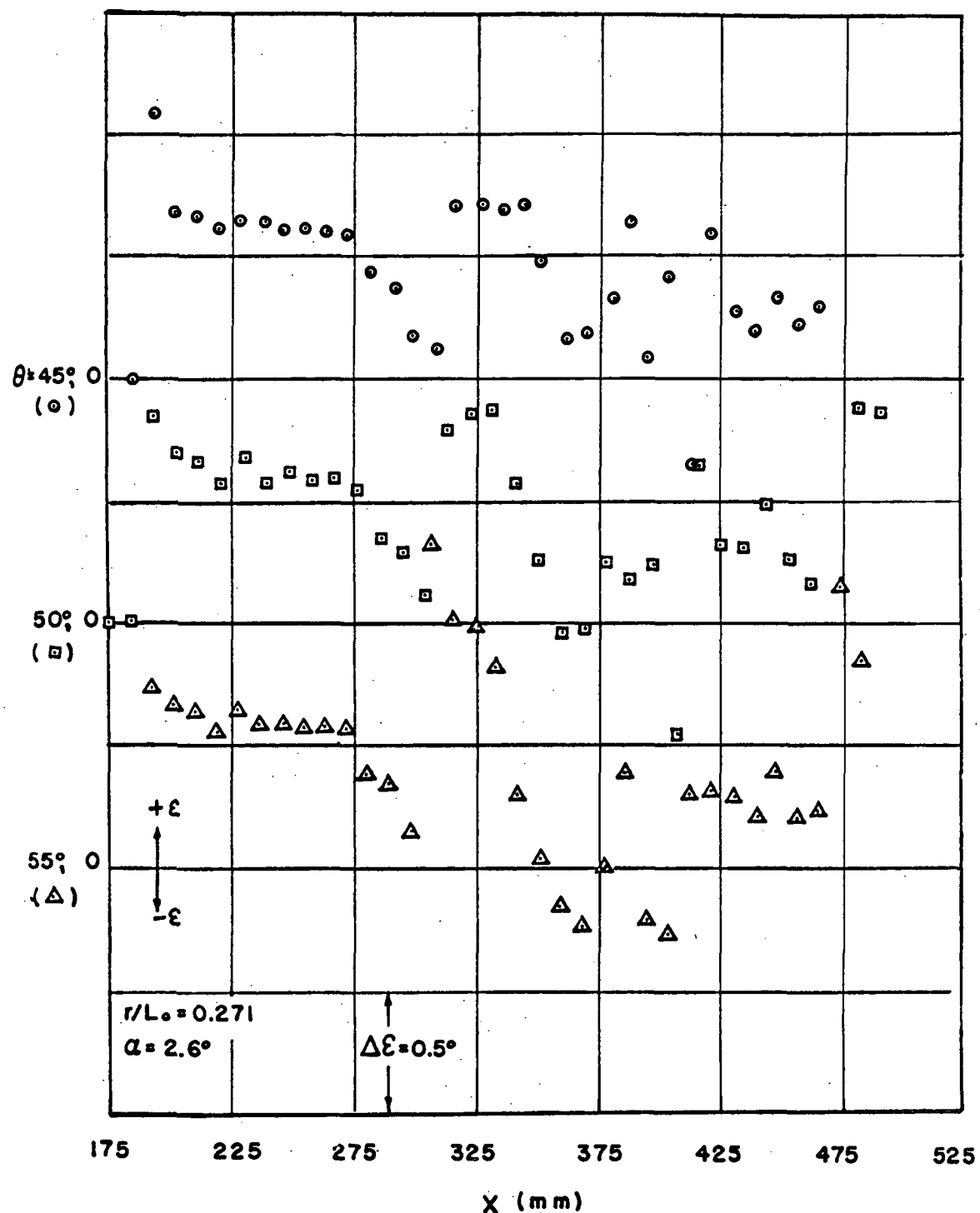


Fig 18 d Continued

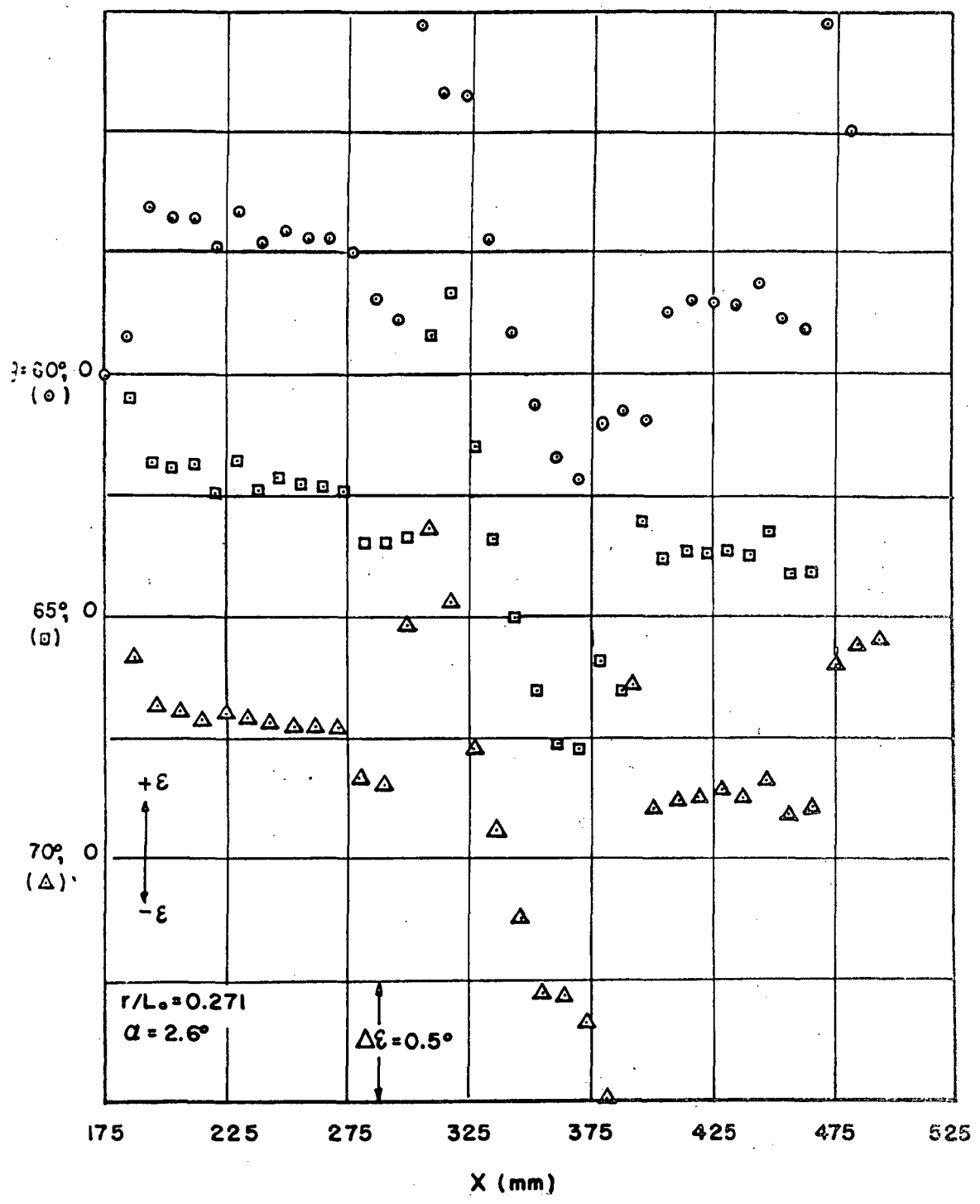
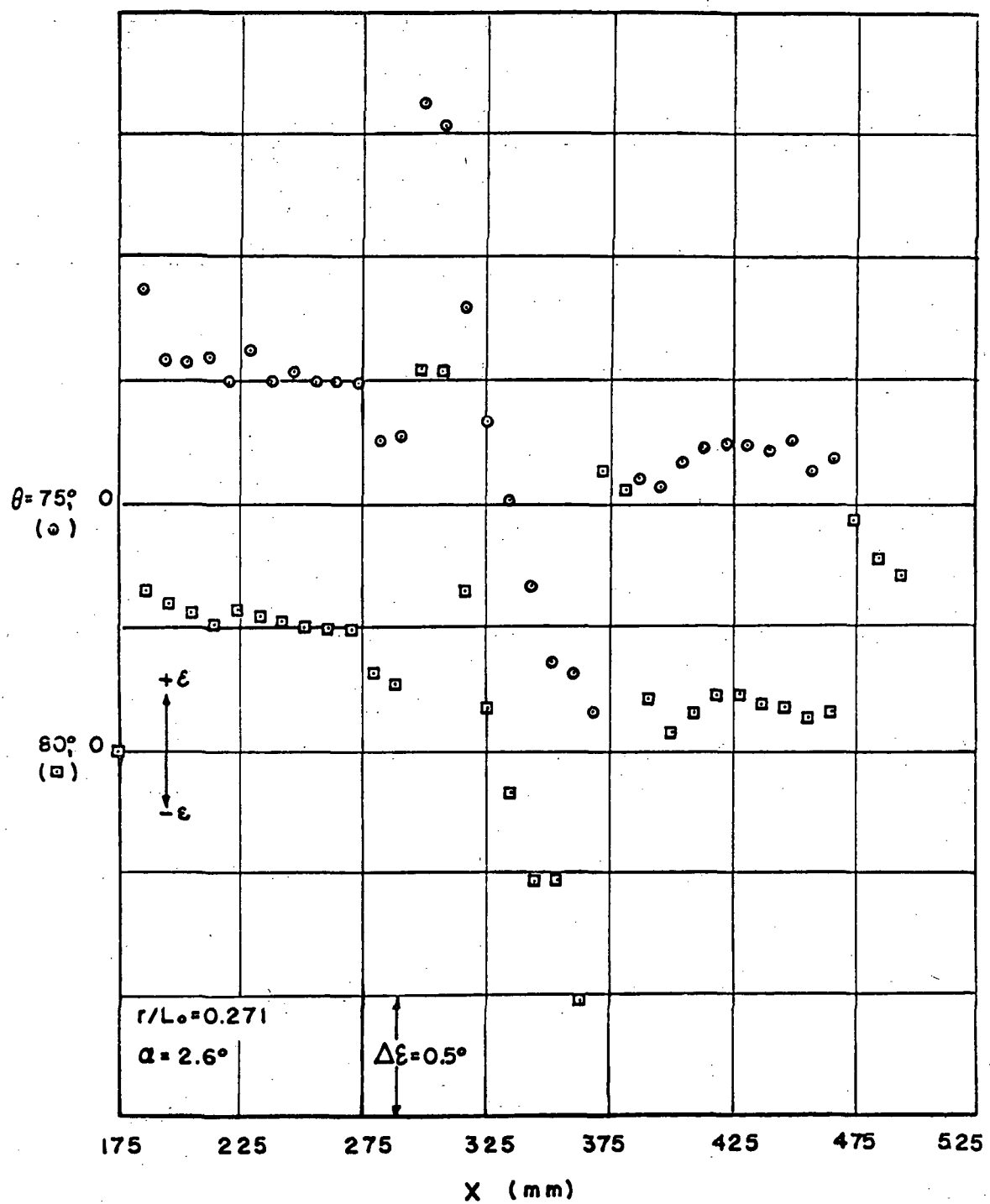


Fig 18e Continued



**Fig 18f** Continued

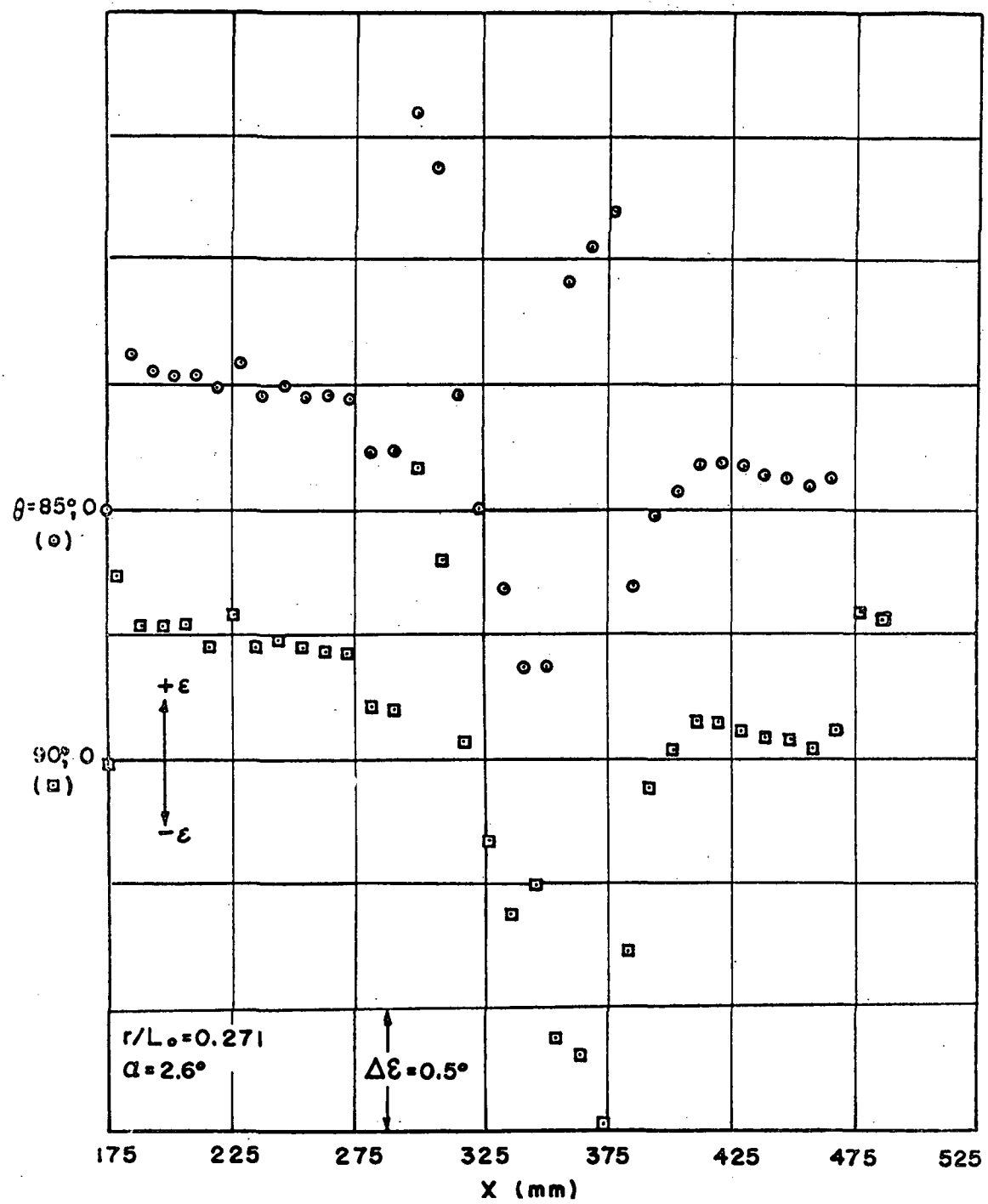


Fig 18g Continued

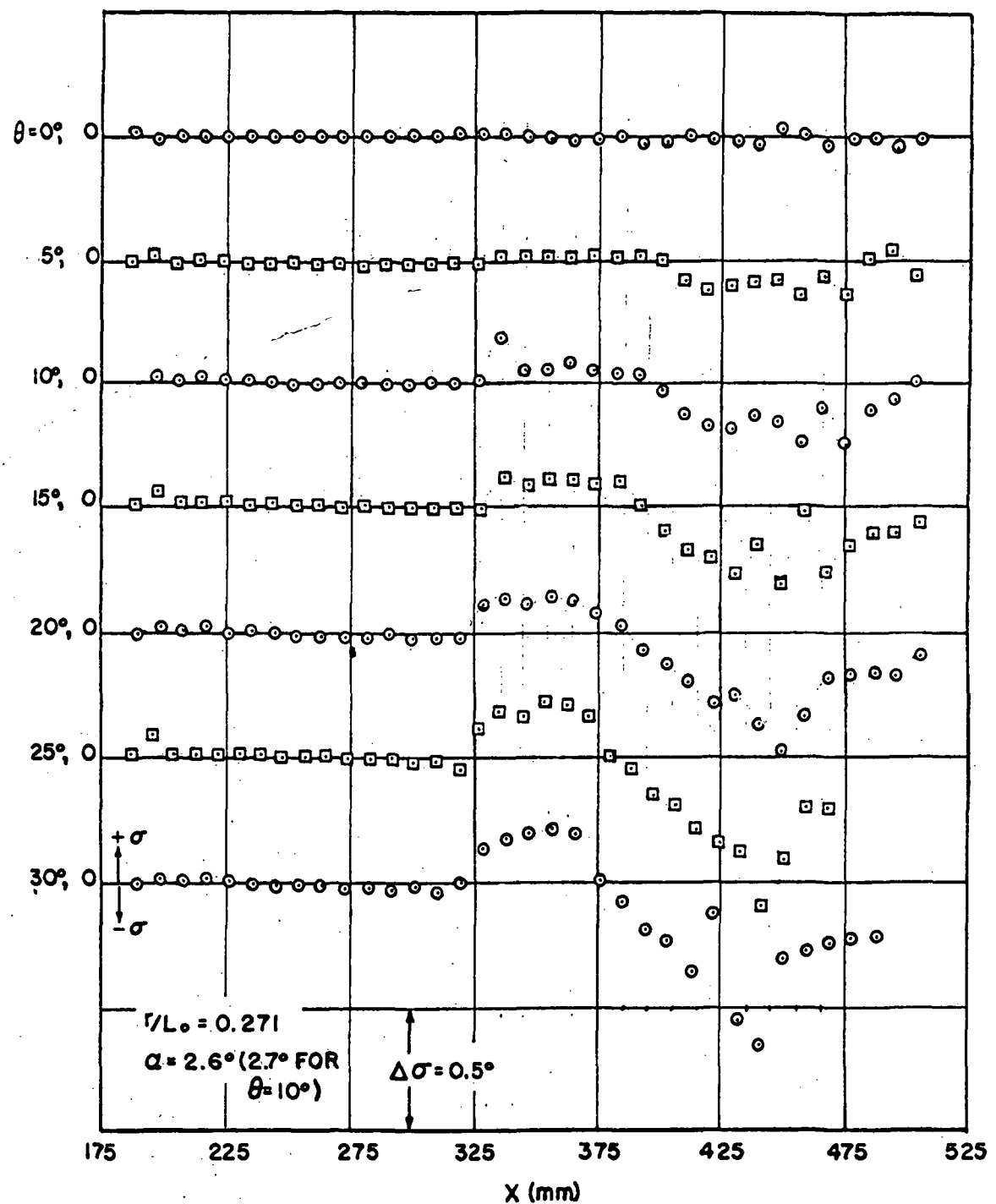


Fig 19a Experimental values of  $\sigma$  as function of distance  
at several meridian planes

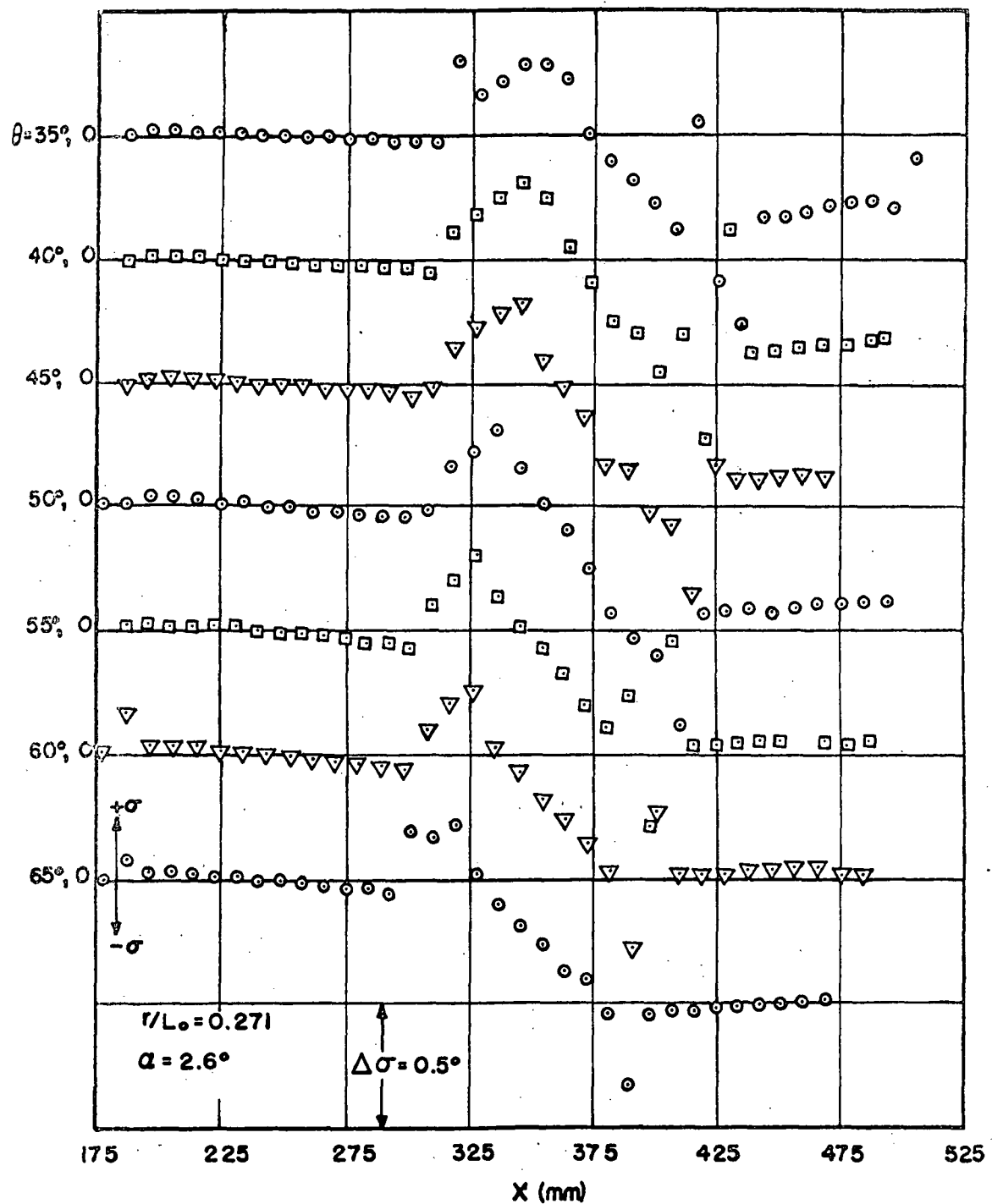


Fig 19b Continued

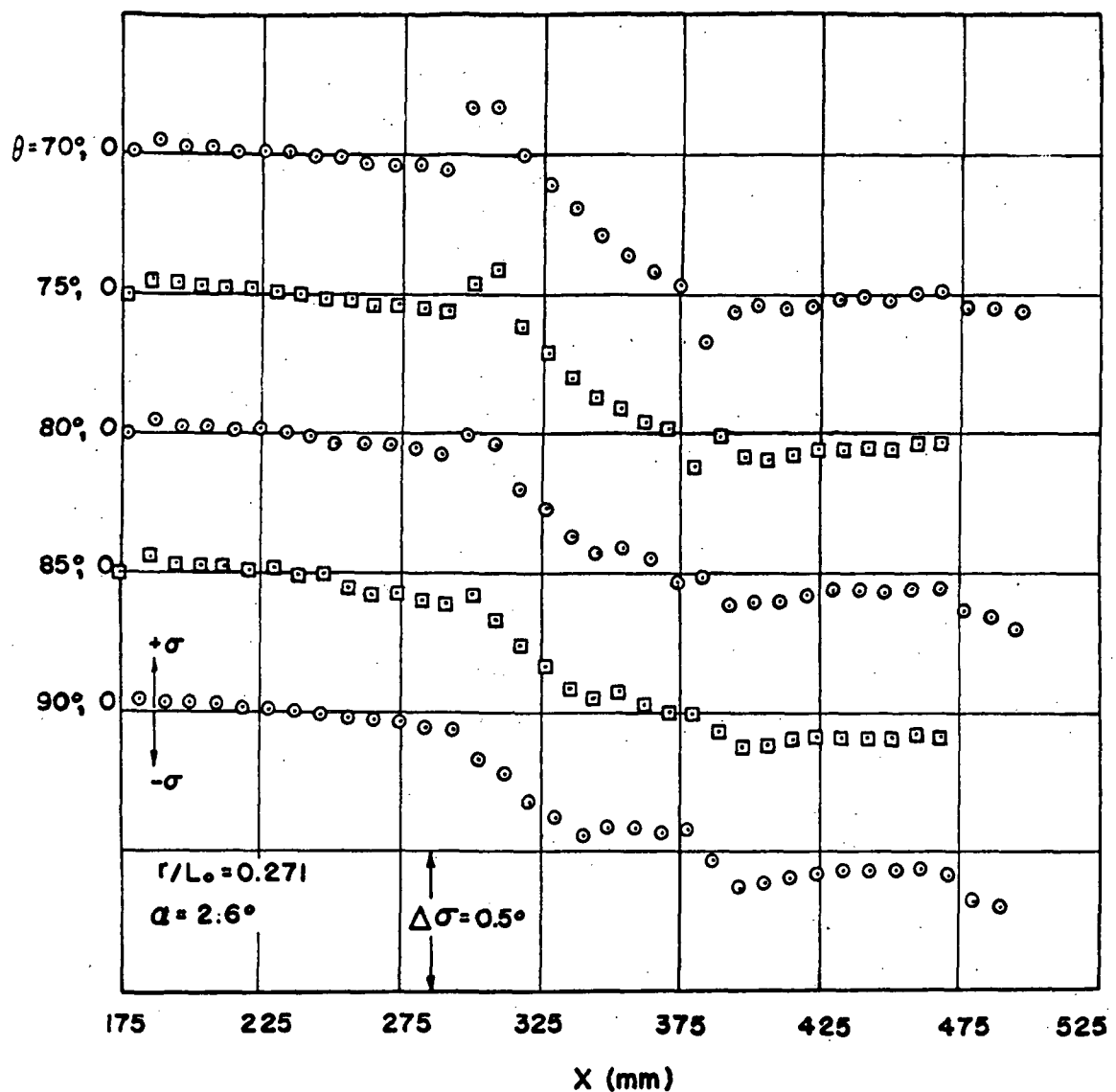


Fig 19c Continued

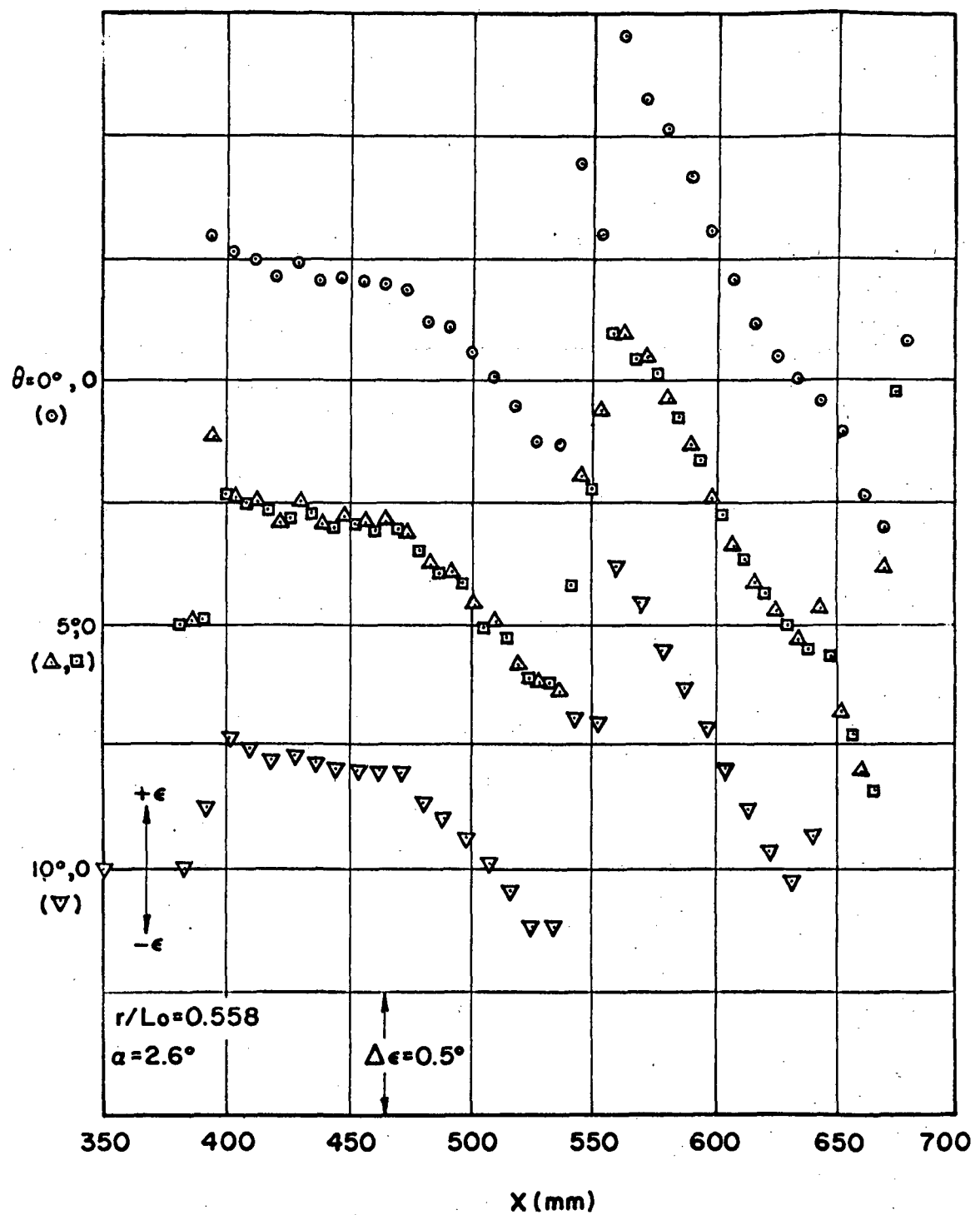


Fig 20a Experimental values of  $\epsilon$  as function of distance at several meridian planes

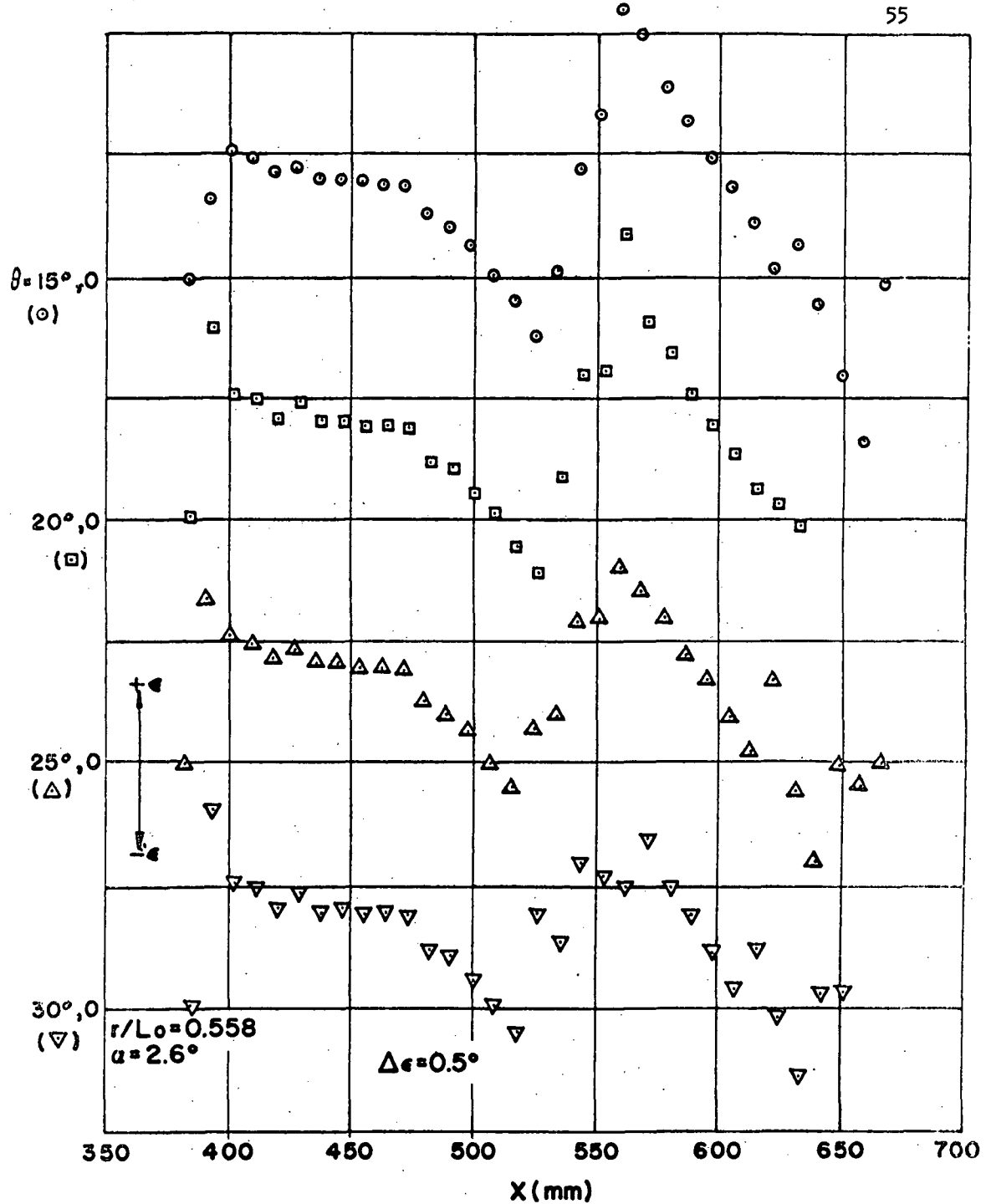


Fig 20b Continued

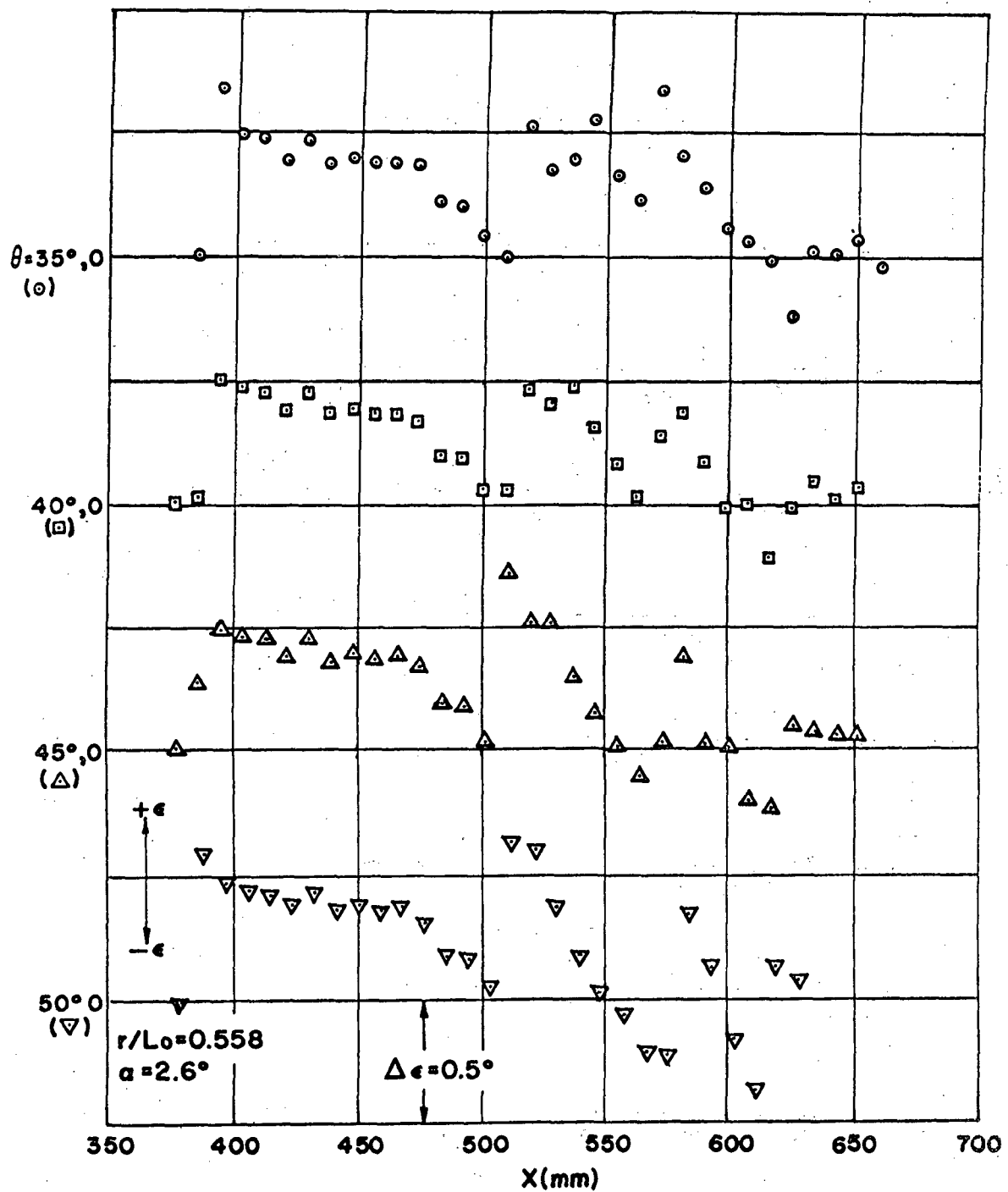


Fig 20c Continued

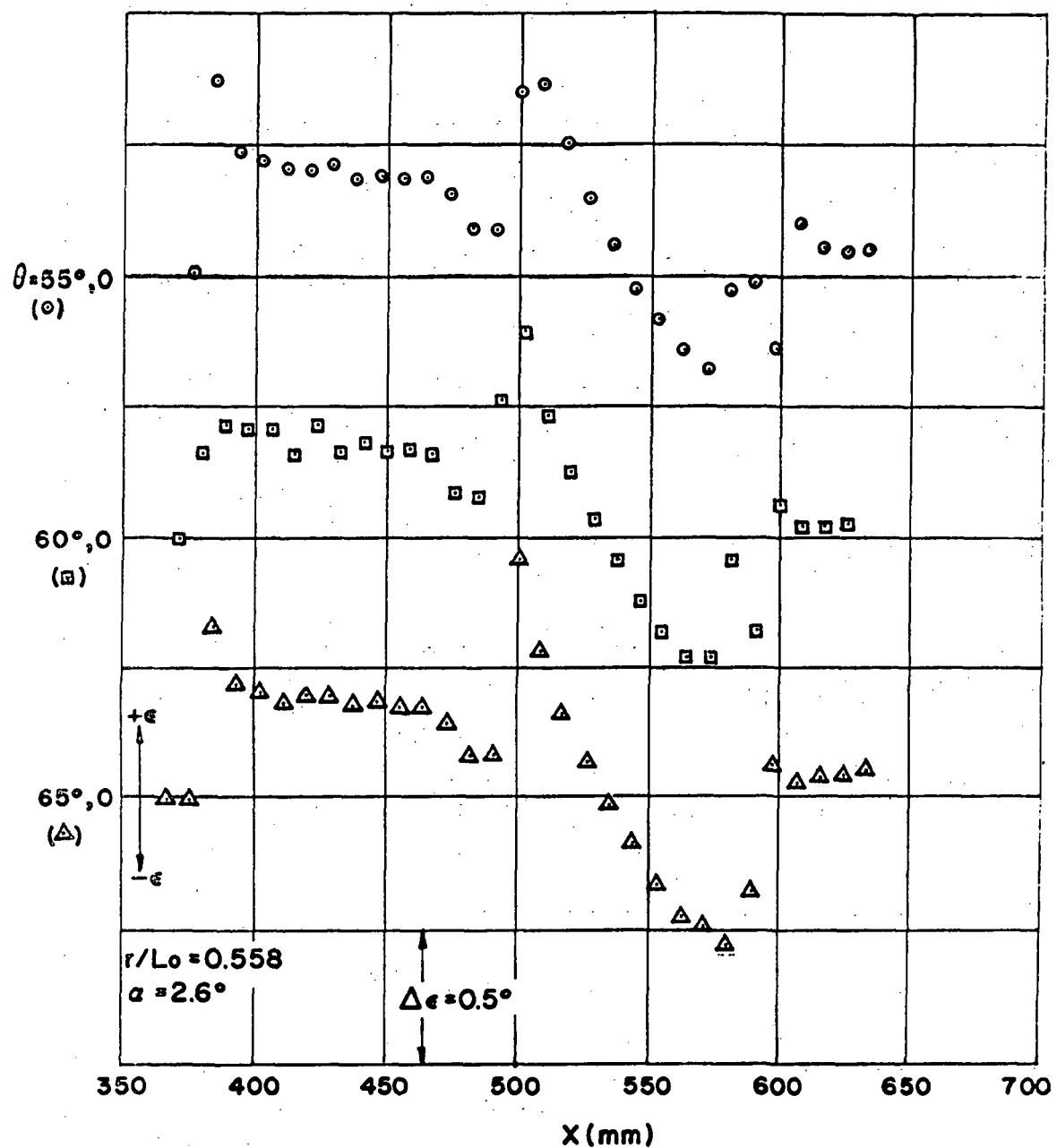


Fig 20d Continued.

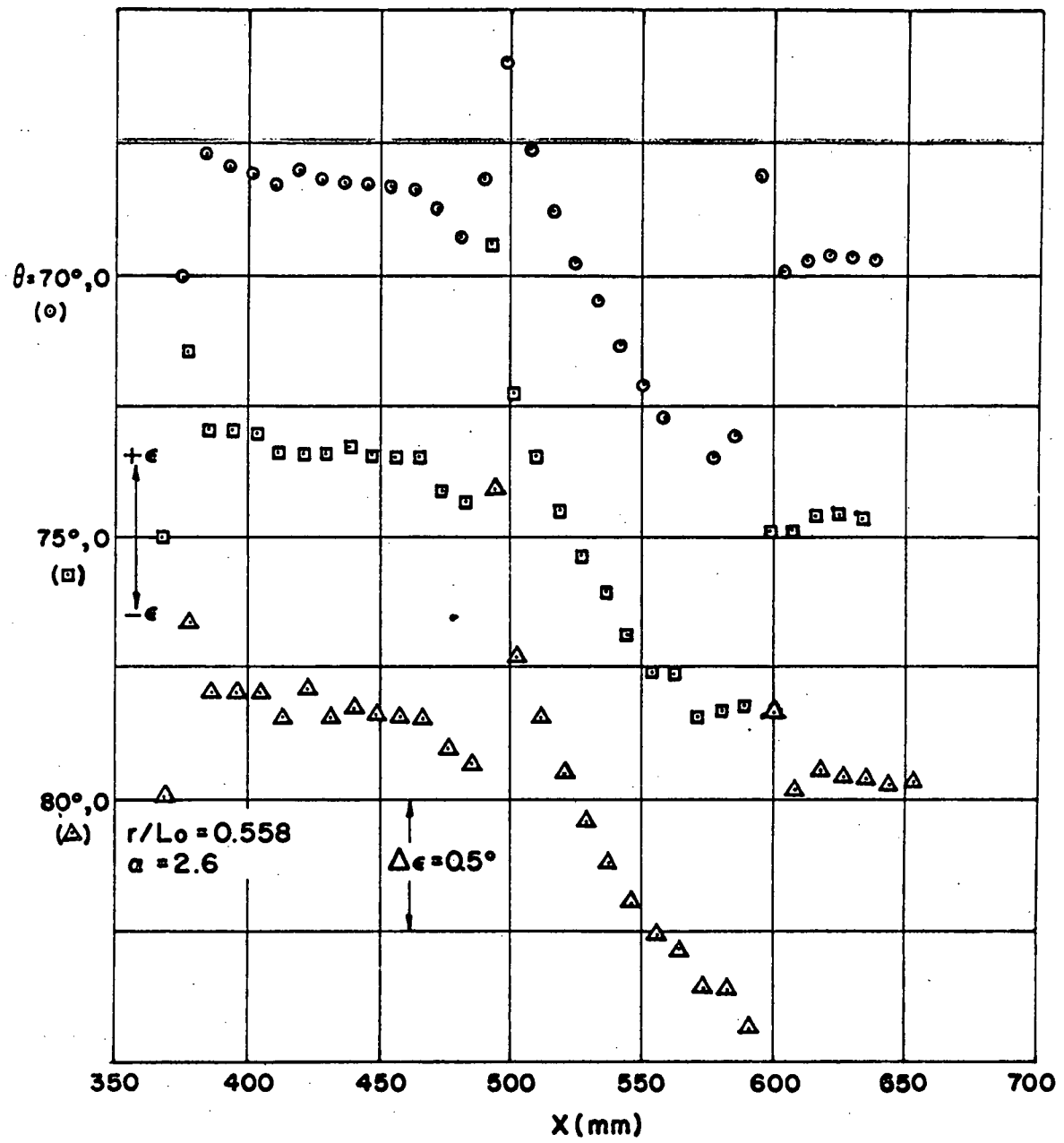


Fig 20e Continued

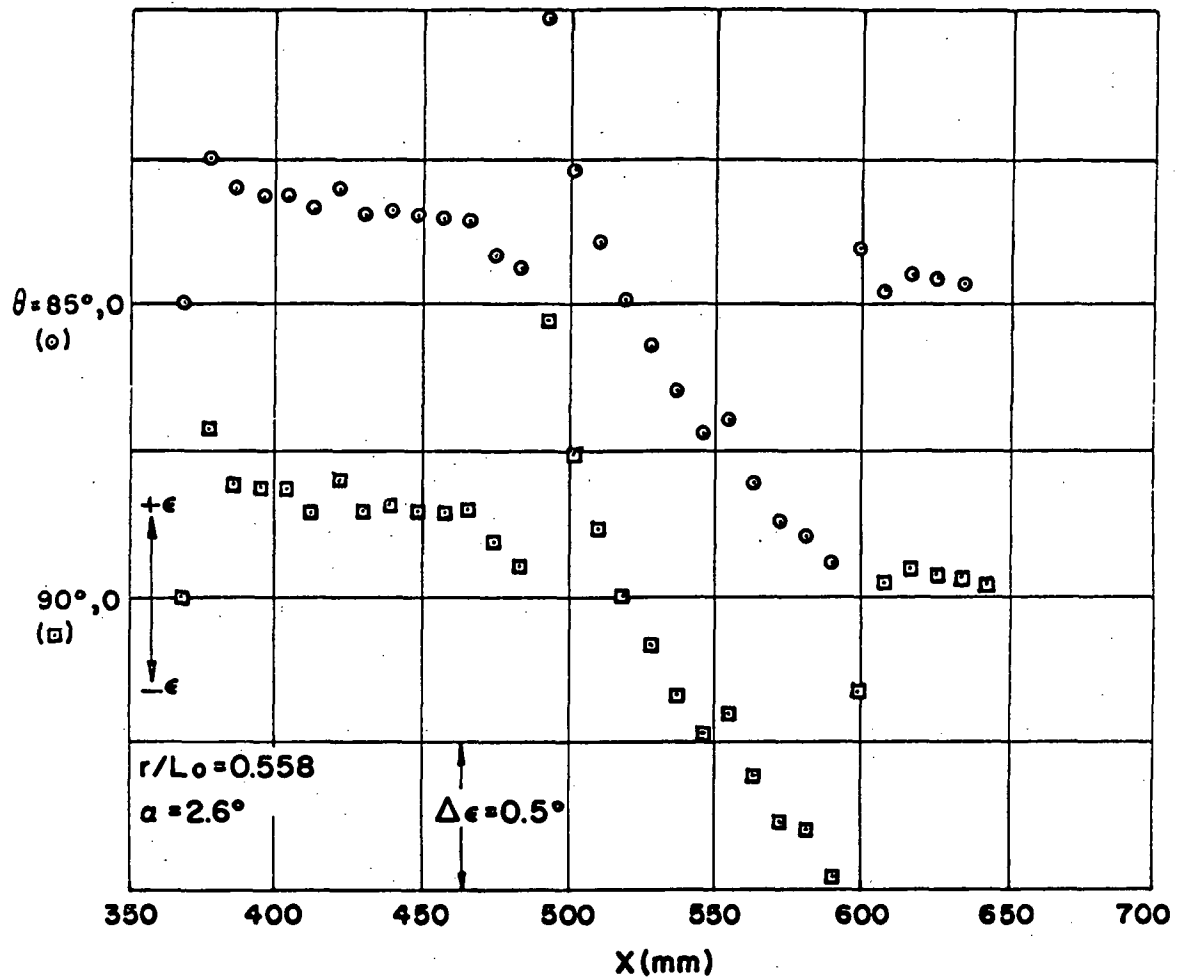


Fig 2Of Continued

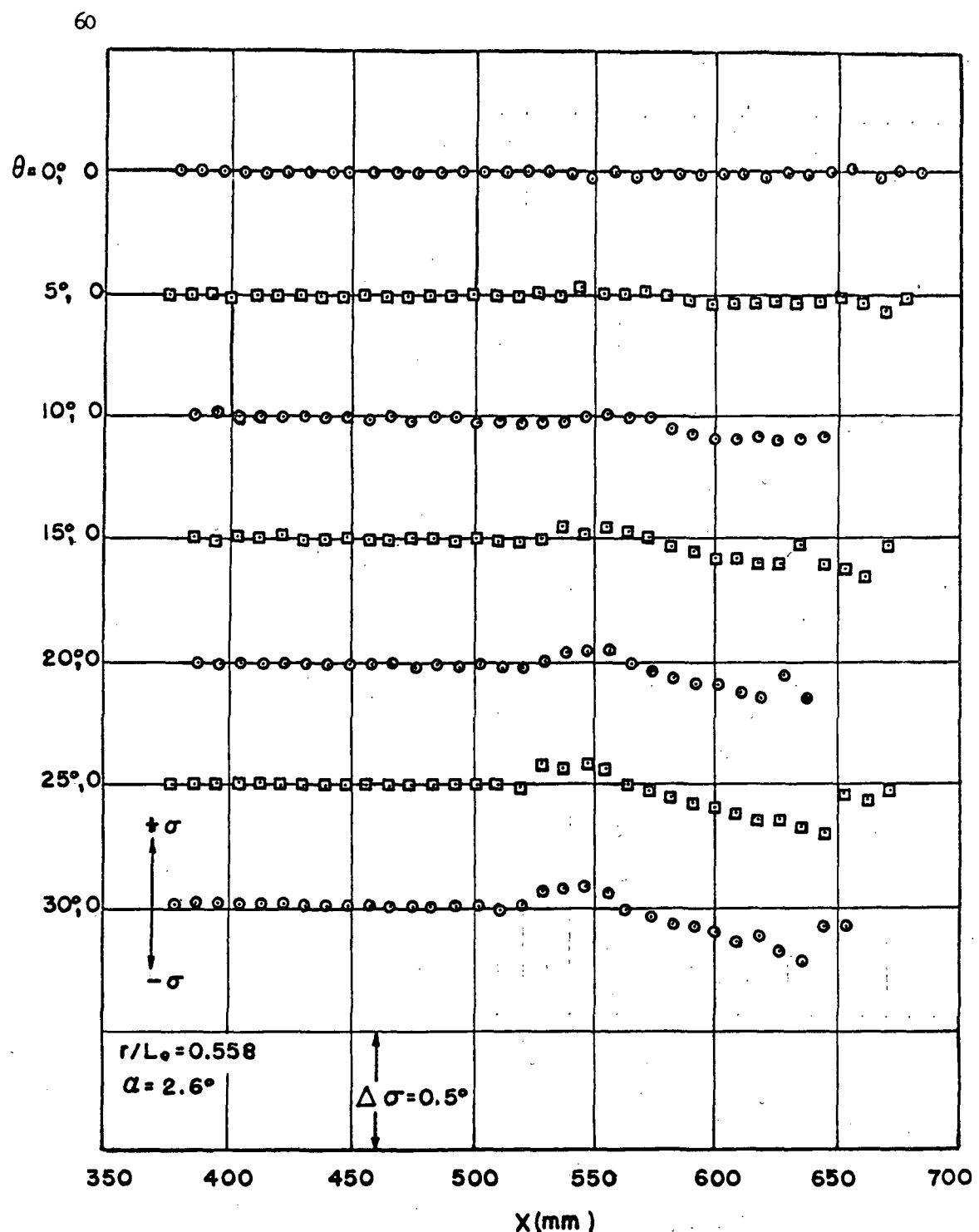


Fig 21a Experimental values of  $\sigma$  as function of distance at several meridian planes

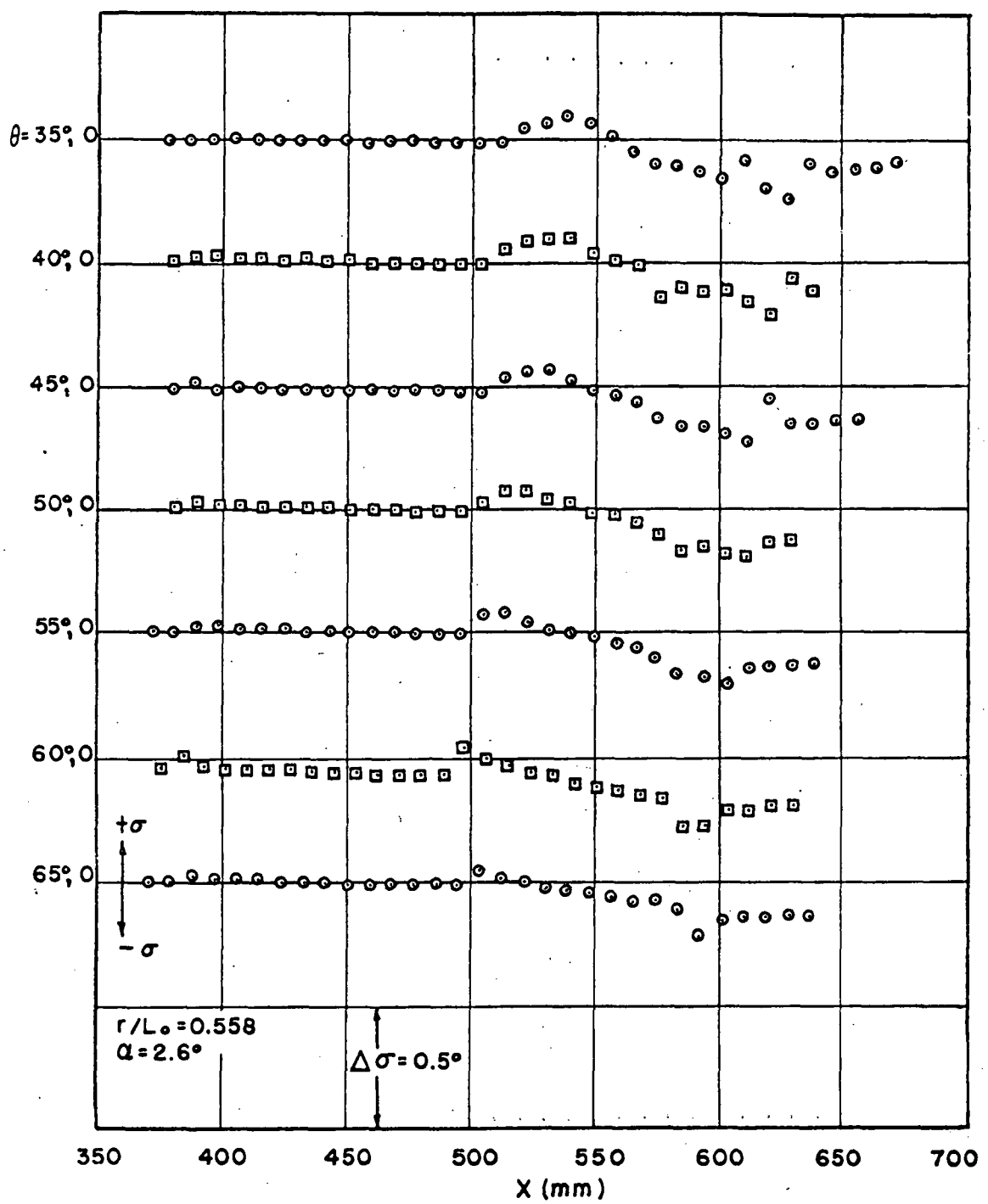


Fig 21b Continued

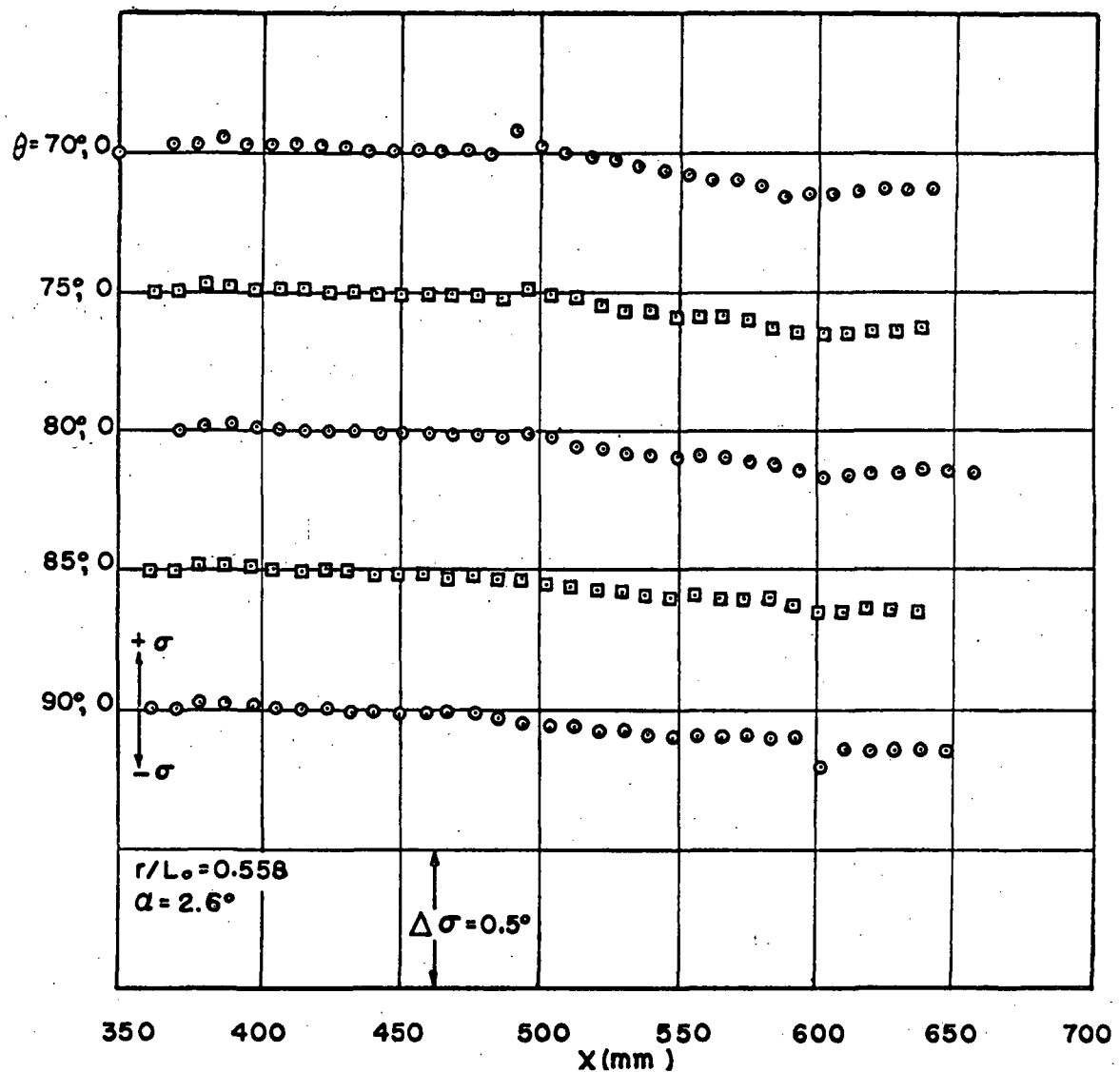


Fig 21c Continued

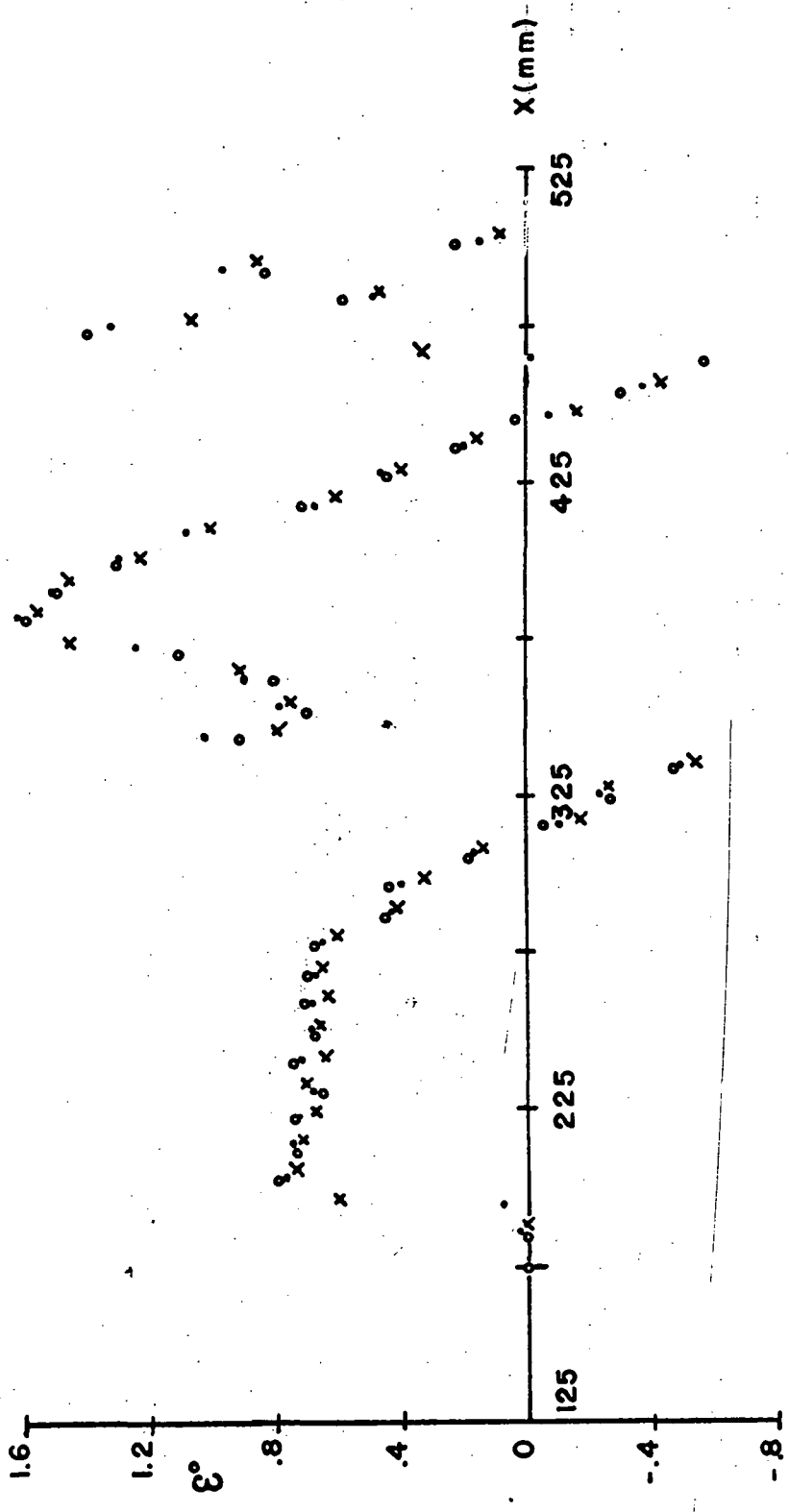


Fig 22 Distribution of deviation angle  $\epsilon$  at  $r/L_o = 0.271$ ,  $\alpha = 2.6^\circ$ ,  
for different longitudinal locations of the model

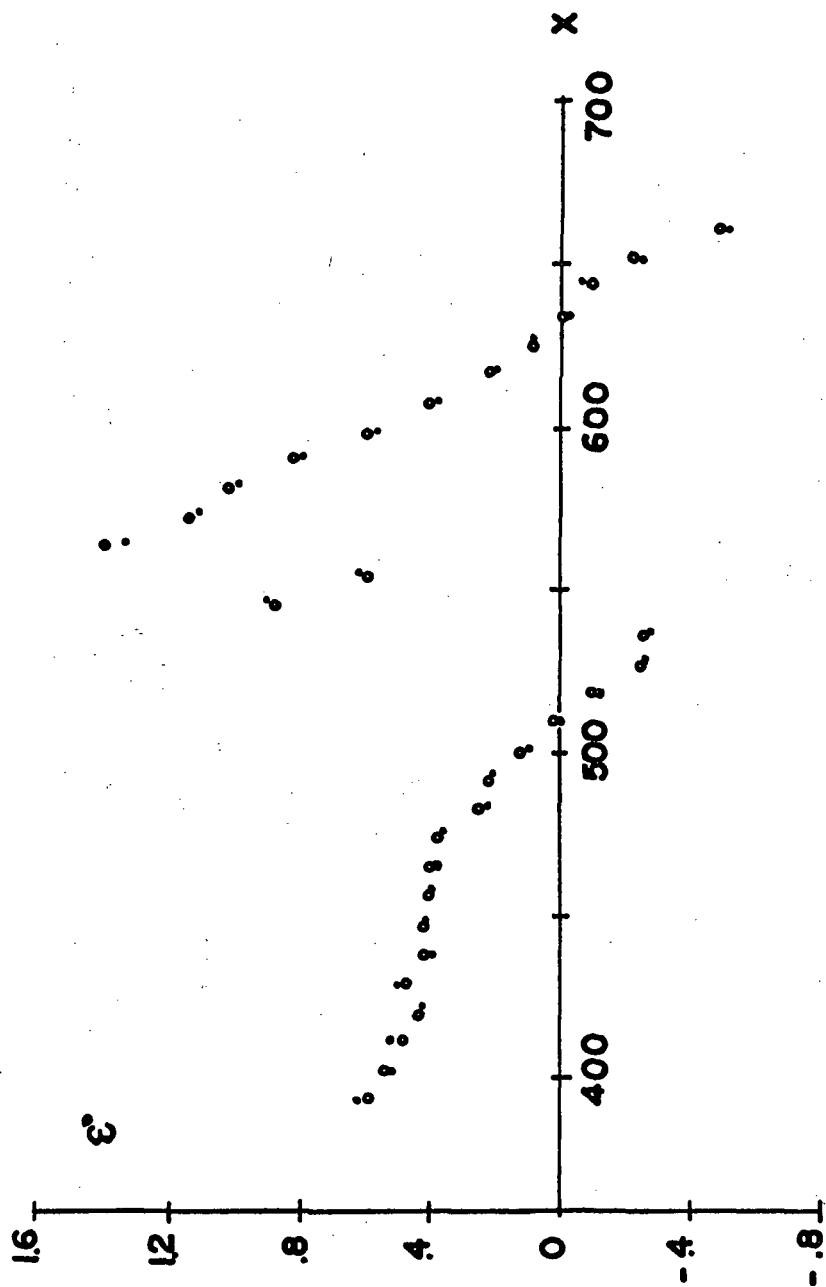


Fig 23 Distribution of  $\epsilon$  for different longitudinal location  
of the model ( $r/L_0 = 0.558$ ,  $\alpha = 2.6^\circ$ )

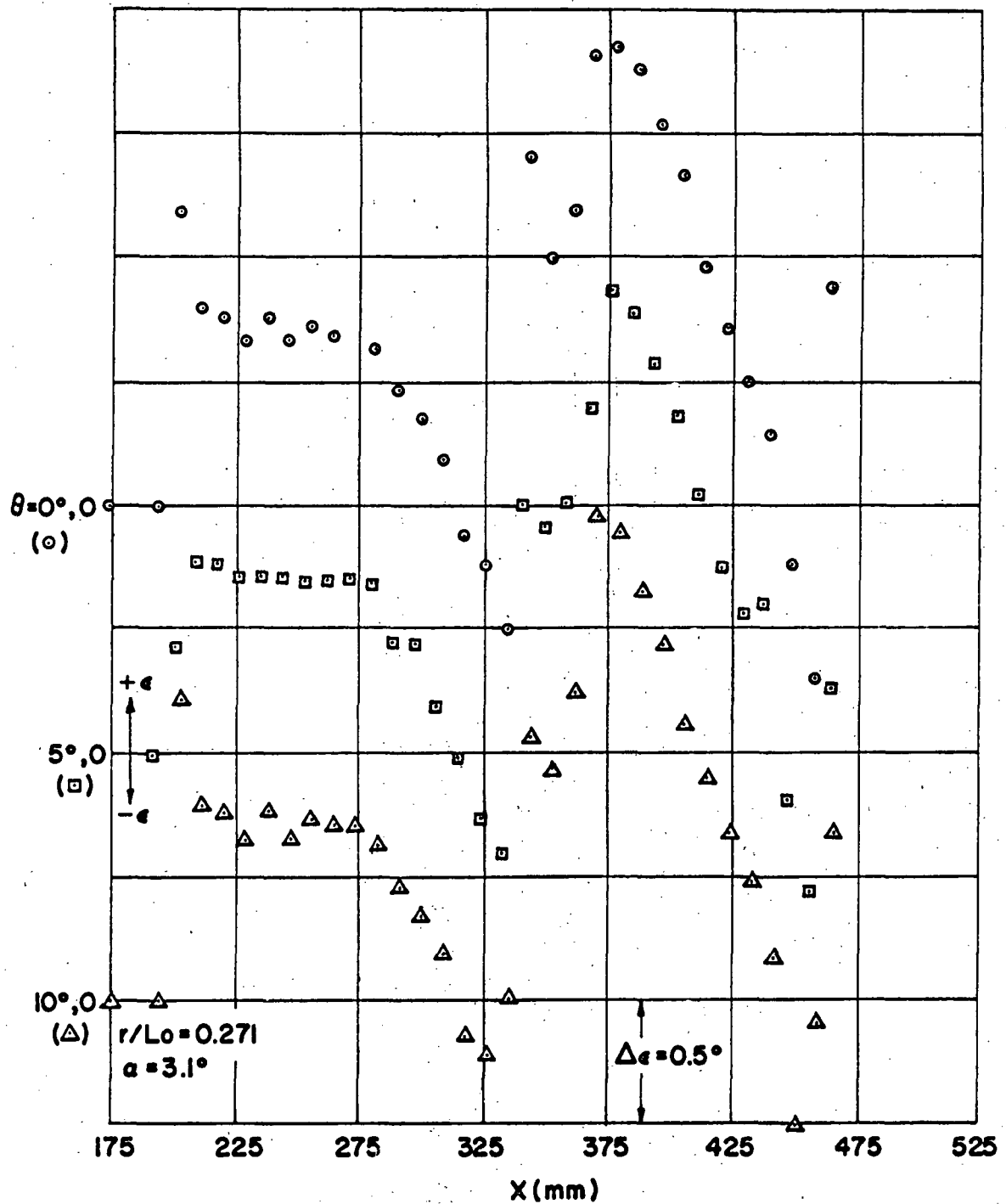


Fig 24a Experimental values of  $\epsilon$  as function of distance at several meridian planes

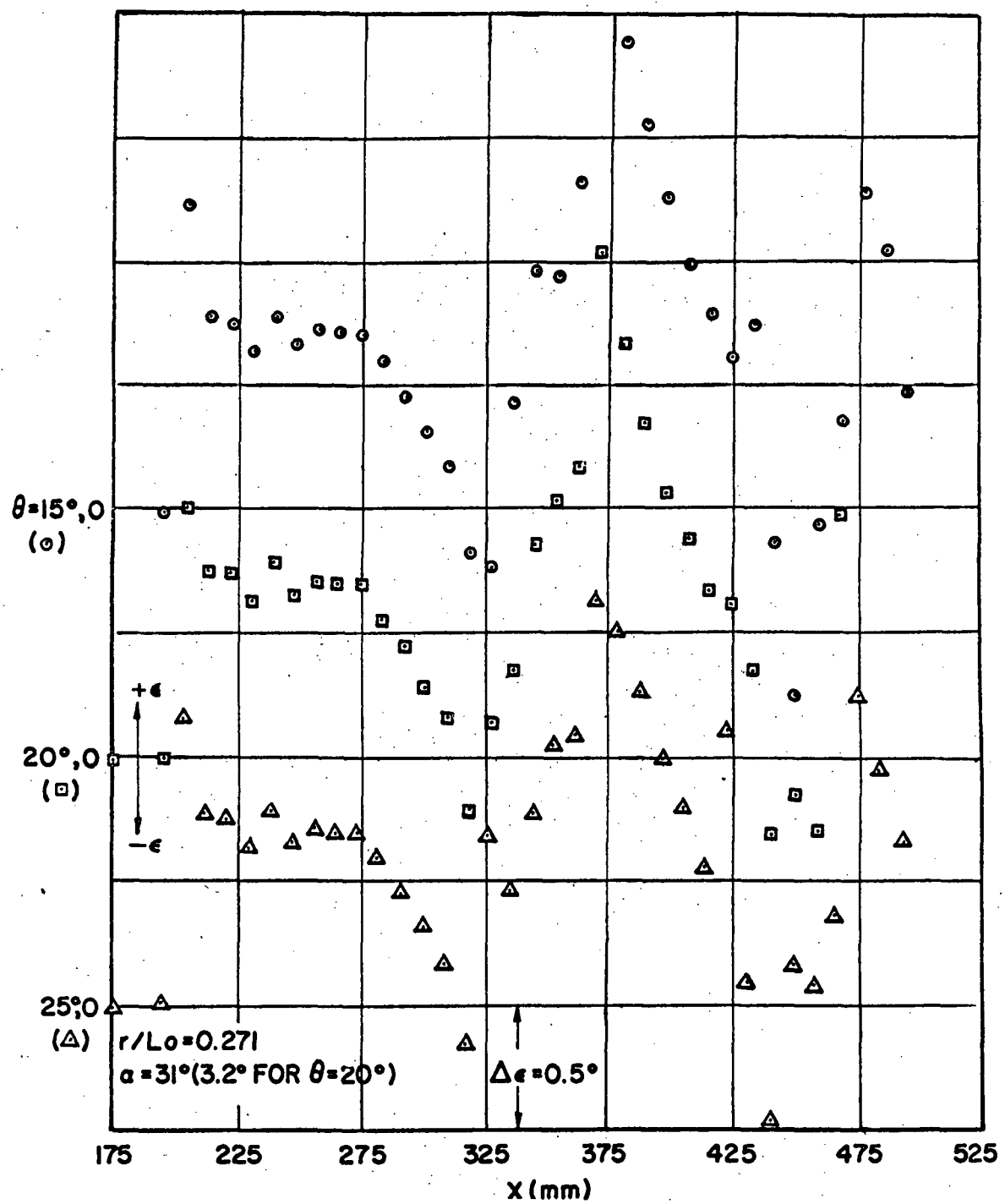


Fig 24b Continued

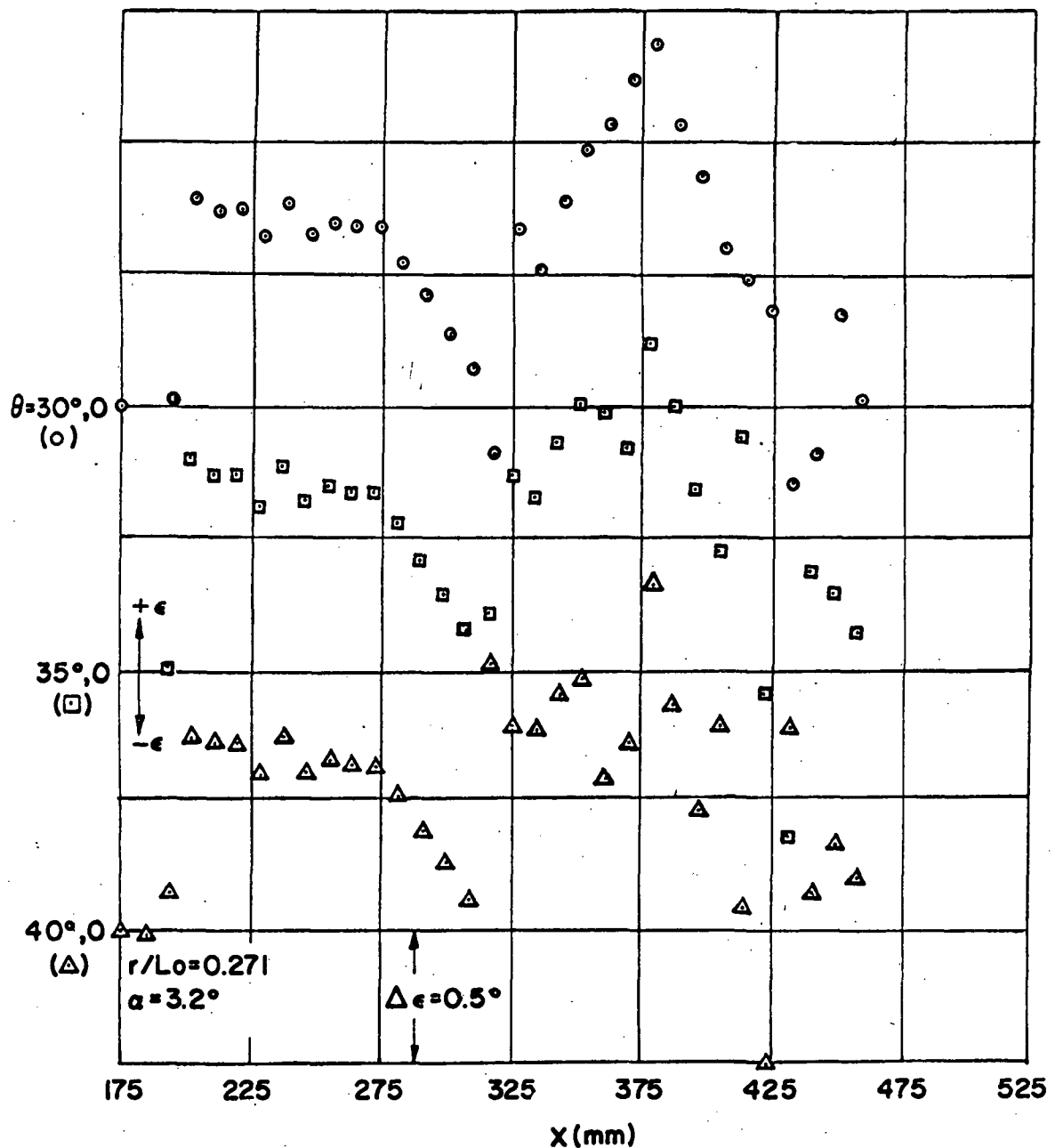


Fig 24c Continued

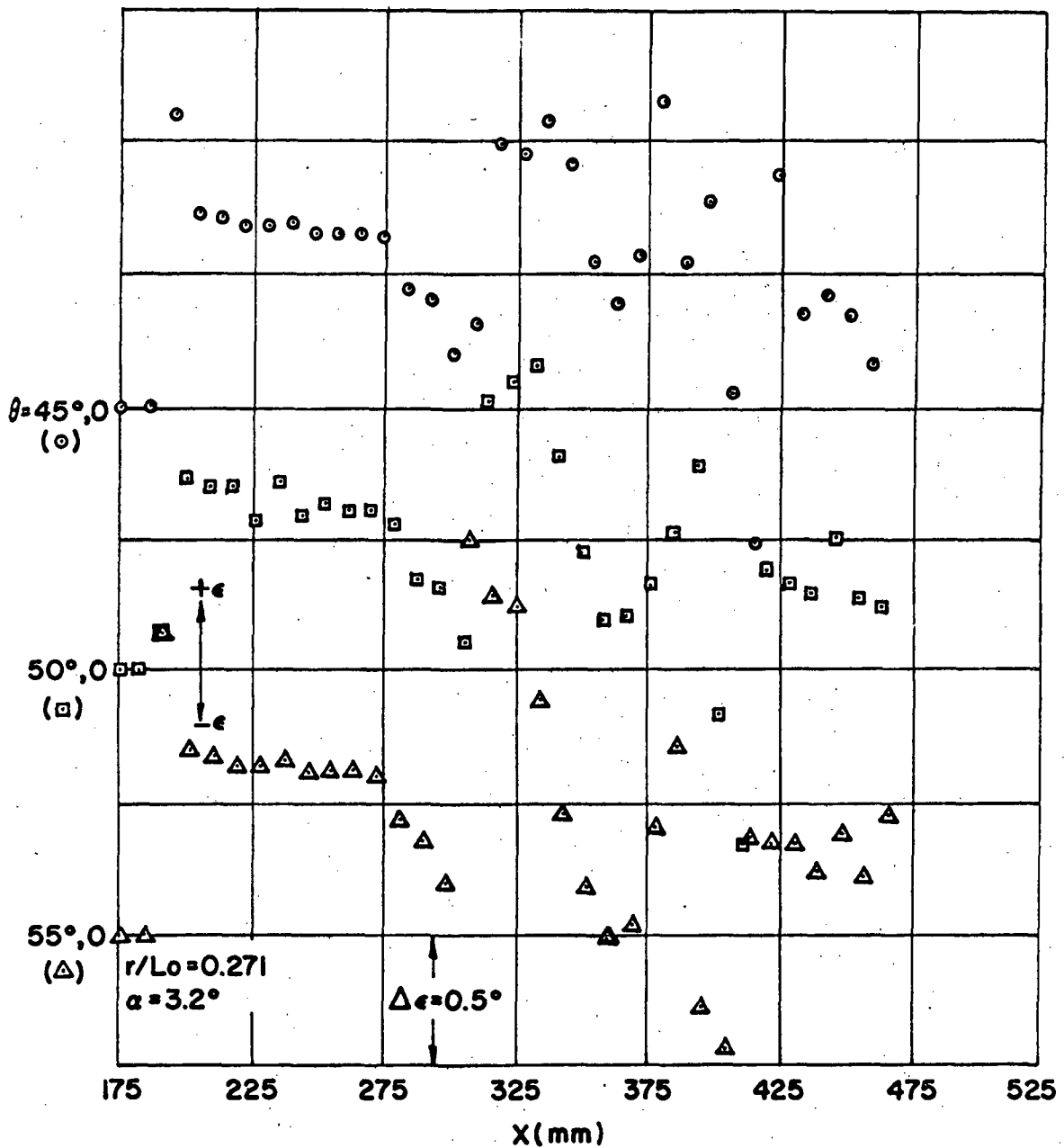


Fig 24d Continued

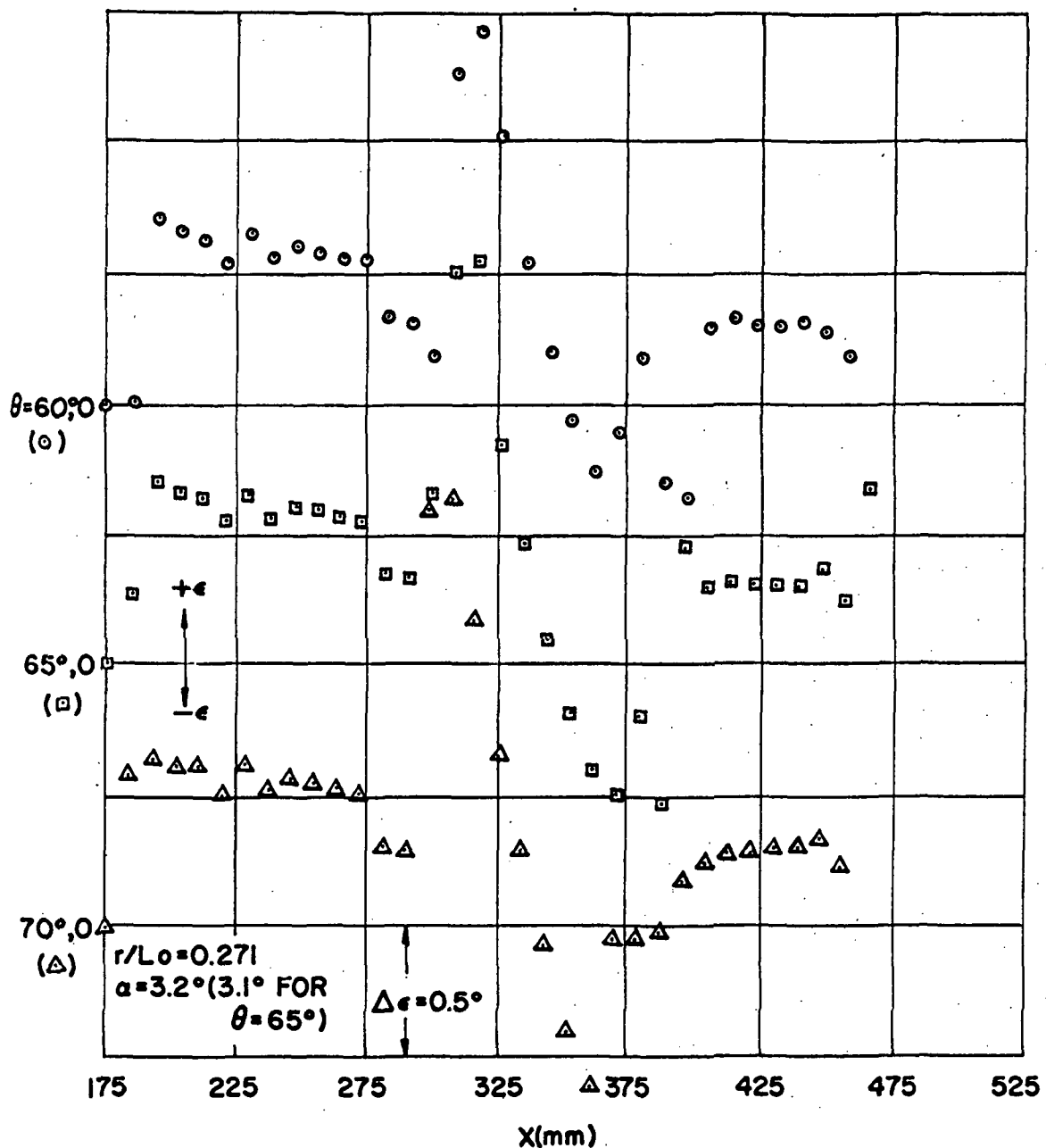


Fig 24e Continued

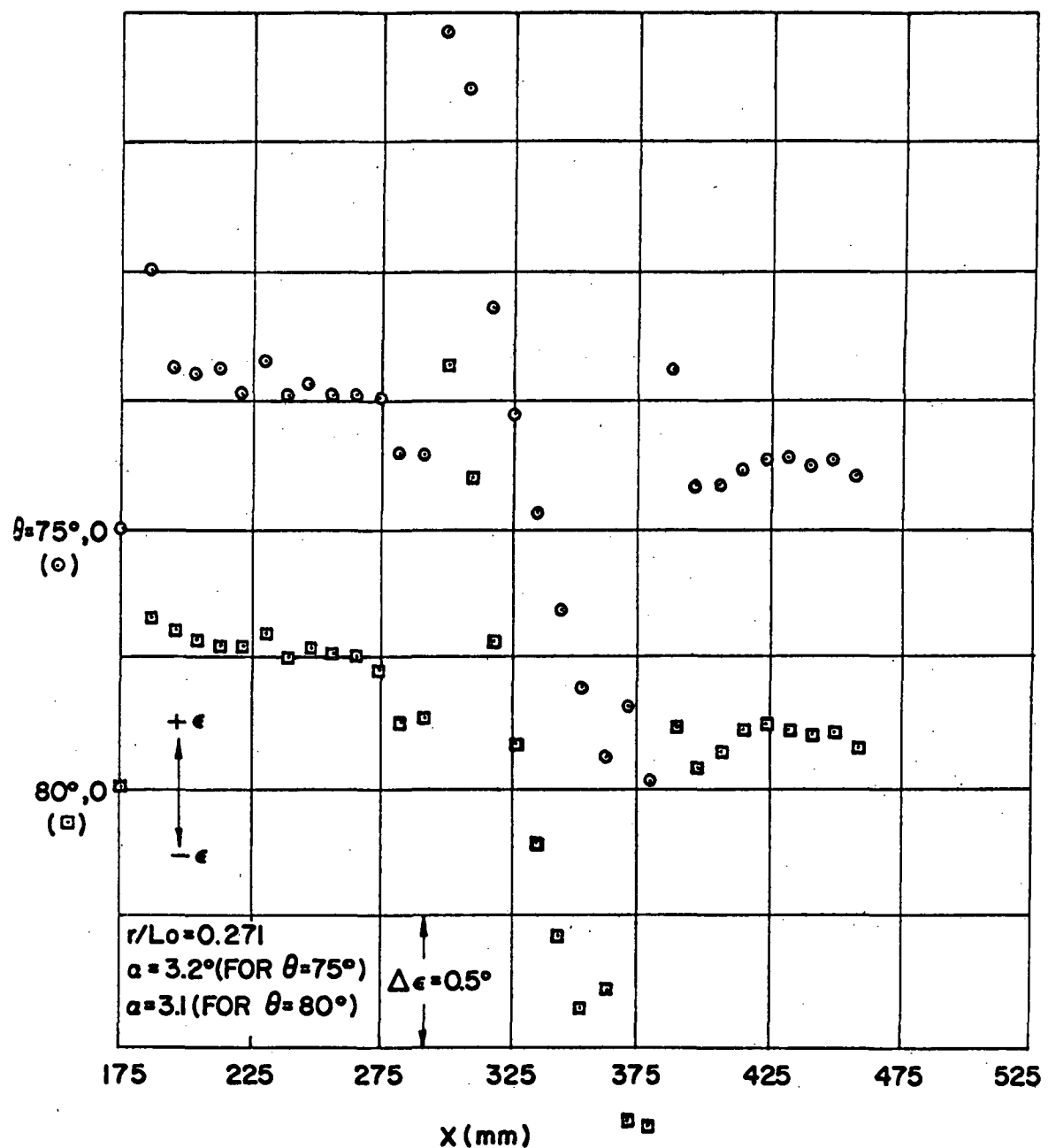


Fig 24f Continued

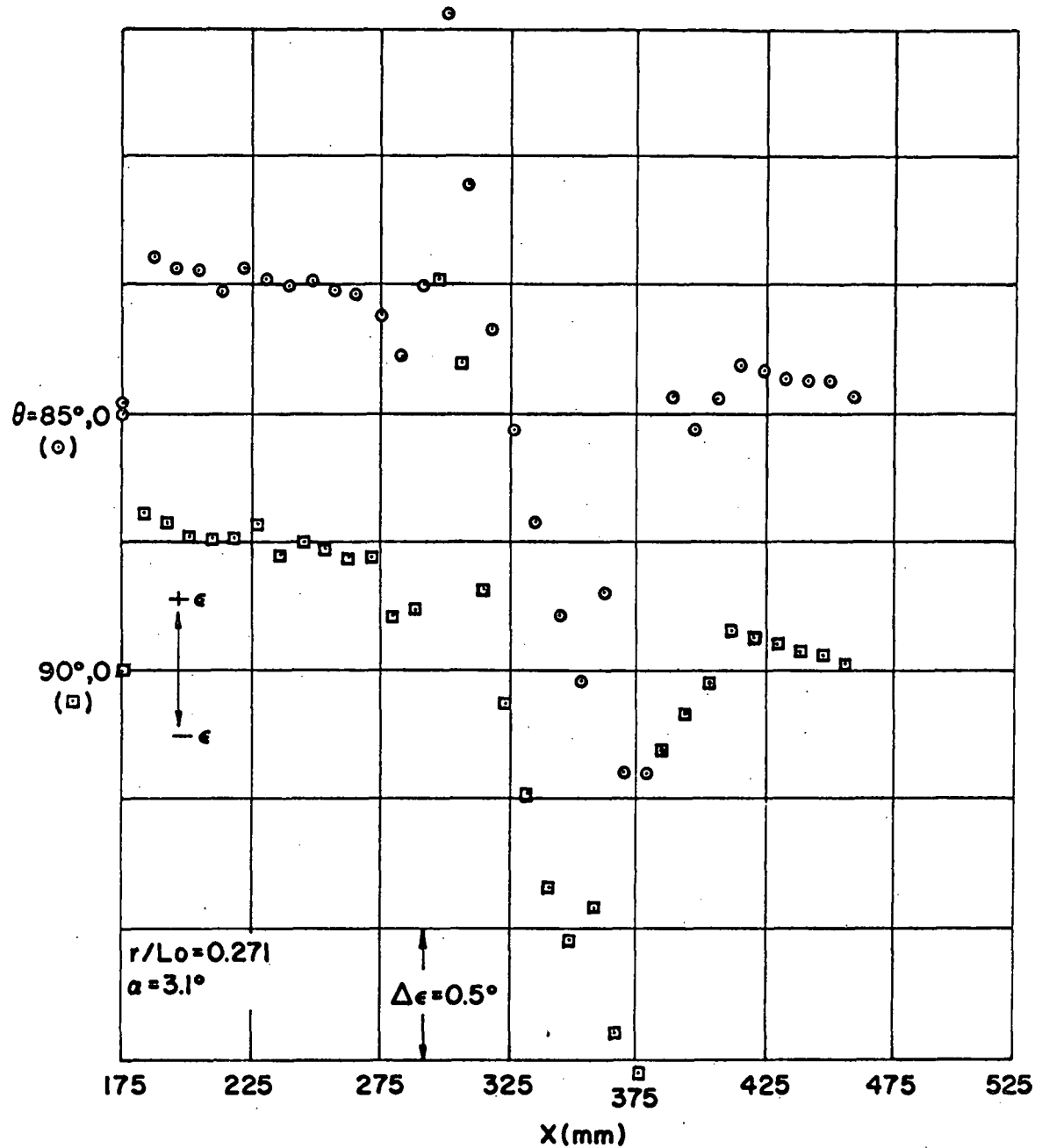


Fig 24g Continued

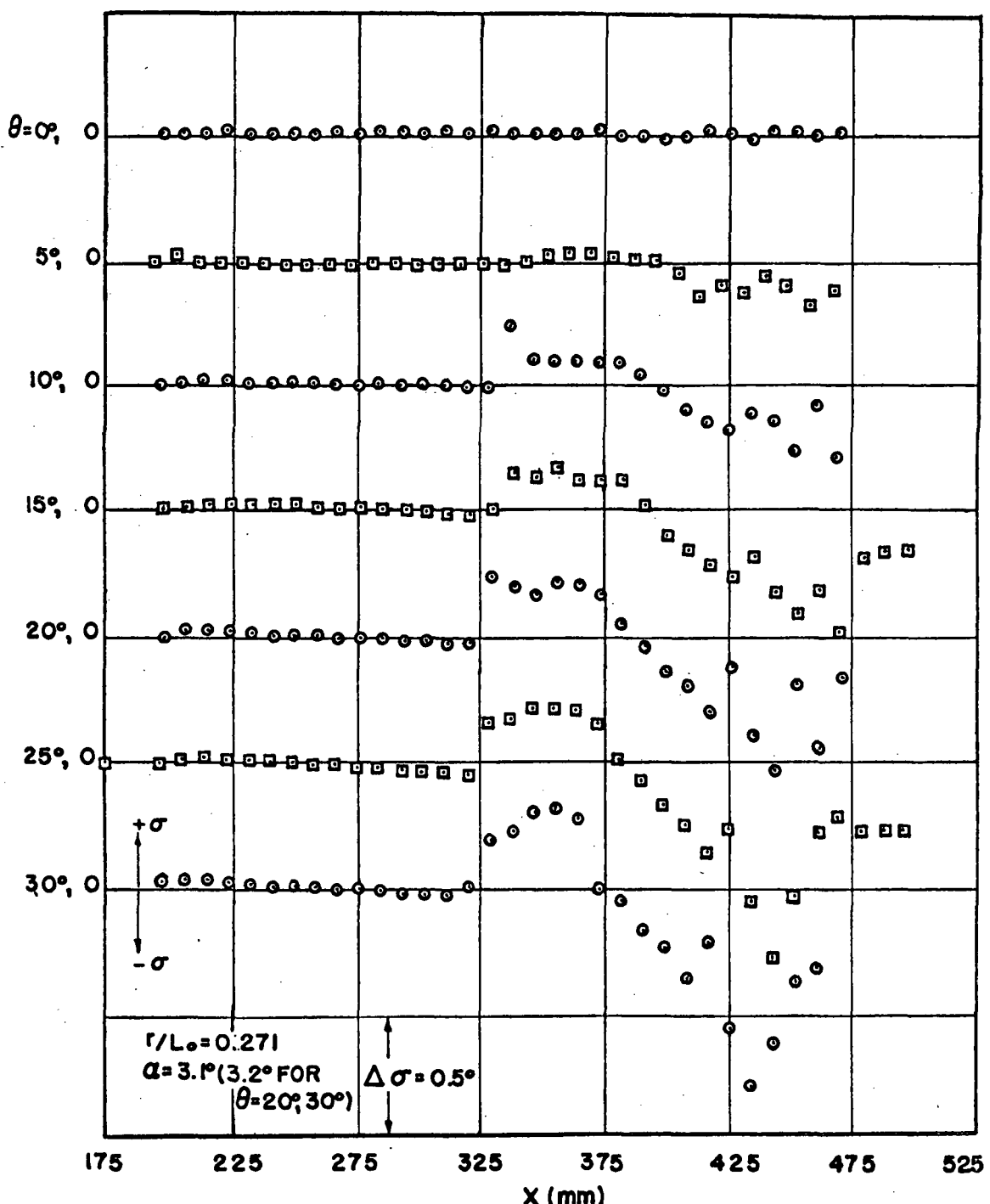


Fig 25a Experimental values of  $\sigma$  as function of distance at several meridian planes

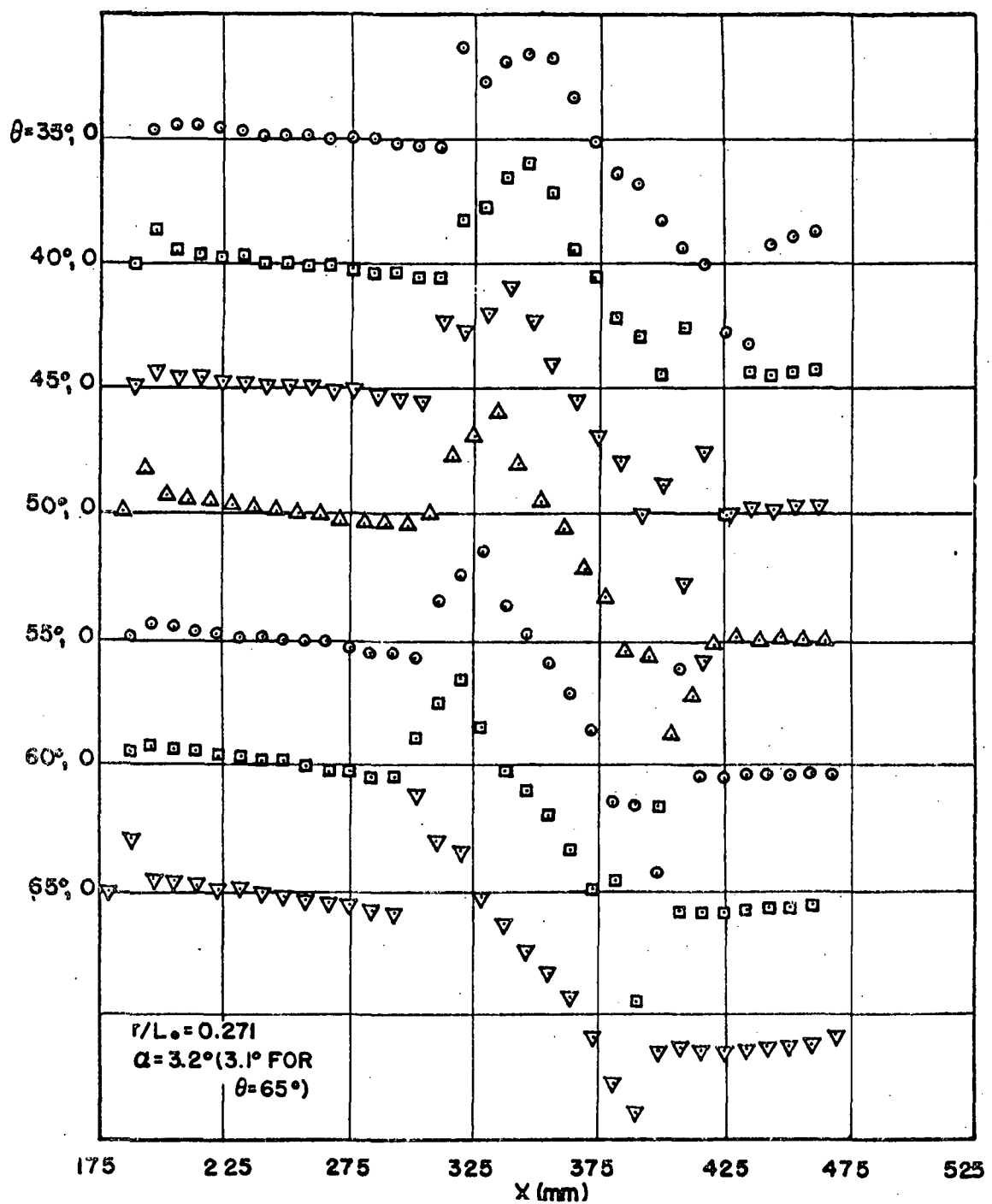


Fig 25b Continued

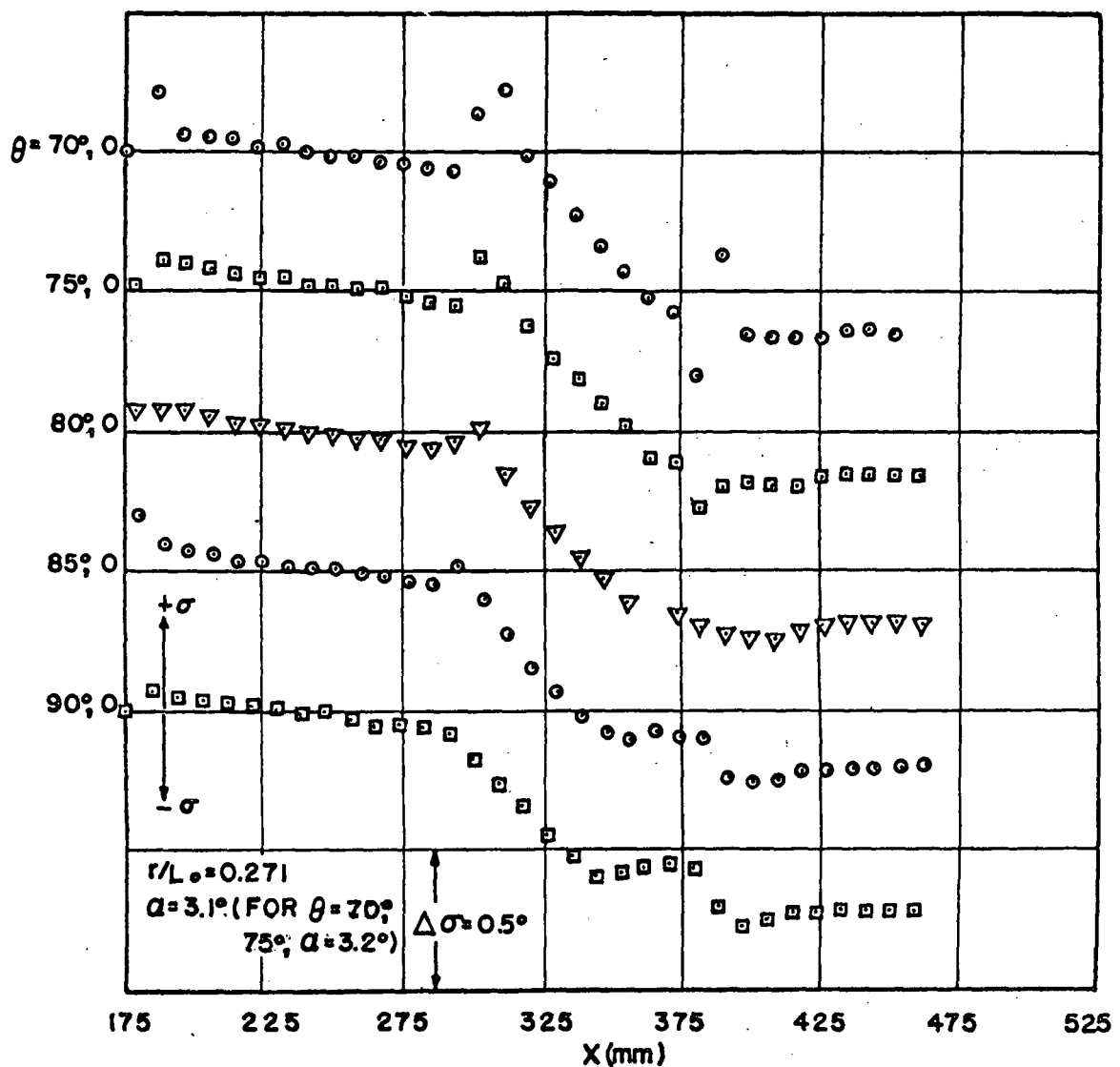


Fig 25c Continued

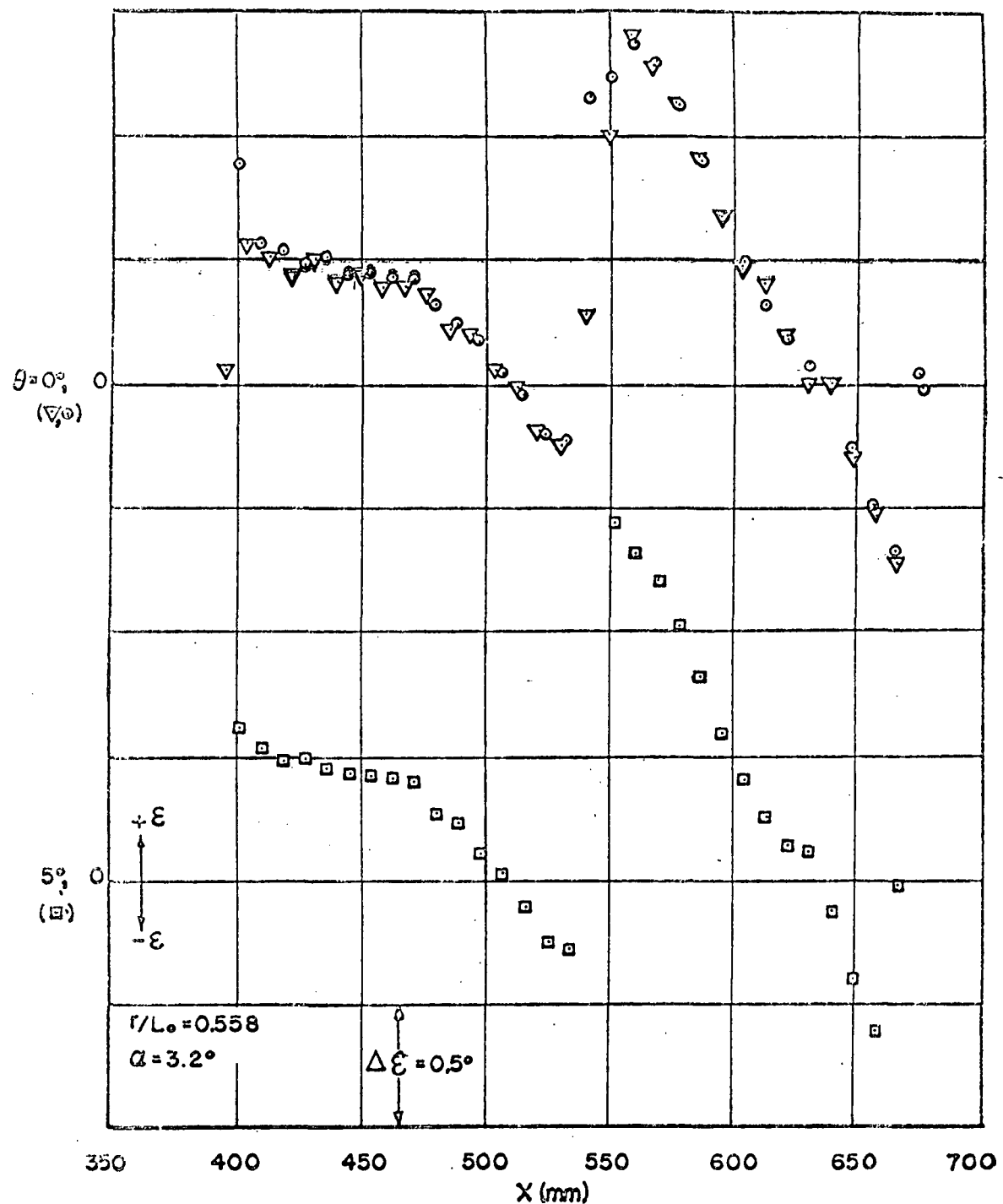


Fig 26a Experimental values of  $\epsilon$  as function of distance at several meridian planes

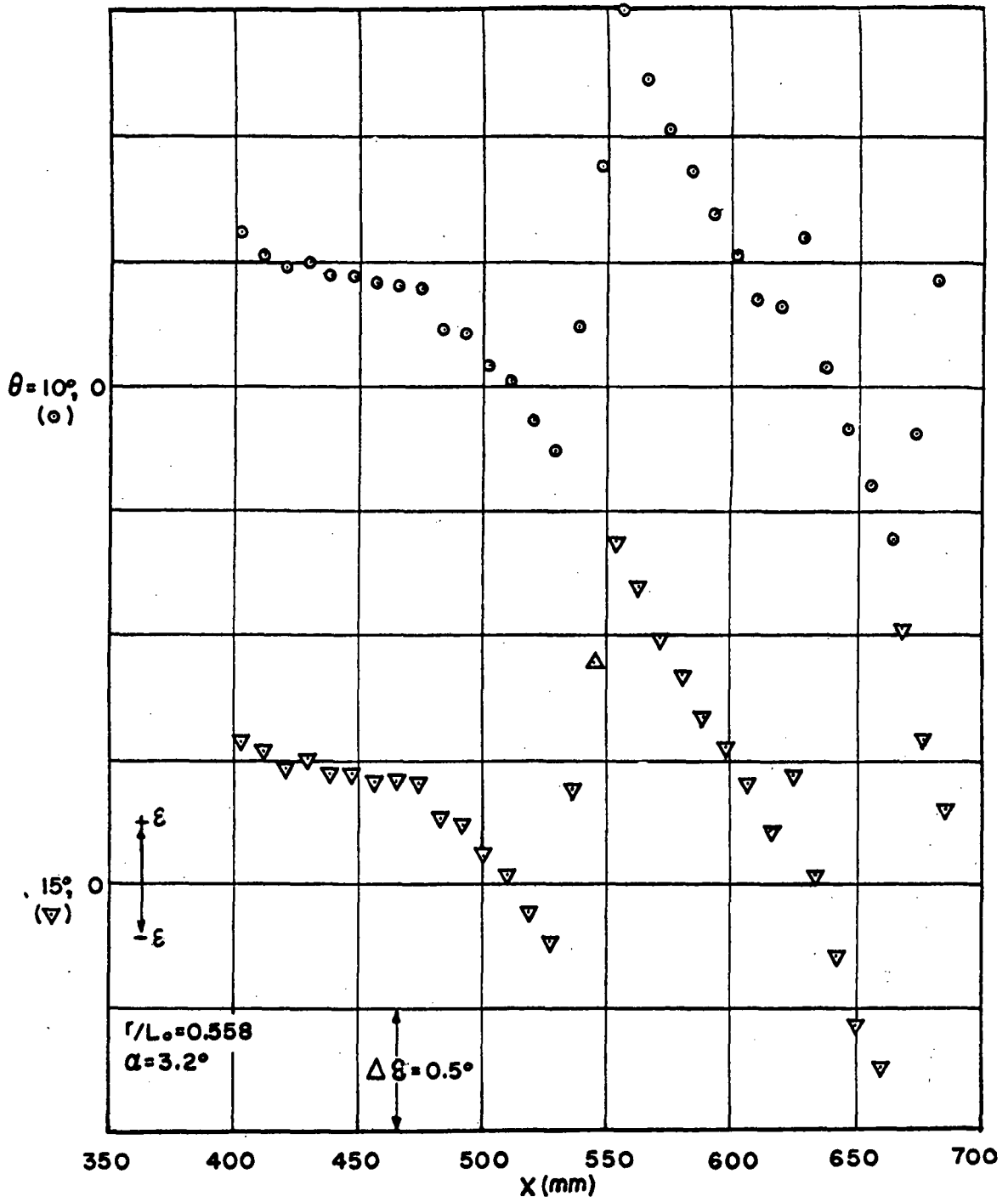


Fig 26b Continued

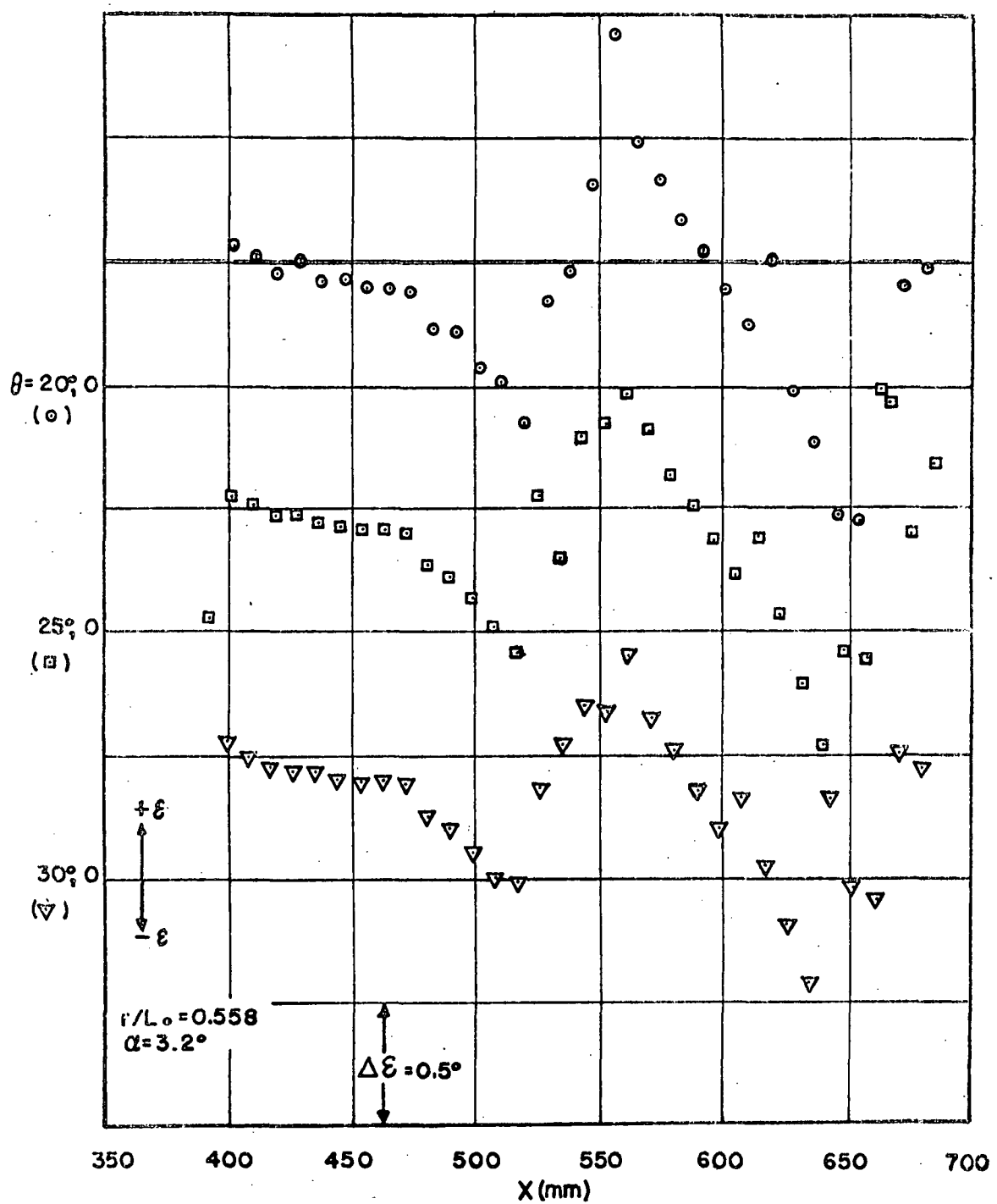


Fig 26c. Continued

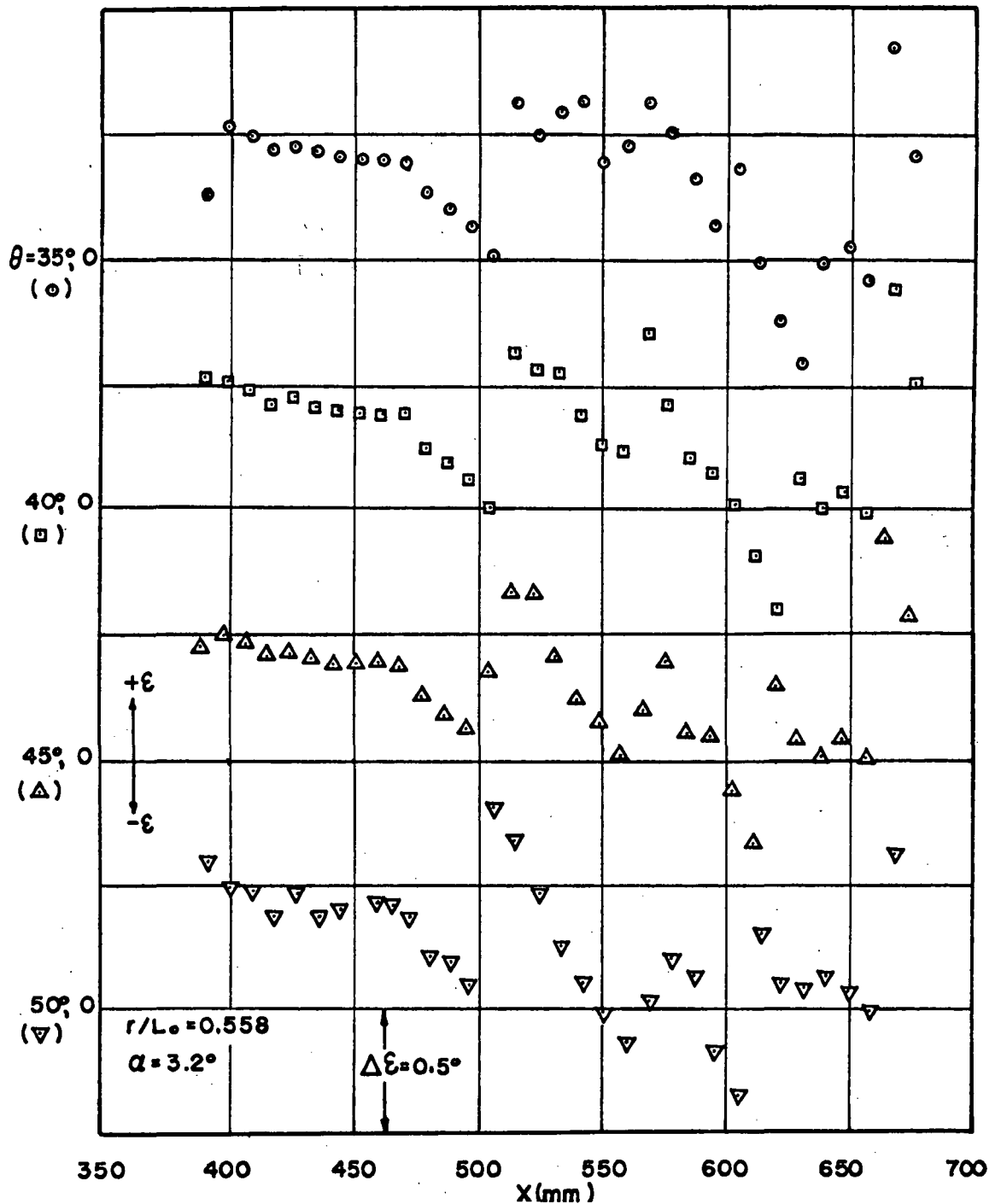


Fig 26d Continued

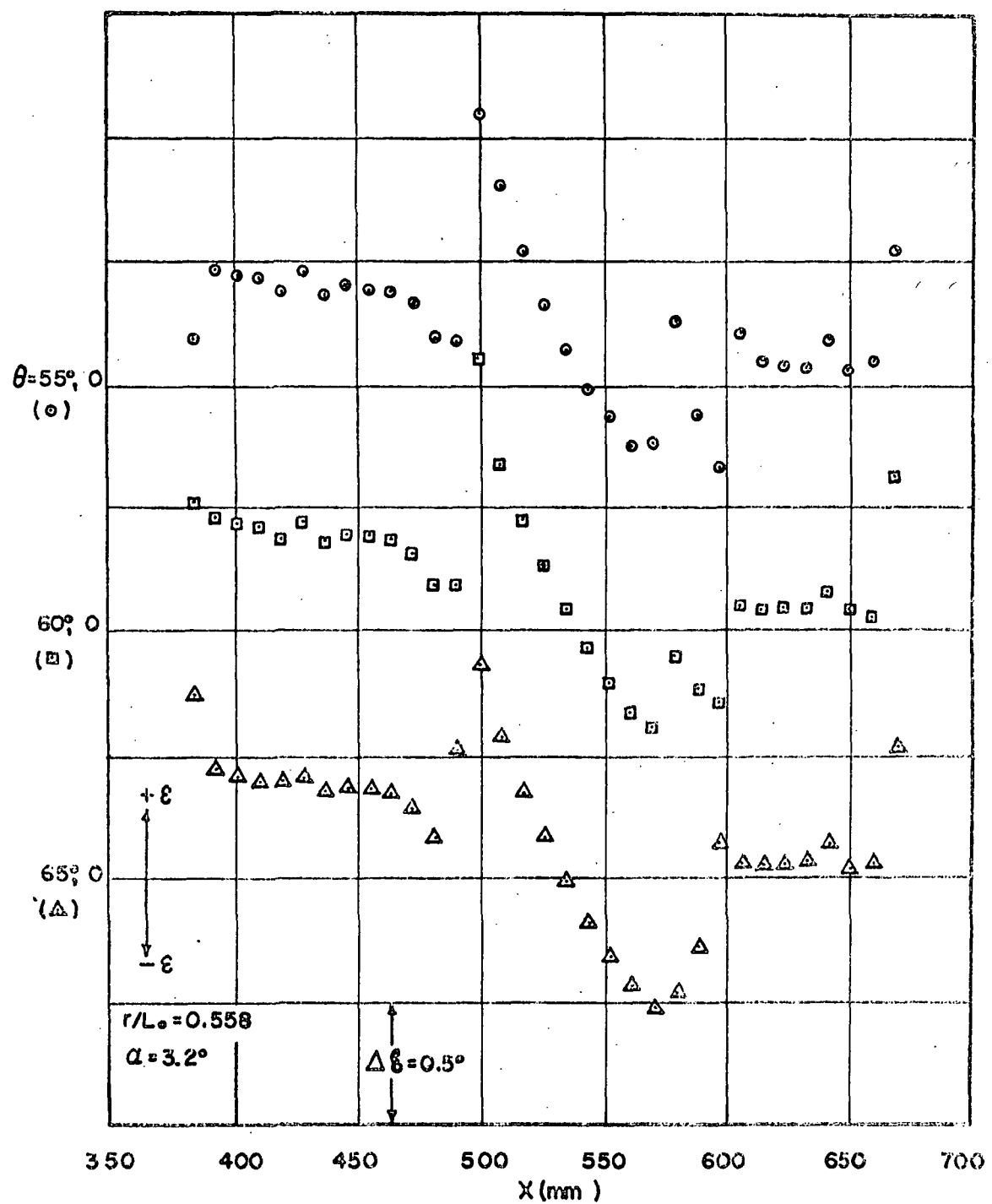


Fig 26e Continued

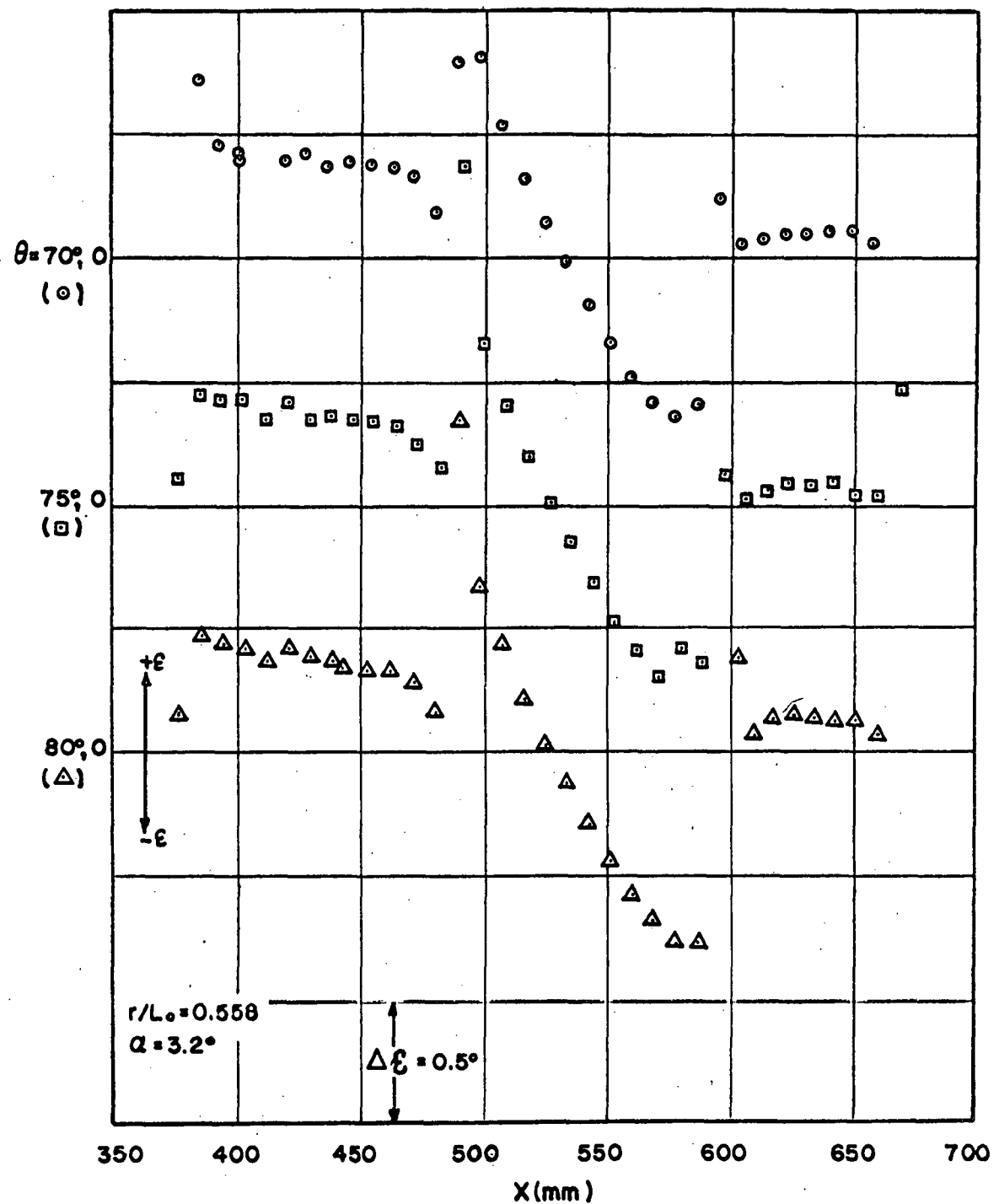


Fig 26f Continued

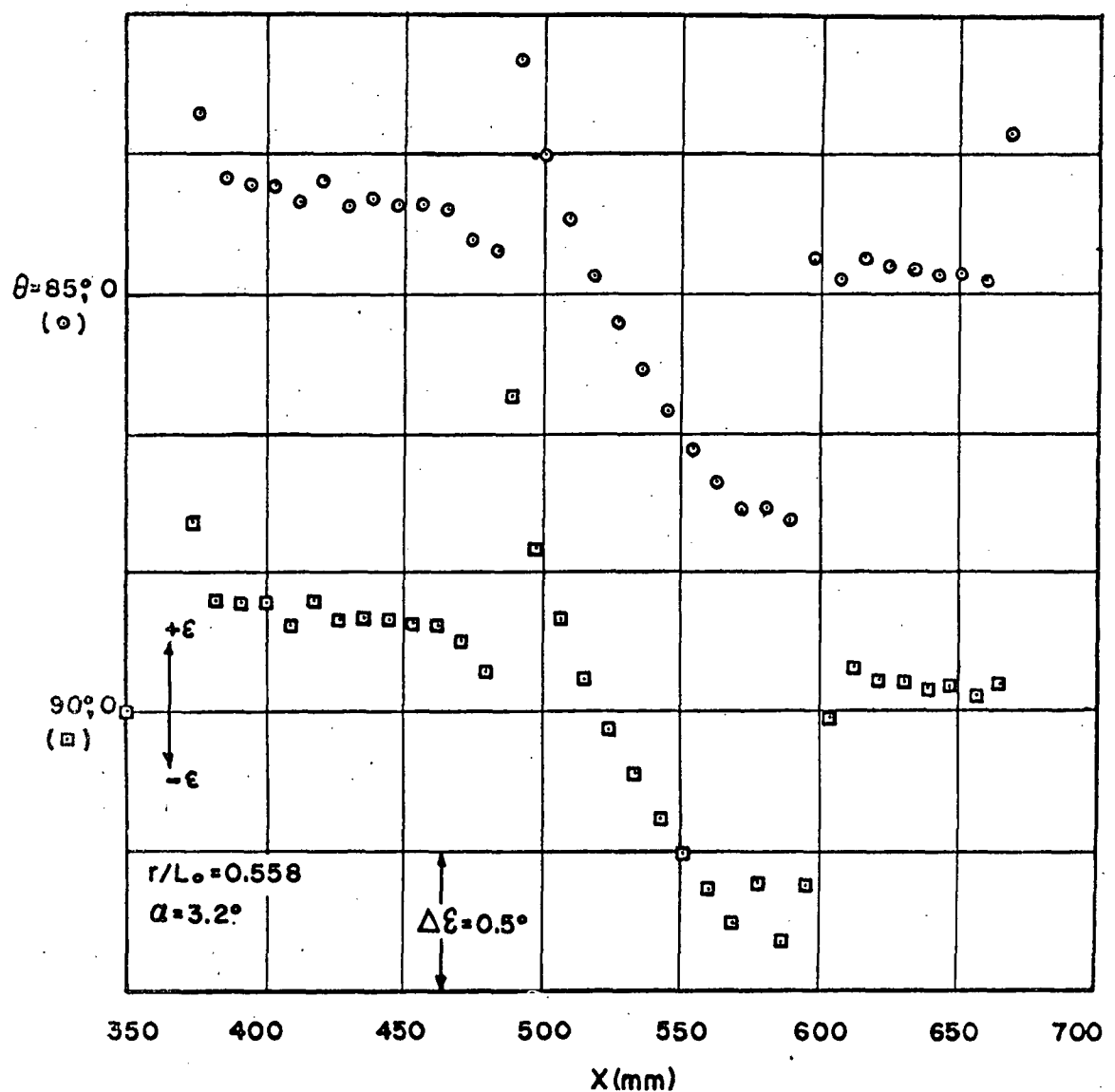


Fig 26g Continued

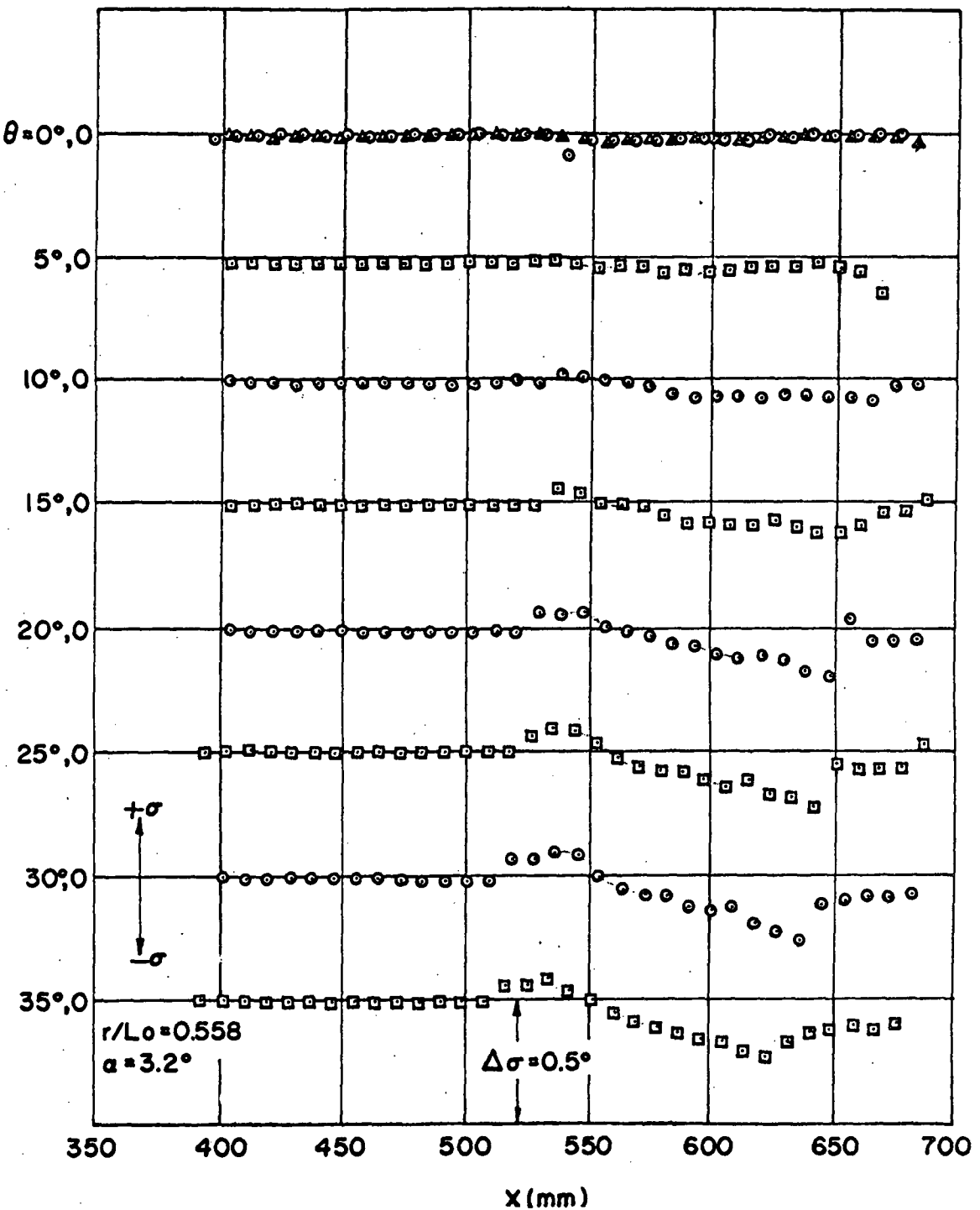


Fig 27a Experimental values of  $\sigma$  as function of distance at several meridian planes

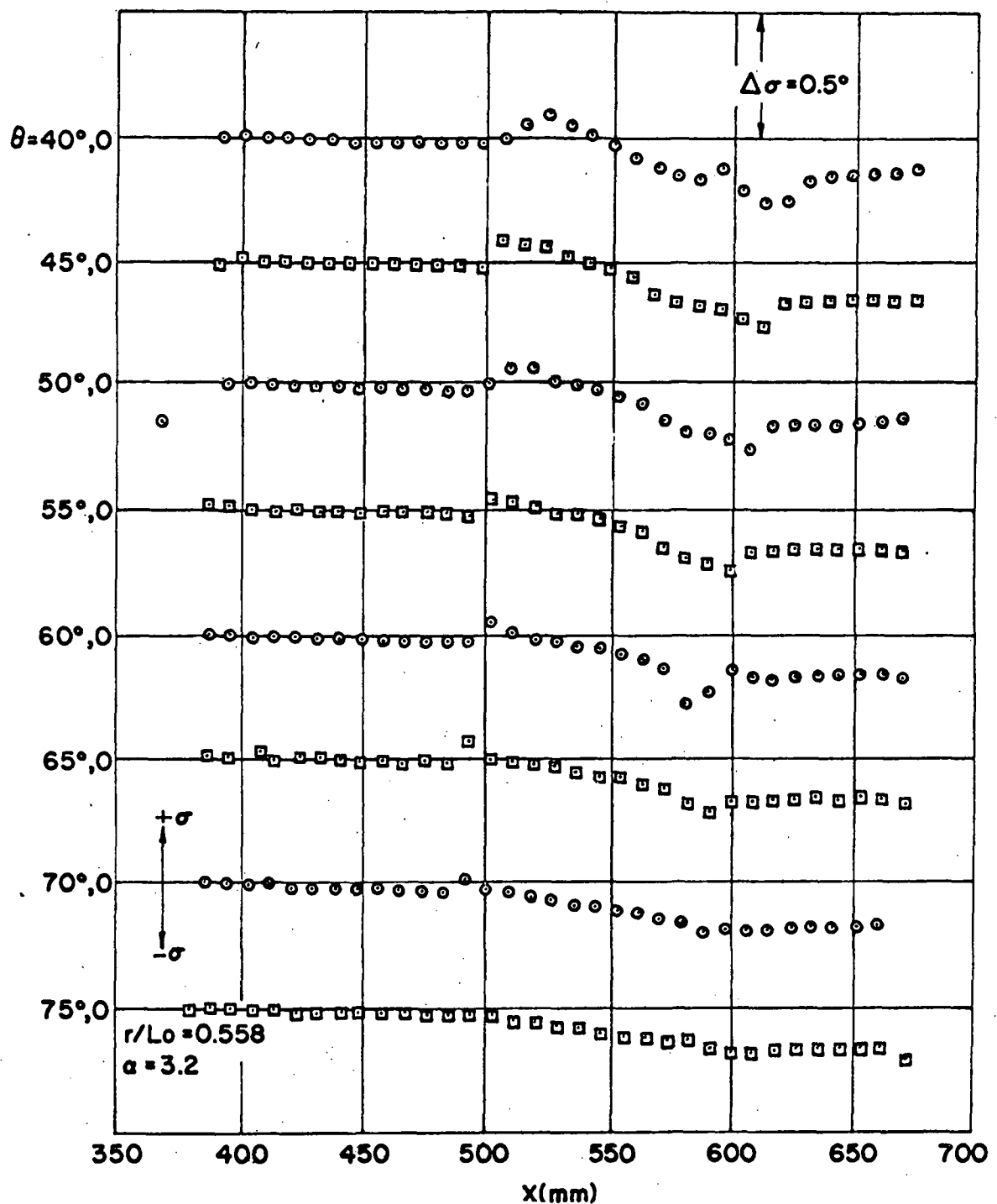


Fig 27b Continued

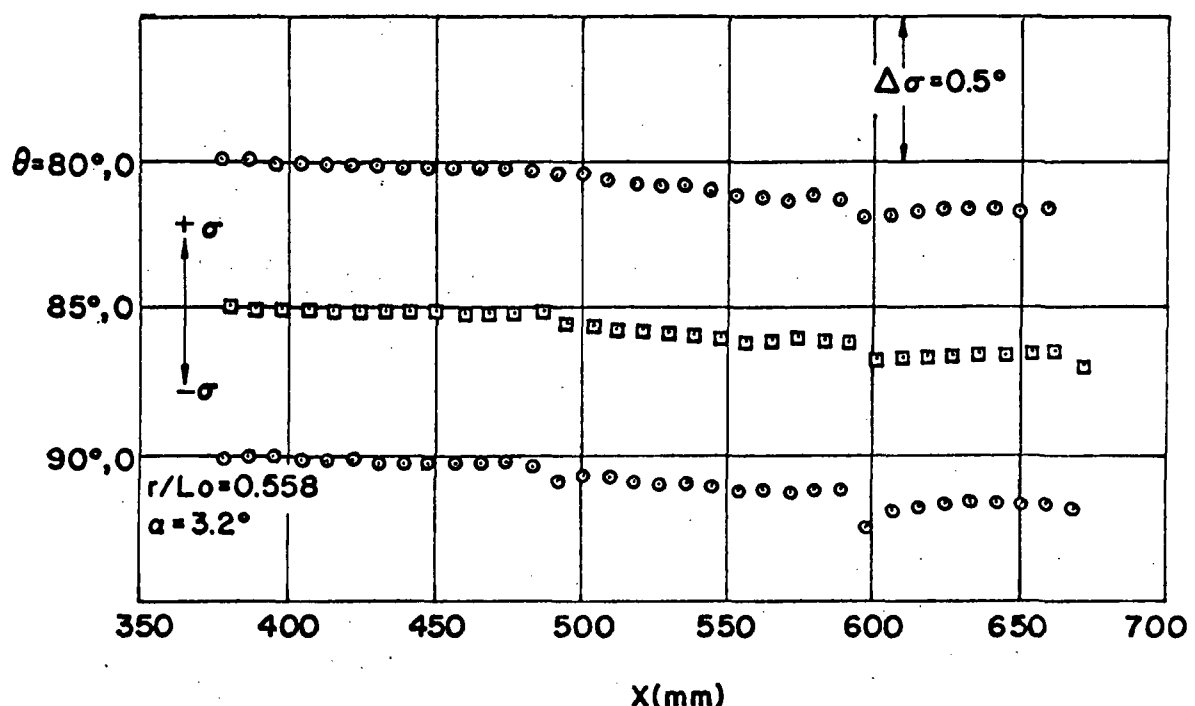


Fig 27c Continued

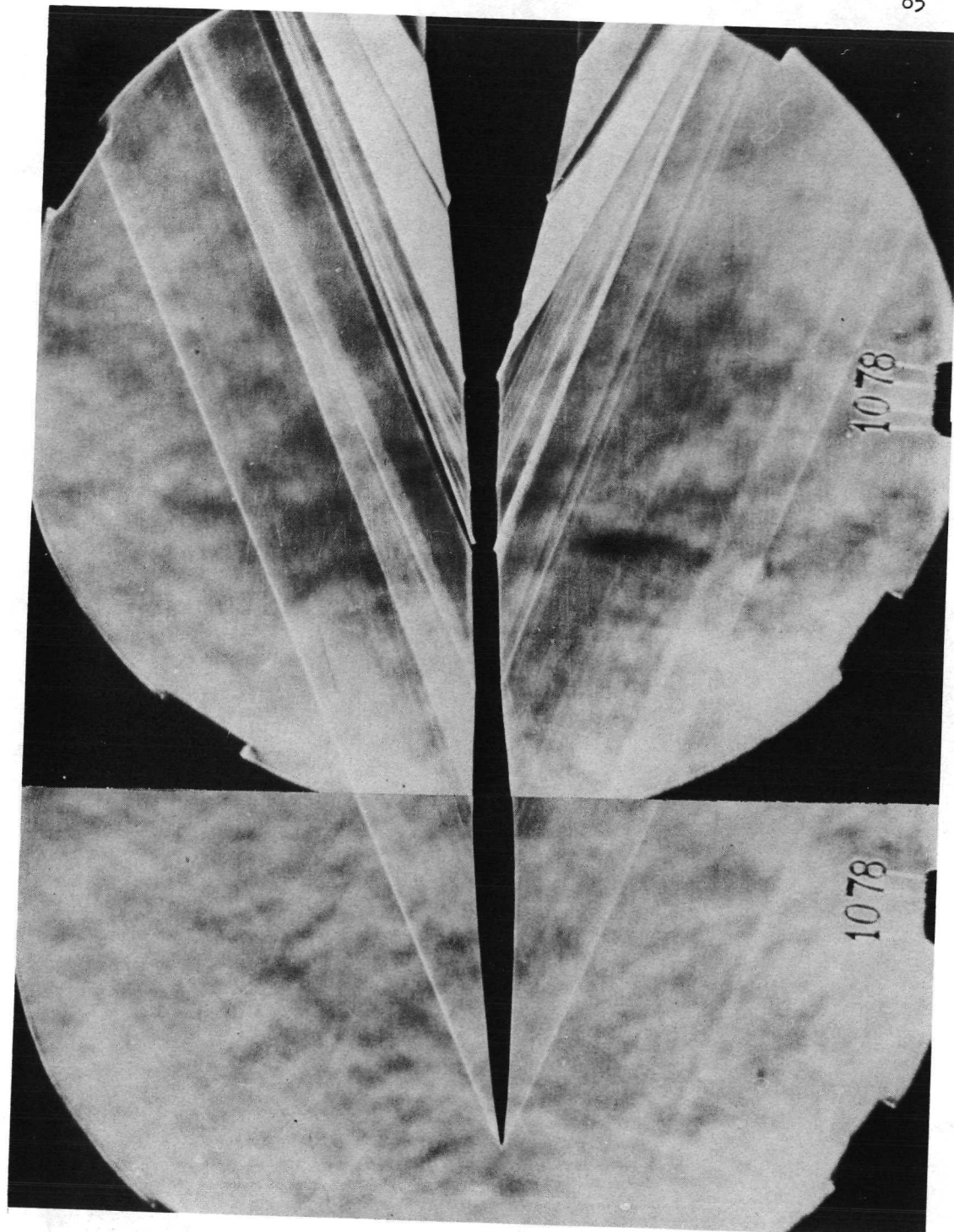


Fig. 28a Schlieren photographs  
at  $\alpha = 2.6^\circ$ ,  $\theta = 0^\circ$

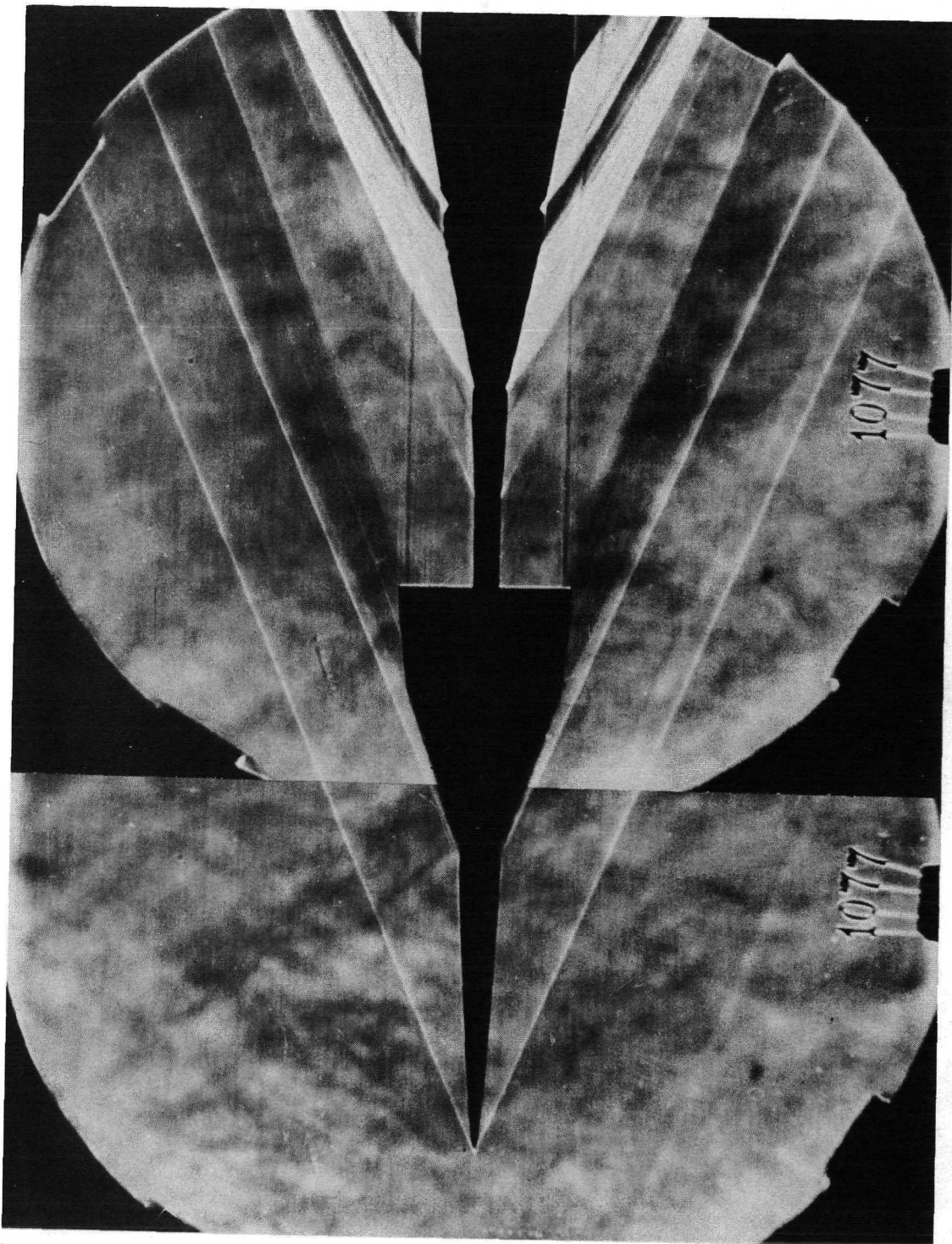


Fig. 28b Schlieren photographs  
at  $\alpha = 2.6^\circ$ ,  $\theta = 90^\circ$

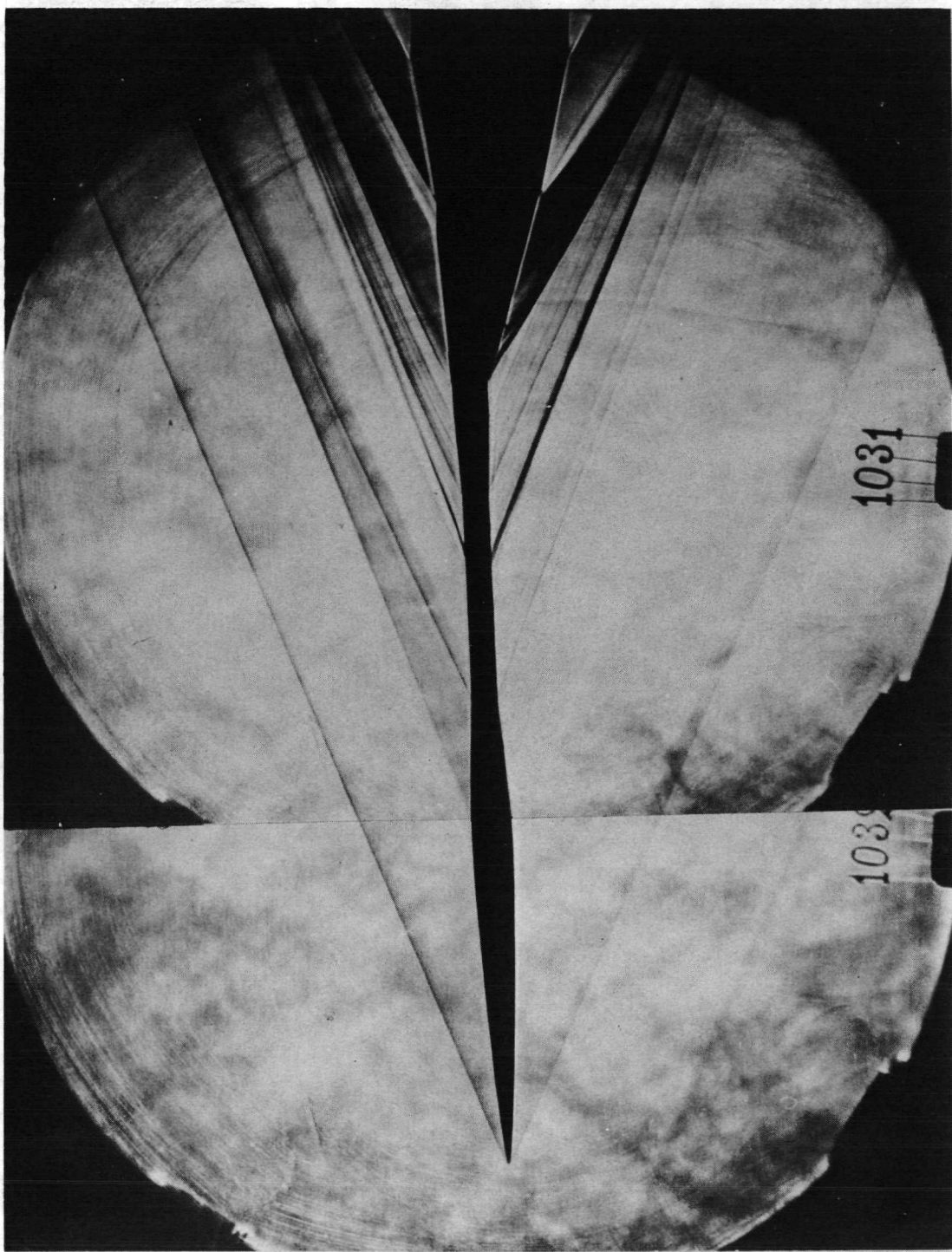


Fig. 29a Schlieren photographs  
at  $\alpha = 3.2^\circ$ ,  $\theta = 0^\circ$

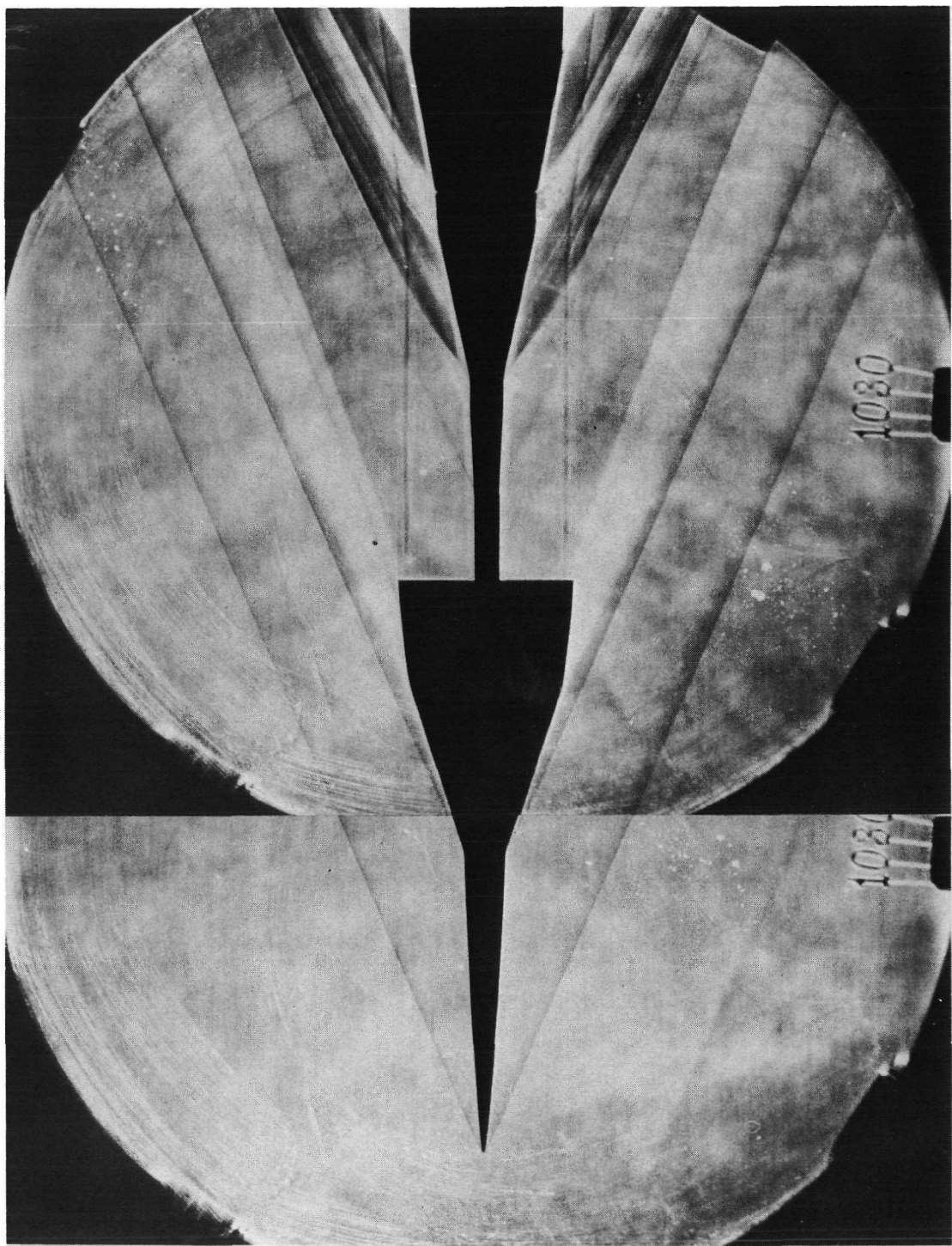


Fig 29b Schlieren photographs  
at  $\alpha = 3.2^\circ$ ,  $\theta = 90^\circ$

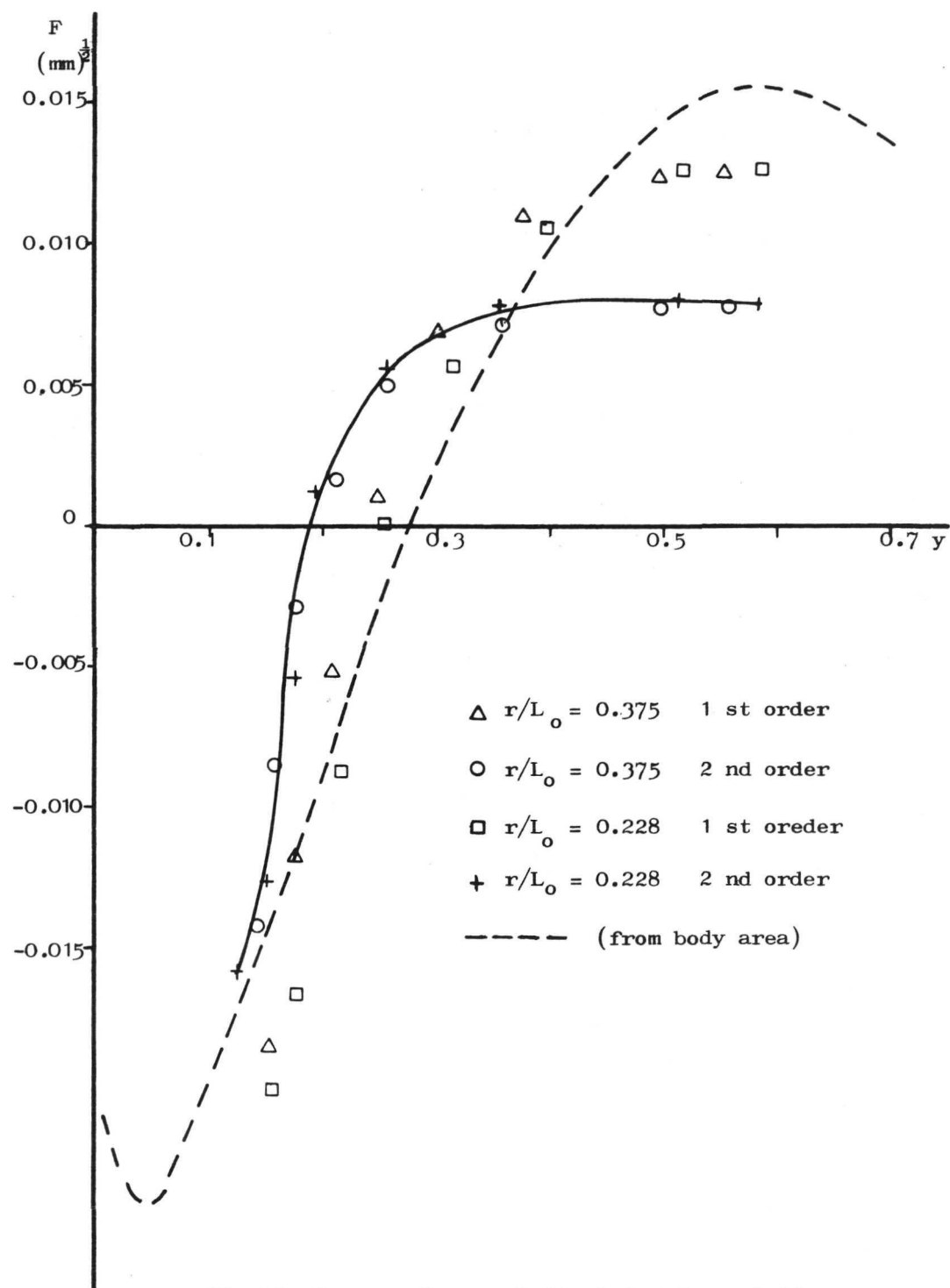


Fig 30 F-curve for parabolic body of revolution

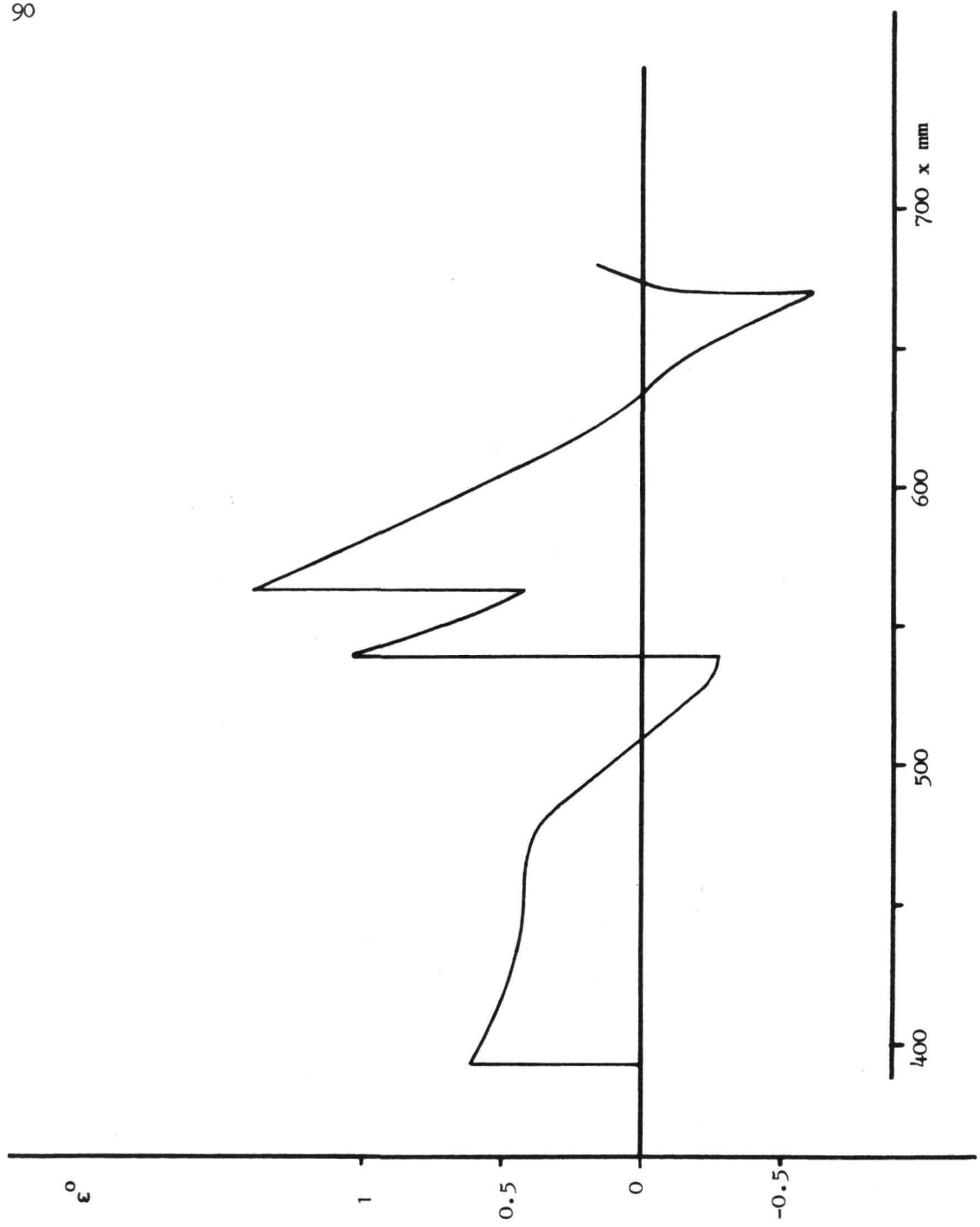


Fig 31 Chosen  $\epsilon$  distribution ( $r/L_o = 0.558$ )

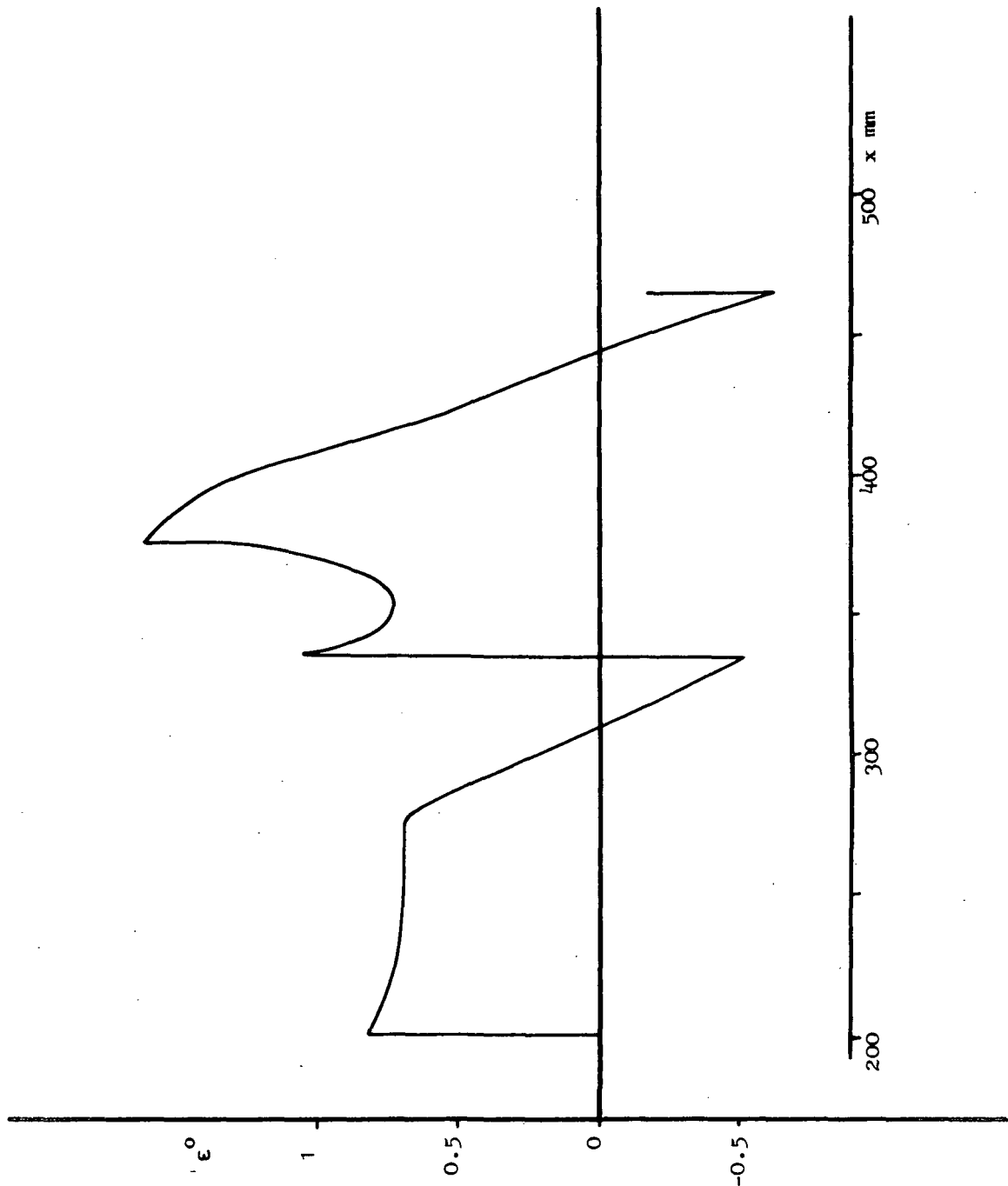
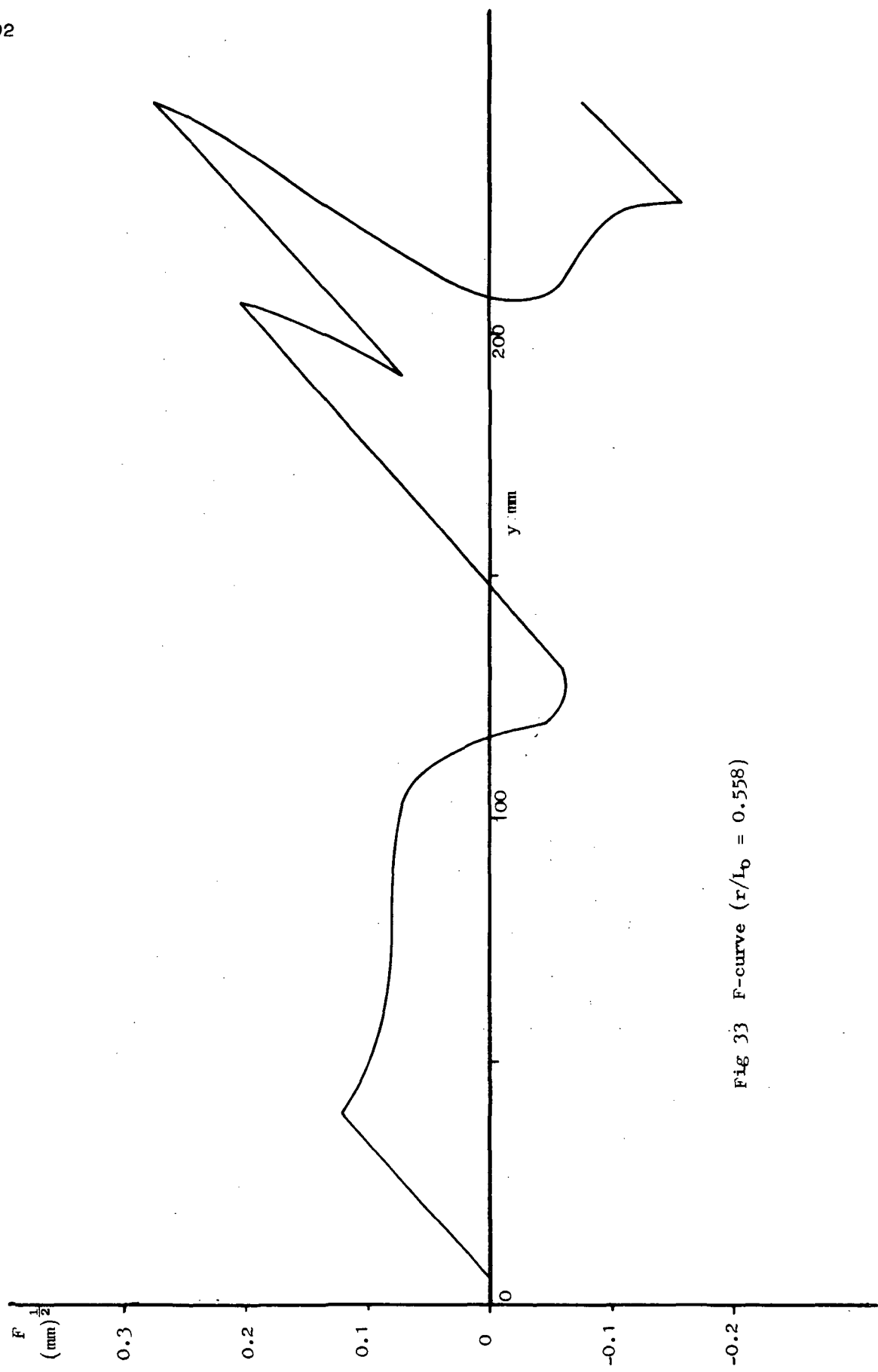


Fig 32 Chosen  $\epsilon$  distribution ( $r/L_o = 0.271$ )



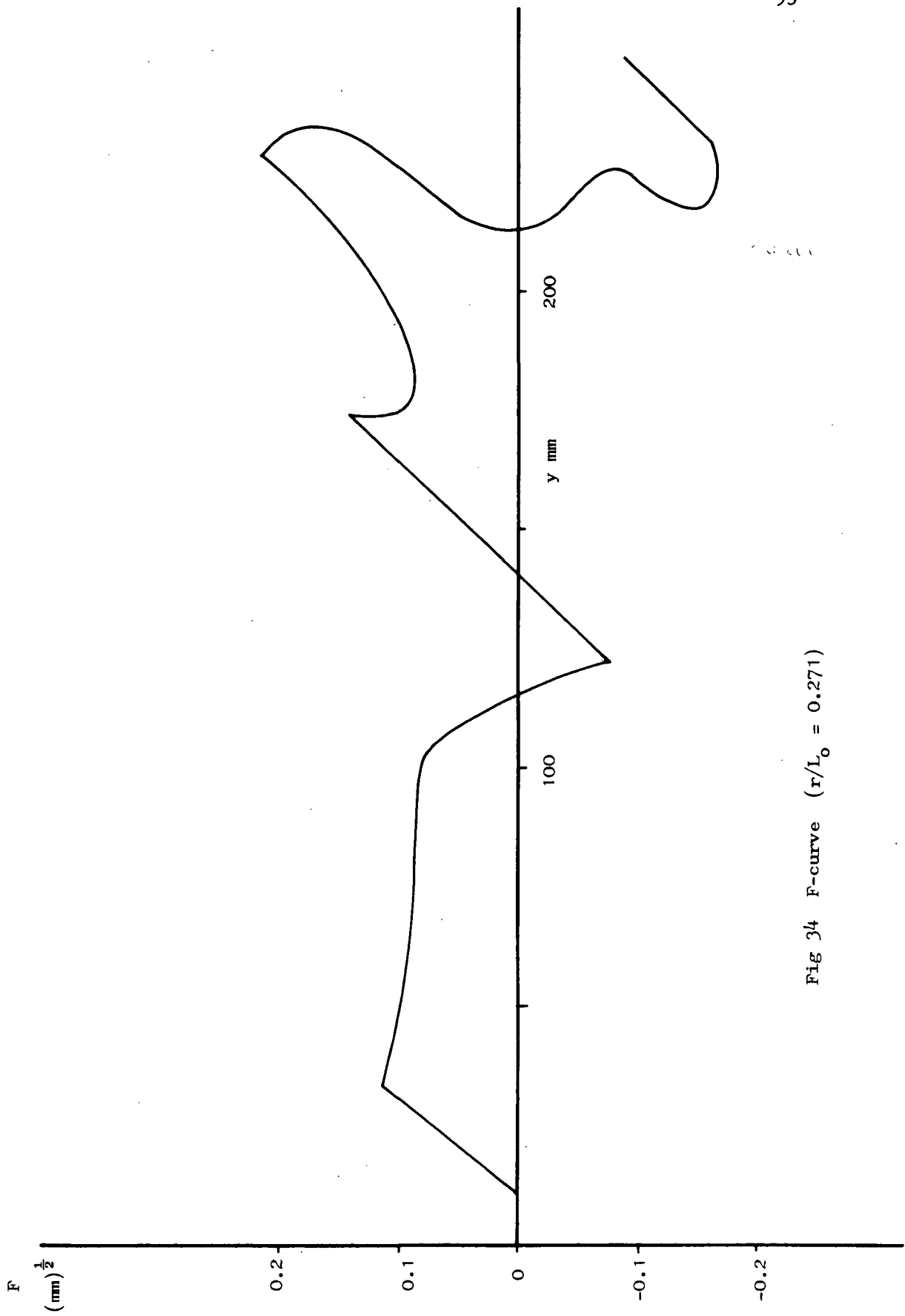


Fig 34 F-curve ( $r/L_o = 0.271$ )

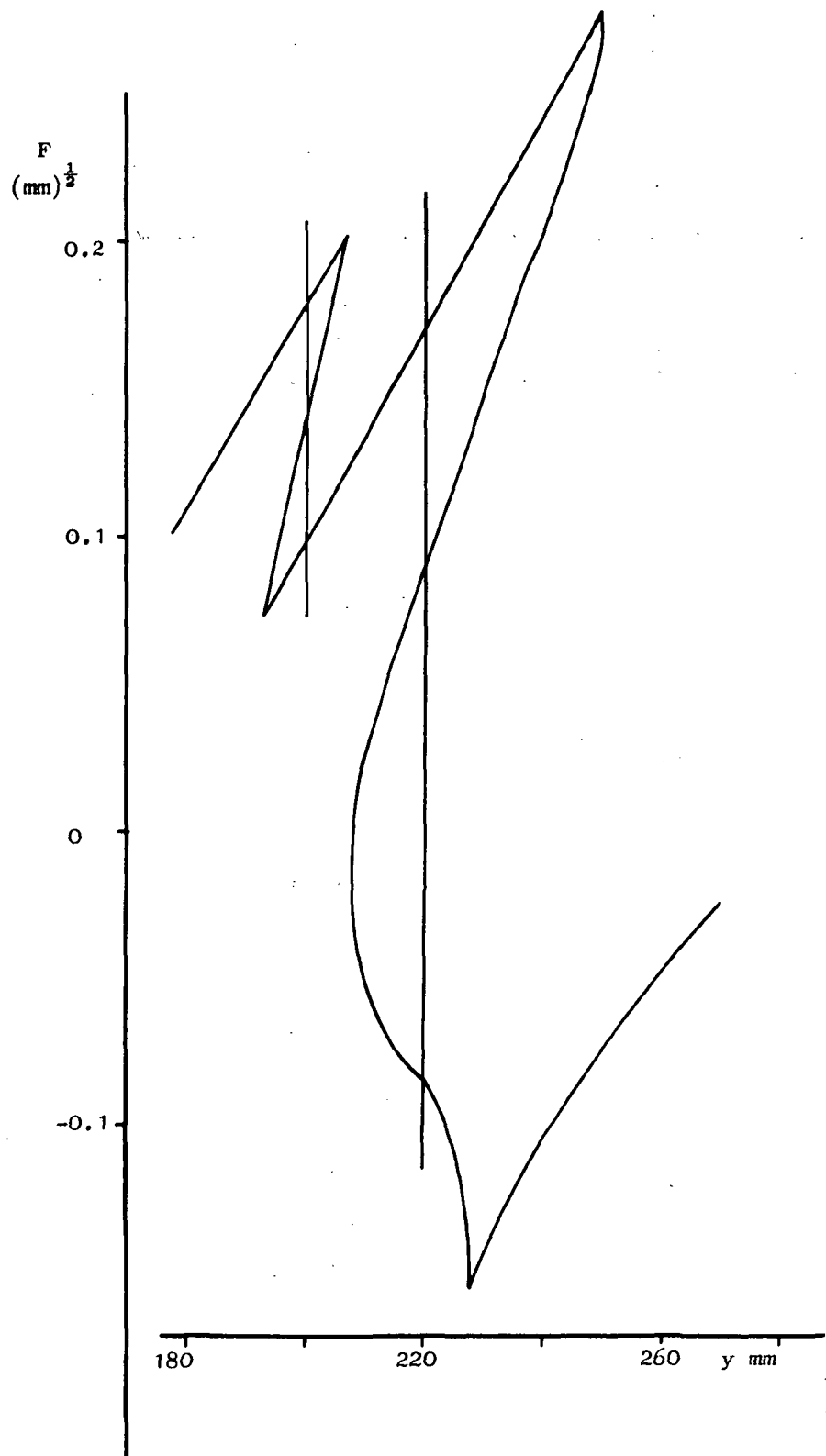


Fig 35 Modifying of F-curve ( $r/L_o = 0.558$ )

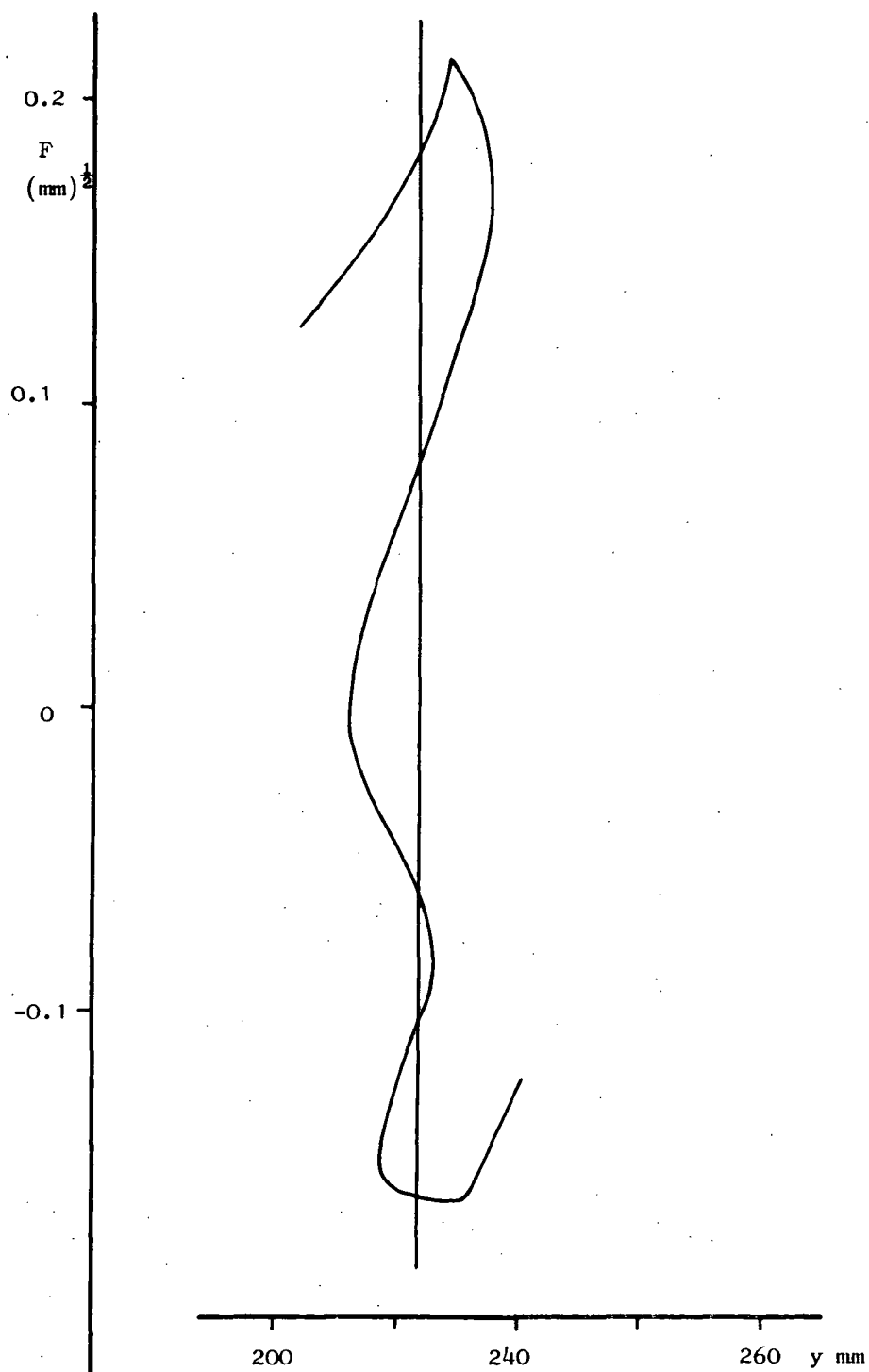


Fig. 36 Modifying of F-curve ( $r/L_o = 0.271$ )

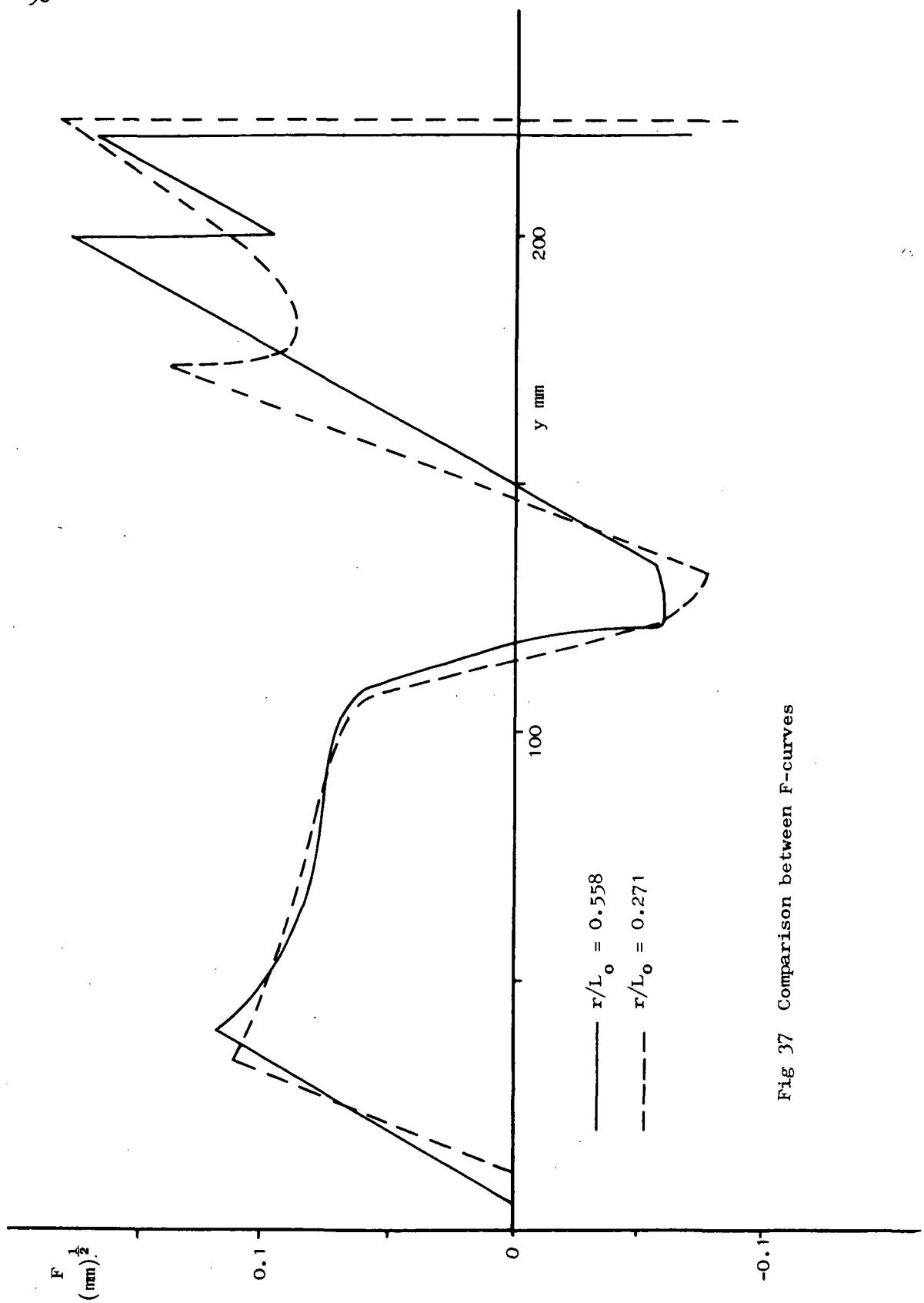


Fig 37 Comparison between F-curves

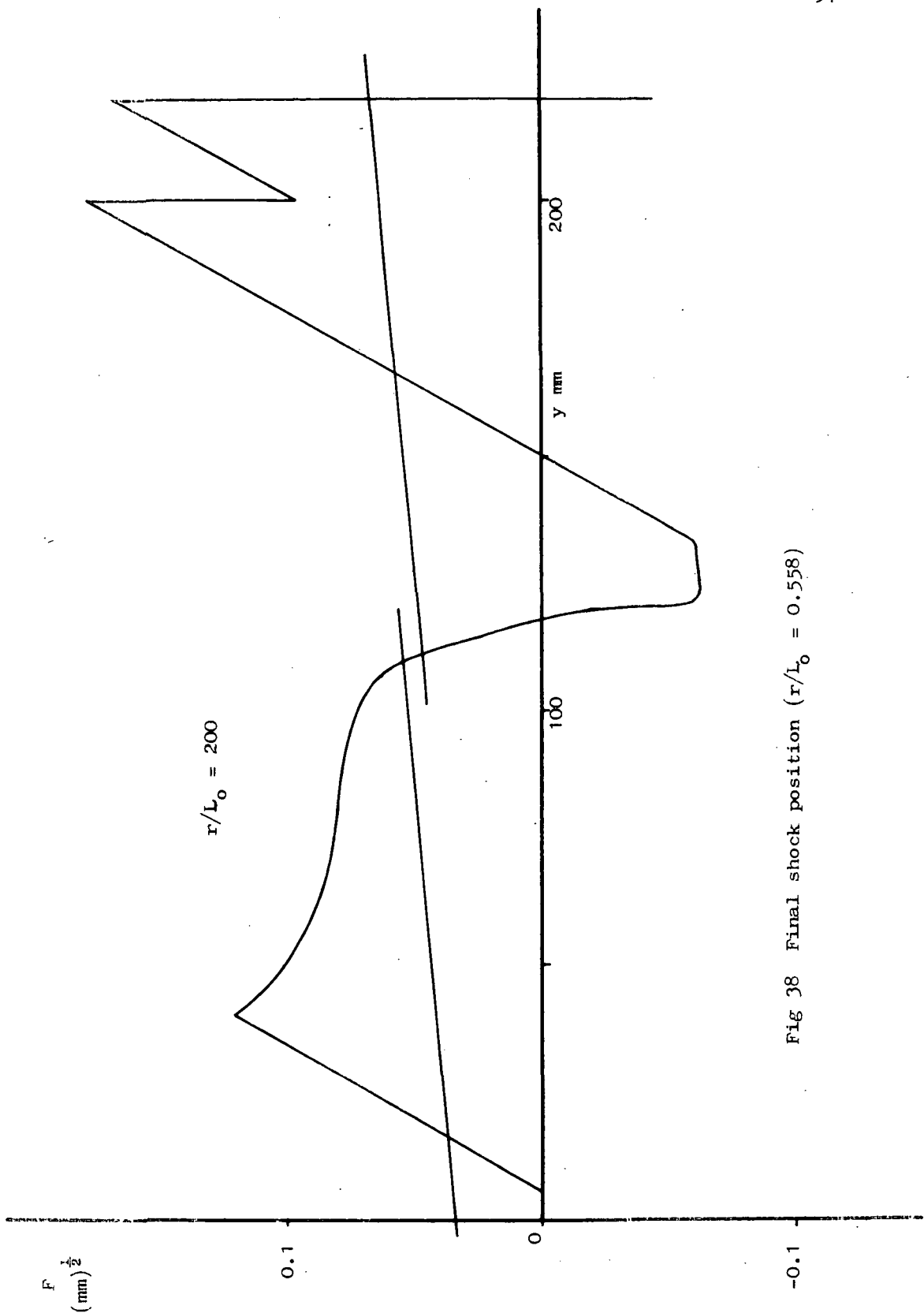
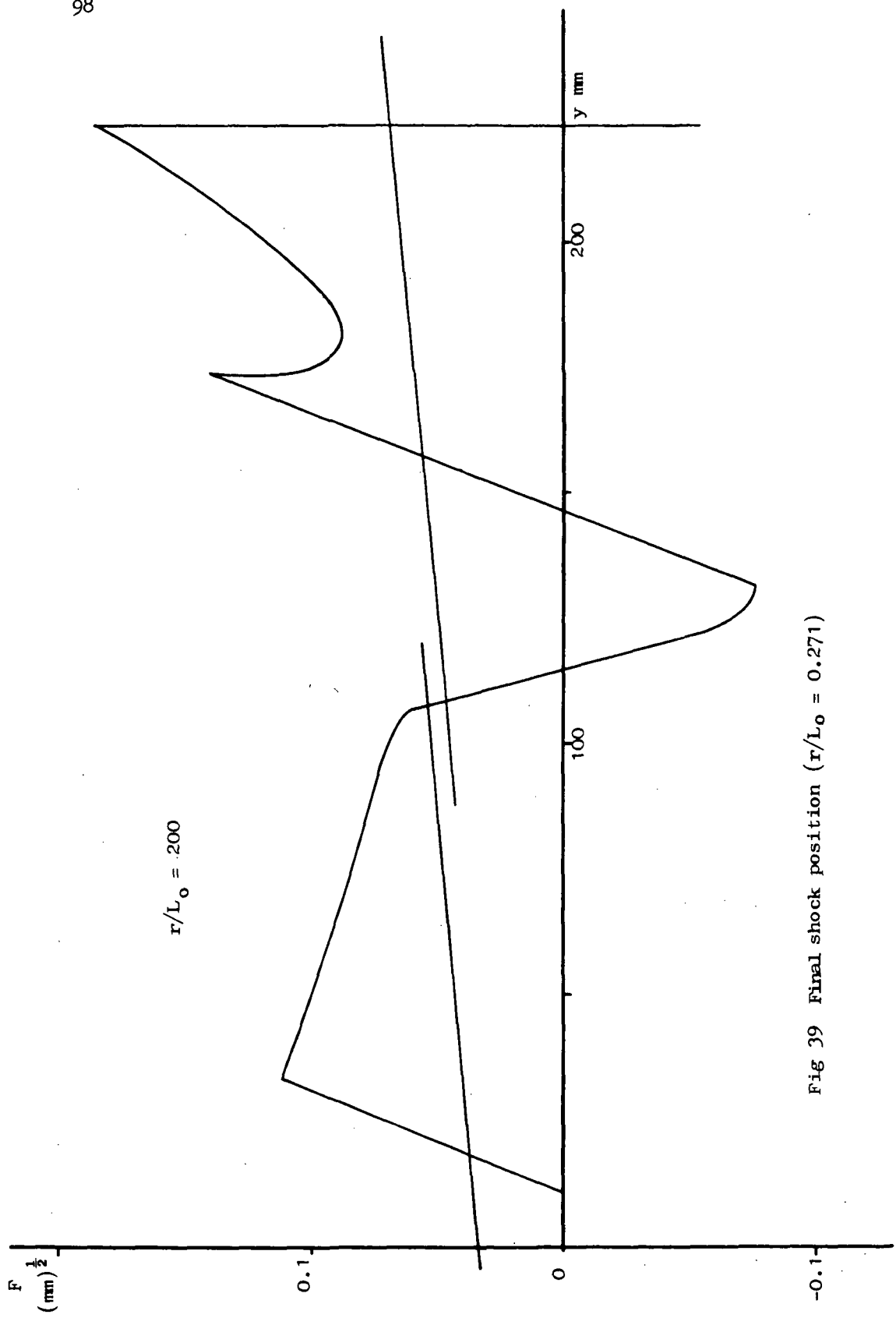


Fig 38 Final shock position ( $r/L_0 = 0.558$ )



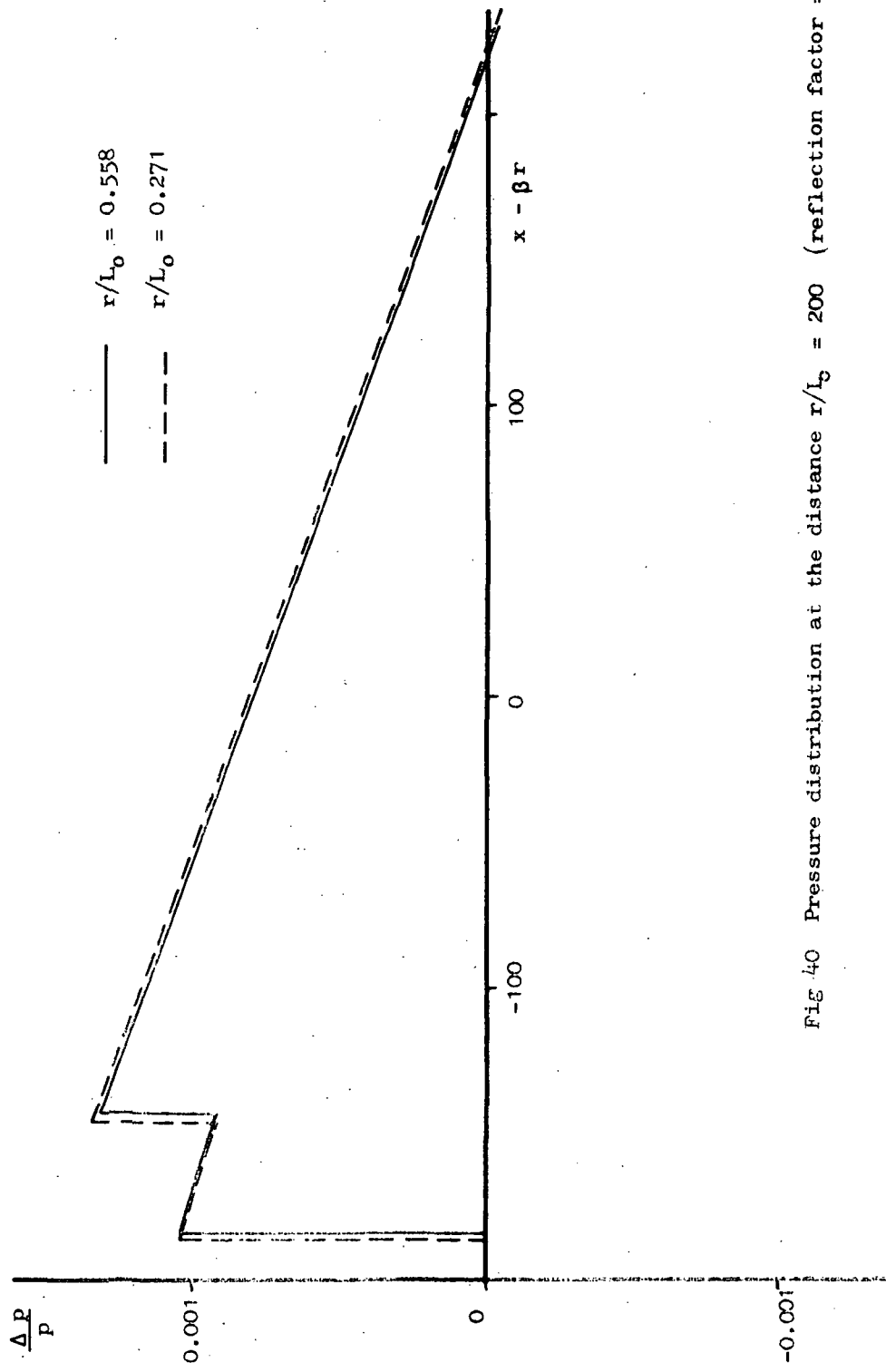


Fig 40 Pressure distribution at the distance  $r/L_0 = 200$  (reflection factor = 1) 99

100

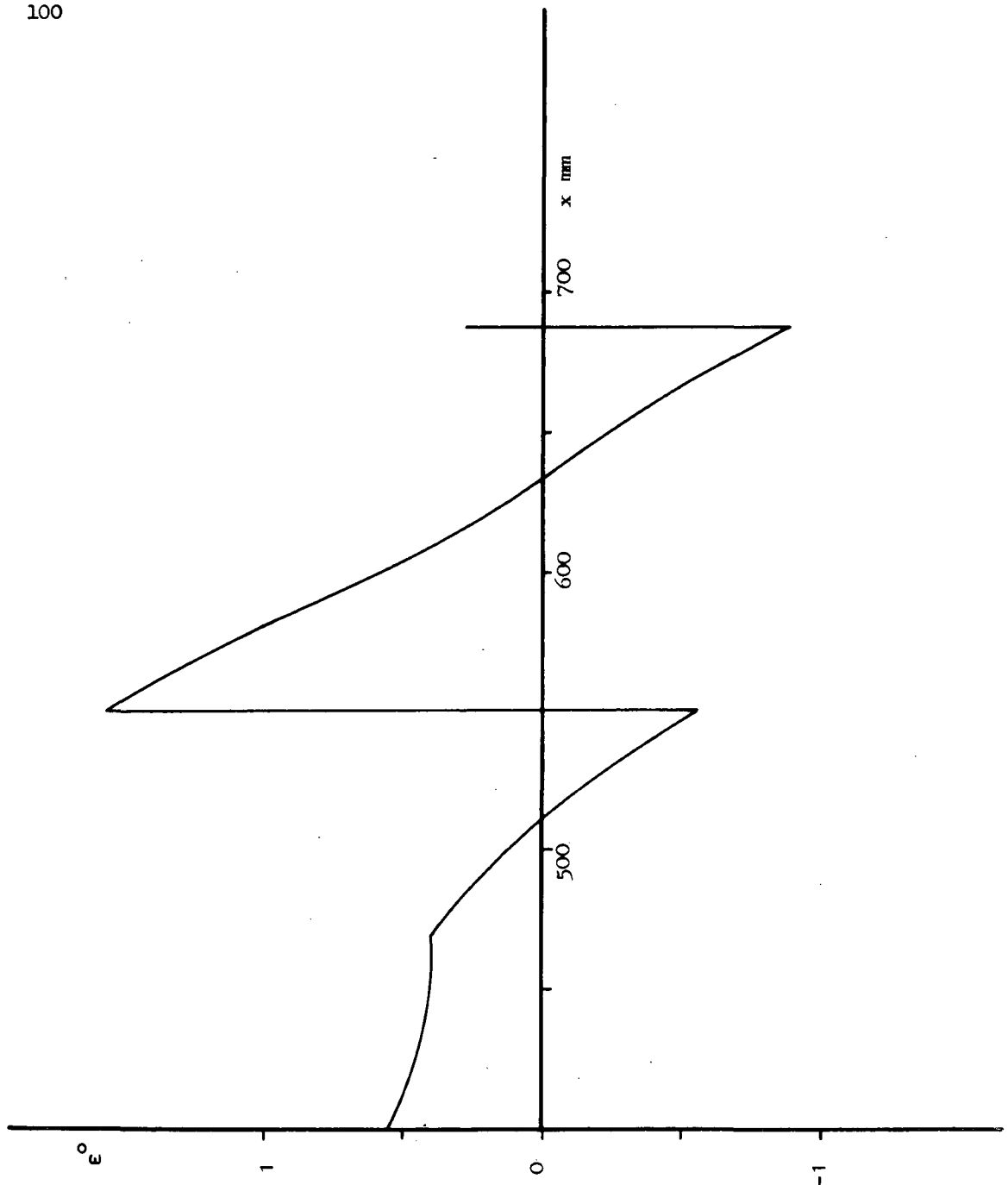


Fig 41 Alternative  $\epsilon$  distribution for  $r/L_o = 0.558$

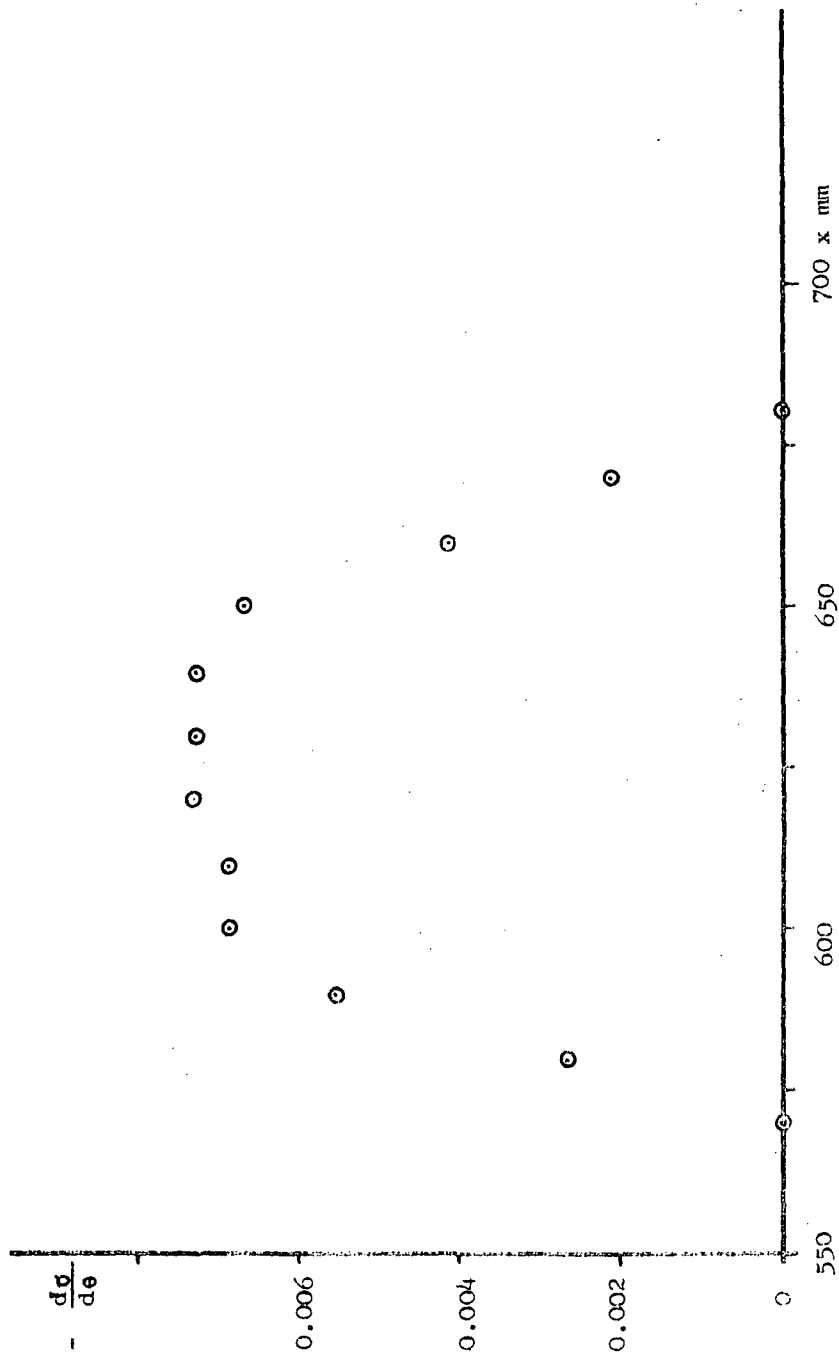


Fig 42 Chosen  $d\sigma/d\theta$ -distribution ( $x/r_0 = 0.558$  : one wing shock)

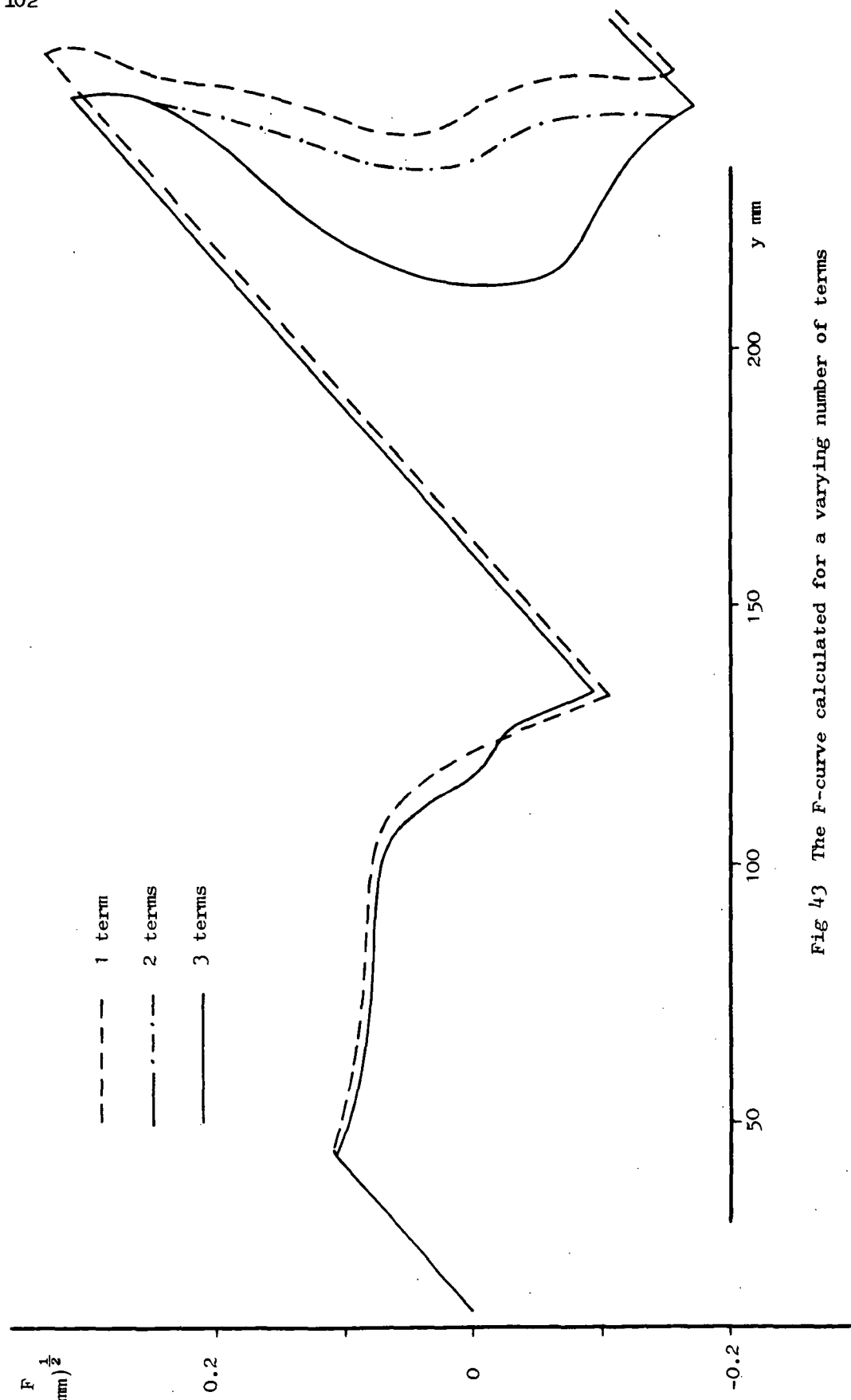


Fig 43 The F-curve calculated for a varying number of terms

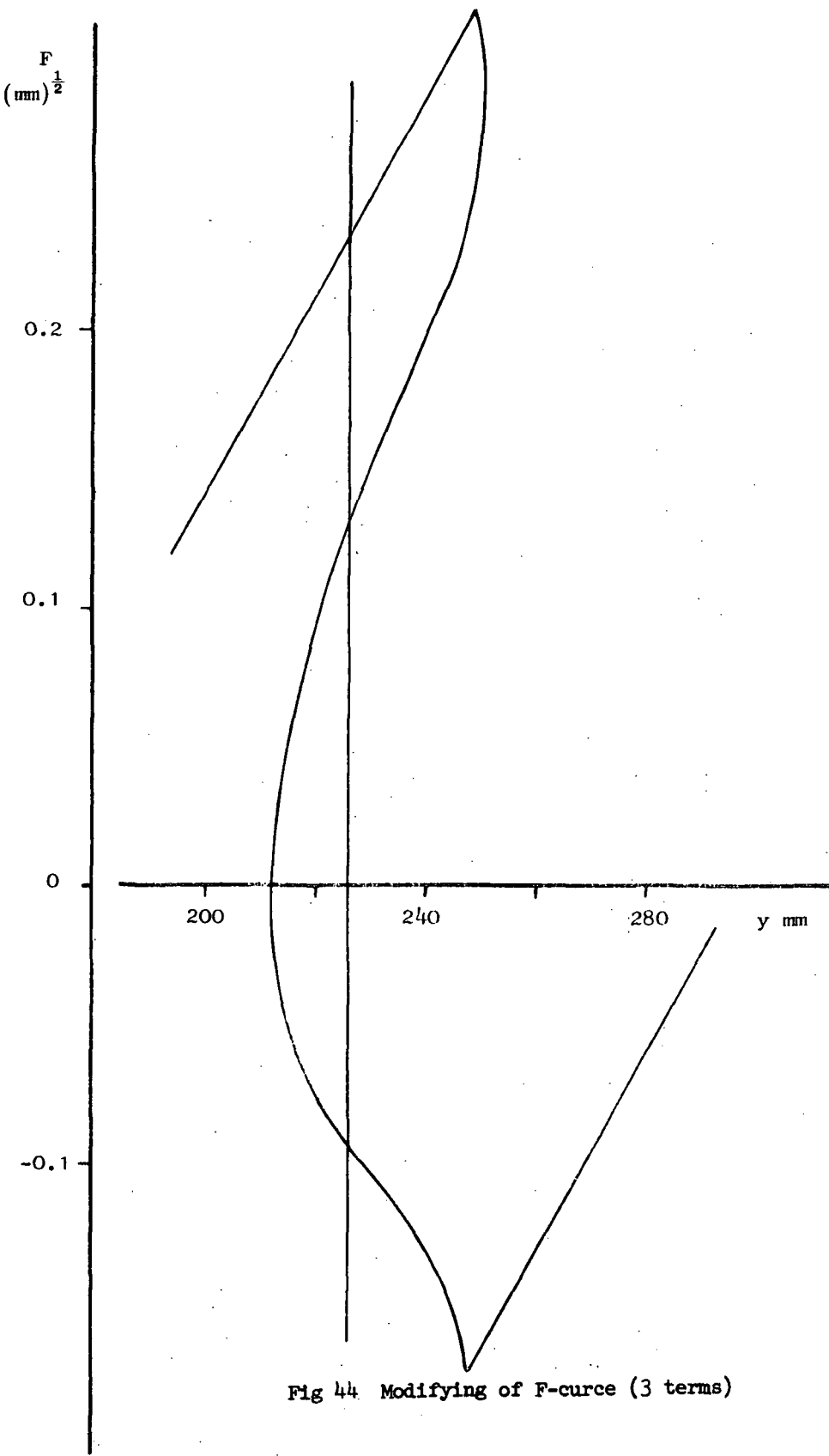


Fig 44. Modifying of F-curve (3 terms)

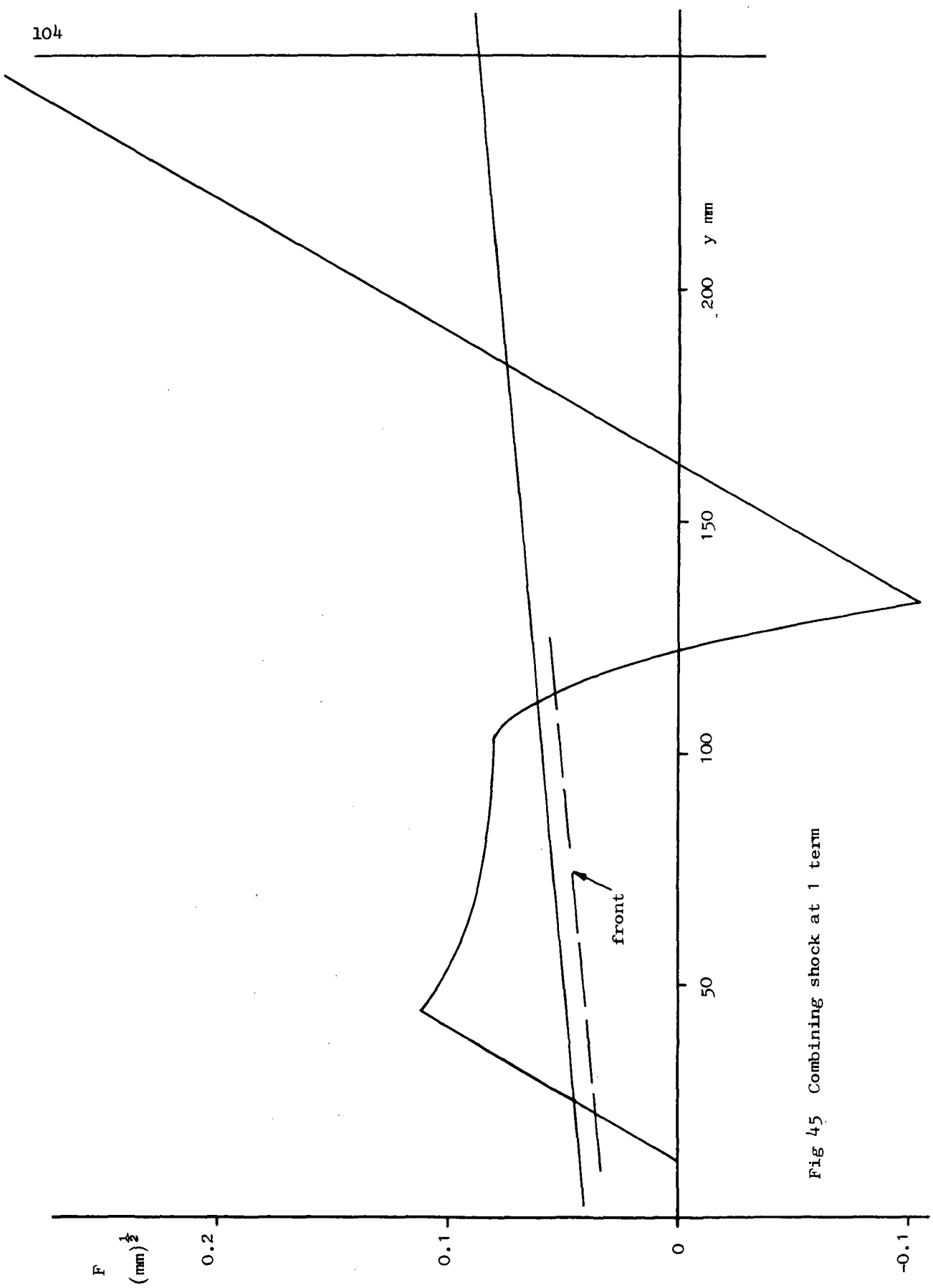


Fig 45 Combining shock at 1 term

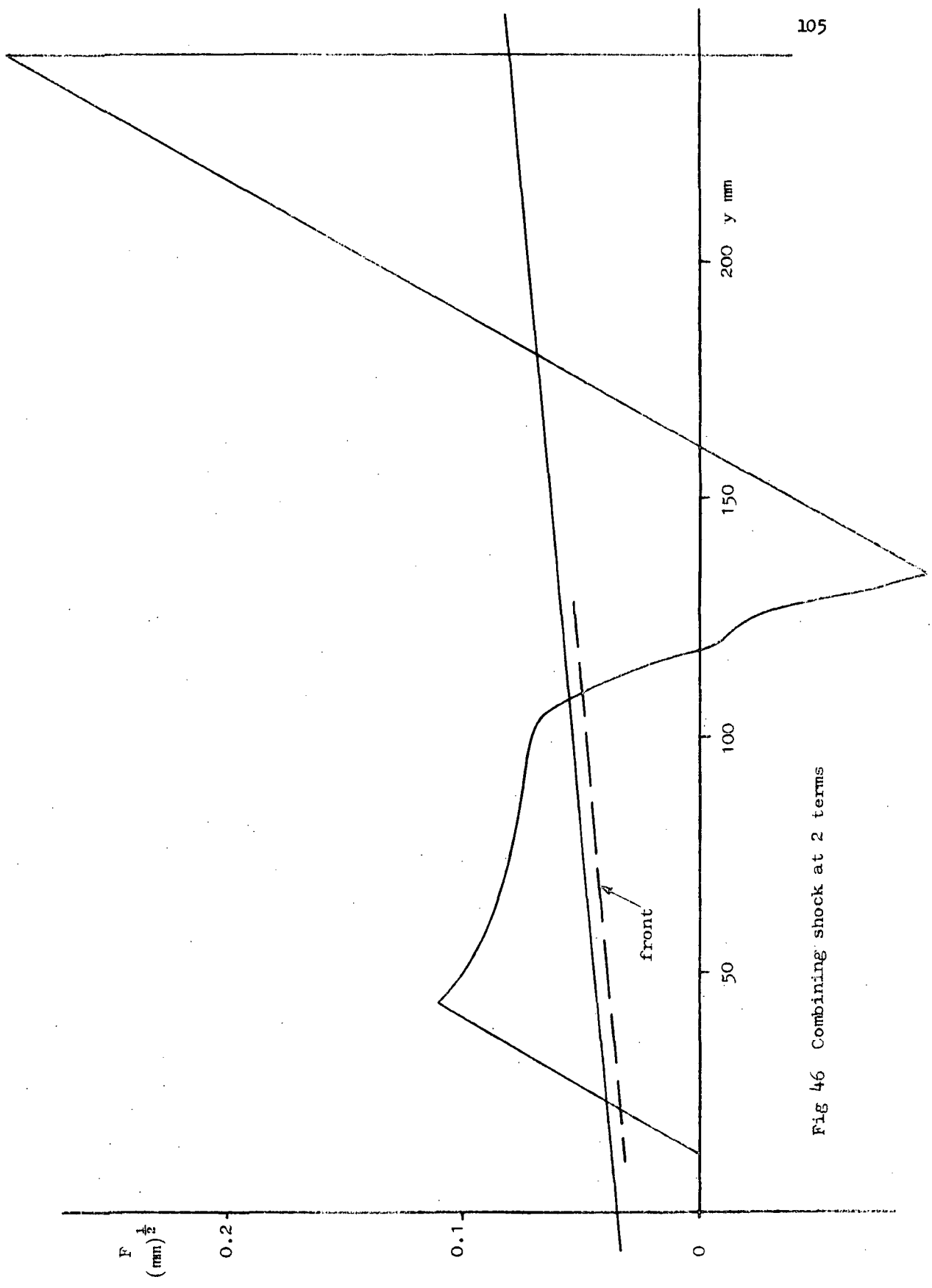


Fig 46 Combining shock at 2 terms

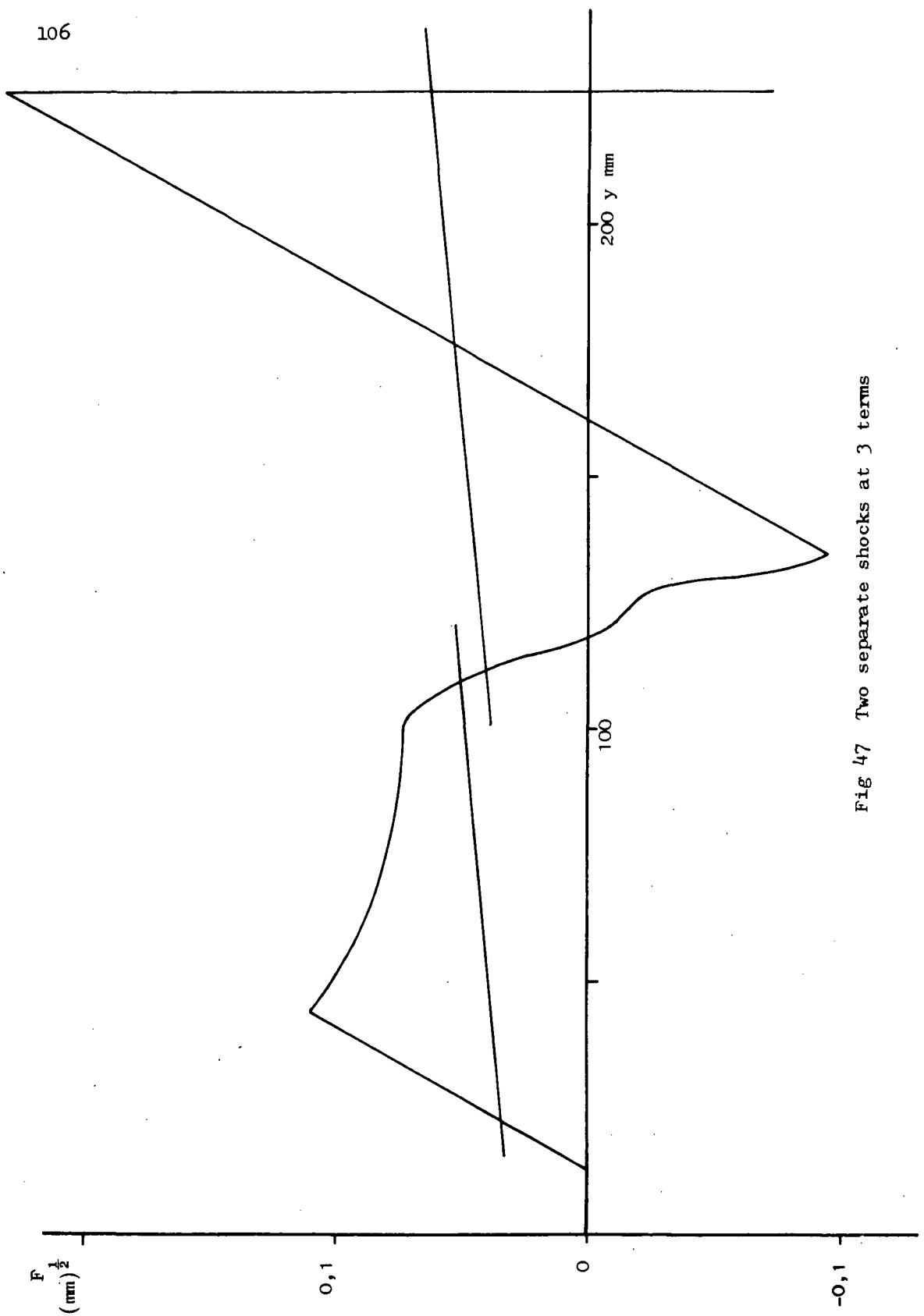


Fig 47 Two separate shocks at 3 terms

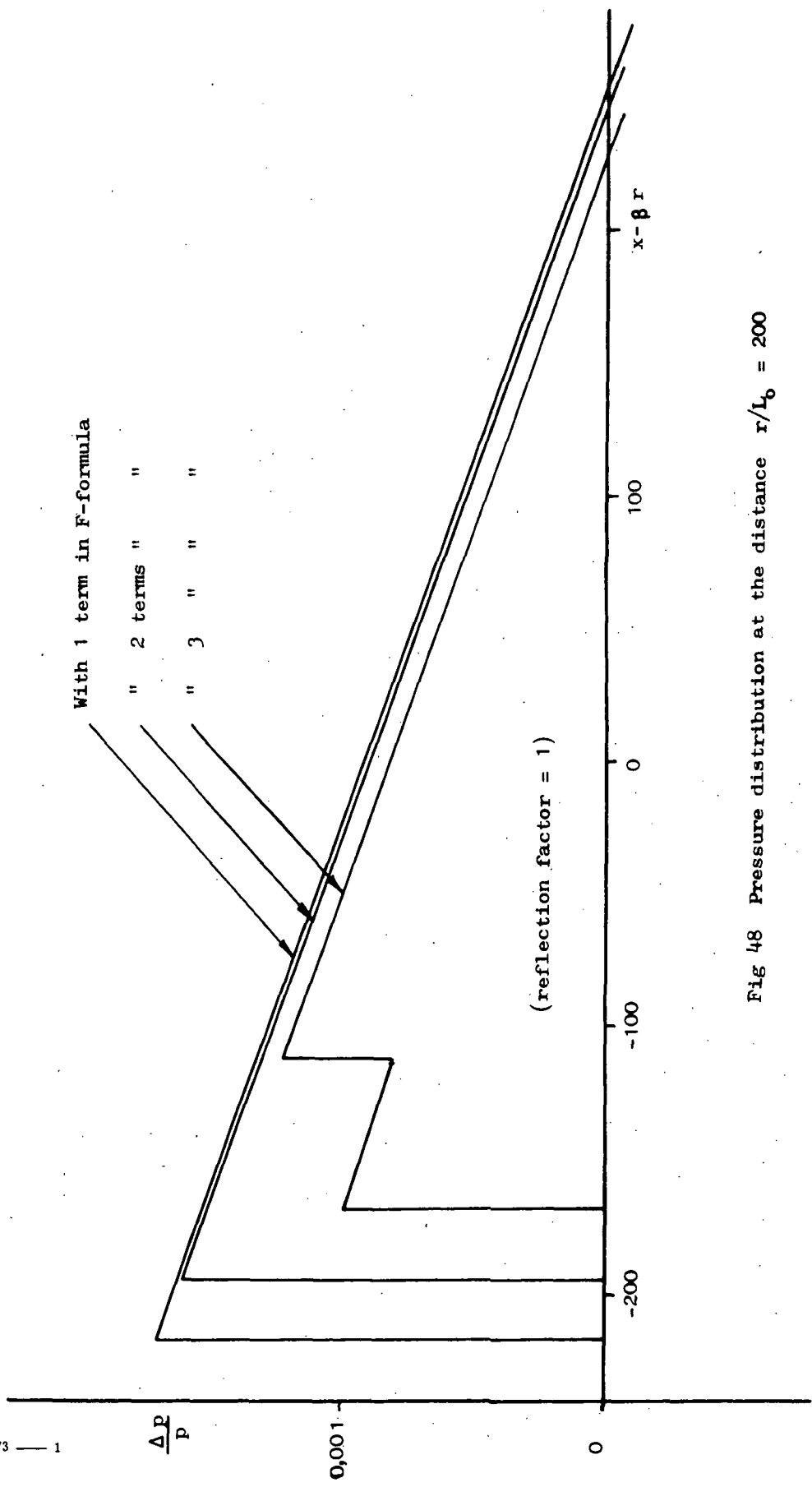


Fig 48 Pressure distribution at the distance  $r/l_0 = 200$

NATIONAL AERONAUTICS AND SPACE ADMINISTRATION  
WASHINGTON, D.C. 20546

OFFICIAL BUSINESS  
PENALTY FOR PRIVATE USE \$300

SPECIAL FOURTH-CLASS RATE  
BOOK

POSTAGE AND FEES PAID  
NATIONAL AERONAUTICS AND  
SPACE ADMINISTRATION  
451



POSTMASTER : If Undeliverable (Section 158  
Postal Manual) Do Not Return

*"The aeronautical and space activities of the United States shall be conducted so as to contribute . . . to the expansion of human knowledge of phenomena in the atmosphere and space. The Administration shall provide for the widest practicable and appropriate dissemination of information concerning its activities and the results thereof."*

—NATIONAL AERONAUTICS AND SPACE ACT OF 1958

## NASA SCIENTIFIC AND TECHNICAL PUBLICATIONS

**TECHNICAL REPORTS:** Scientific and technical information considered important, complete, and a lasting contribution to existing knowledge.

**TECHNICAL NOTES:** Information less broad in scope but nevertheless of importance as a contribution to existing knowledge.

**TECHNICAL MEMORANDUMS:** Information receiving limited distribution because of preliminary data, security classification, or other reasons. Also includes conference proceedings with either limited or unlimited distribution.

**CONTRACTOR REPORTS:** Scientific and technical information generated under a NASA contract or grant and considered an important contribution to existing knowledge.

**TECHNICAL TRANSLATIONS:** Information published in a foreign language considered to merit NASA distribution in English.

**SPECIAL PUBLICATIONS:** Information derived from or of value to NASA activities. Publications include final reports of major projects, monographs, data compilations, handbooks, sourcebooks, and special bibliographies.

**TECHNOLOGY UTILIZATION PUBLICATIONS:** Information on technology used by NASA that may be of particular interest in commercial and other non-aerospace applications. Publications include Tech Briefs, Technology Utilization Reports and Technology Surveys.

*Details on the availability of these publications may be obtained from:*

### SCIENTIFIC AND TECHNICAL INFORMATION OFFICE

NATIONAL AERONAUTICS AND SPACE ADMINISTRATION

Washington, D.C. 20546